



TECHNISCHE  
UNIVERSITÄT  
MÜNCHEN



WALTHER-MEISSNER-  
INSTITUT FÜR  
TIEFTEMPERATUR-  
FORSCHUNG



BAYERISCHE  
AKADEMIE DER  
WISSENSCHAFTEN

---

# Coherent Magnetoelastic Coupling in Magnetic Thin Film/Crystalline Substrate Heterostructures

---

Master's thesis  
Johannes Weber

Advisor: Prof. Dr. Rudolf Gross  
Supervisor: Dr. Matthias Althammer, Manuel Müller  
Garching – November 8, 2023



## Contents

<b>1</b>	<b>Introduction</b>	<b>1</b>
<b>2</b>	<b>Theoretical concepts</b>	<b>5</b>
2.1	Macrospin model . . . . .	5
2.2	Ferromagnetic resonance . . . . .	7
2.3	Magnon-phonon coupling . . . . .	9
2.4	Quarpartite coupling . . . . .	14
<b>3</b>	<b>Experimental procedure</b>	<b>17</b>
3.1	Sample fabrication . . . . .	17
3.2	Experimental technique . . . . .	18
3.3	Experimental setup . . . . .	20
<b>4</b>	<b>Temperature dependence of magnetoelastic coupling in YIG/GGG heterostructures</b>	<b>23</b>
4.1	Data analysis for YIG/GGG magnetoelastic coupling . . . . .	23
4.2	Differences of magnetoelastic coupling in the ip/oop geometry . . . . .	25
4.3	Study of the temperature dependent tuning of the phononic resonances . . . . .	32
4.4	Frequency dependence of the magnetoelastic coupling . . . . .	34
<b>5</b>	<b>Dependence of the magnetoelastic coupling on the orientation of the substrate in CoFe/Sapphire heterostructures</b>	<b>37</b>
5.1	Crystalline direction dependence of the transverse acoustic sound velocity . . . . .	37
5.2	Frequency dependence of the magnetoelastic linewidth . . . . .	41
5.3	Temperature dependence of the magnetic and acoustic parameters . . . . .	43
<b>6</b>	<b>Magnetoelastic coupling in CoFe/Si heterostructures</b>	<b>47</b>
6.1	Data analysis for CoFe/Si magnetoelastic coupling . . . . .	47
6.2	Layer thickness optimization of $\text{Co}_{25}\text{Fe}_{75}$ for Magnon-Phonon coupling . . . . .	49
6.3	Dependence of the magnetoelastic coupling on the substrate thickness . . . . .	50
6.4	Tripartite Magnon-phonon coupling in a CoFe/Si/CoFe trilayer sample . . . . .	57
<b>7</b>	<b>Summary</b>	<b>59</b>
7.1	Temperature dependence of magnetoelastic coupling in YIG/GGG heterostructures . . . . .	59
7.2	Dependence of the magnetoelastic coupling on the orientation of the substrate in CoFe/Sapphire heterostructures . . . . .	60
7.3	Magnetoelastic coupling in CoFe/Si heterostructures . . . . .	61
<b>8</b>	<b>Outlook</b>	<b>63</b>
<b>9</b>	<b>Acknowledgements</b>	<b>75</b>



# 1 Introduction

"Make everything as simple as possible, but not simpler."

(Albert Einstein)

This famous quote of Albert Einstein, winner of the nobel prize in physics in 1922 for his description of the photoelectric effect [1] holds true to all fields of physics, where scientists aim to describe phenomena in nature with mathematical models. The quote describes the challenge to break down the laws of nature to as simple as possible mathematical models, that can be solved with low computational effort, while still giving a good description of real phenomena. A model 'too' simple fails to describe an experiment accurately, while a 'too' complex model can either not or only be solved with excessive computational effort and therefore also cannot give a prediction. A famous example for a 'too' simple model are Newton's laws of motion [2], which can predict the orbits of the planets in our solar system reasonably good for all planets except for mercury's, whose orbit could be first accurately described with Einstein's more complex 'General Theory of Relativity' [3]. Furthermore, Einstein firstly described the relation between the specific heat of crystals and lattice vibrations, which are also called phonons [4].

Phonons, the excitation of vibrational modes in a crystalline lattice [5], can interact with both a variety of different physical particles like electrons, which is used to explain the formation of Cooper-pairs in superconductors [6, 7], or physical fields like the electromagnetic field, which yields the quasi-particle called phonon polariton [8].

In this master's thesis, we investigate the coupling between magnons, the quantized excitation of spins in a crystal lattice [9], and phonons using bulk acoustic wave (BAW) resonators consisting of a ferro-/ferrimagnetic layer deposited on top of a crystalline substrate. BAW resonators have potential applications in radio frequency filters, which are used in fifth generation (5G) telecommunication technology, due to low insertion losses [10] and they can also be monolithically integrated with active circuit elements [11]. BAW resonators also have applications in quantum technologies. For example, they were recently used to demonstrate non-classical behavior on a macroscopic scale, where the quantum state of the phonon was measured via a superconducting qubit coupled to the BAW resonator [12]. They are also used for solid-state quantum acoustodynamic systems, which couple acoustic phonon sources with superconducting or spin qubits and allow for quantum information storage and processing [13–16].

In the first experimental chapter of this thesis, we expand upon the previous work in Ref. [17] by studying the magnetoelastic coupling for the established material system YIG/GGG in a wide temperature range from 3 K to 300 K and for different measurement geometries. Furthermore, we investigate the magnetoelastic coupling between magnetometallic CoFe thin films and sapphire substrates oriented in varying crystalline directions, thus expanding on previous works [18–20] and study the frequency and temperature-dependent behavior of the magnetoelastic parameters. Finally, we continue the previous works in Refs.[18, 19, 21] by characterizing the magnetoelastic coupling in CoFe/Silicon samples with different substrate thicknesses and perform experiments on CoFe/Si/CoFe trilayer samples at cryogenic temperatures.

This thesis is structured as follows: We begin by explaining the theoretical concepts necessary to understand the contents of this thesis in chapter 2. We start with explaining the Macrospin model in Sec. 2.1 and introduce important concepts such as the Heisenberg exchange interaction, to model the interactions of the magnetic moments in a solid. We define the magnetization as the sum of all the individual magnetic moments and model the magnetization dynamics using the Landau-Lifshitz-Gilbert equation, which is a phenomenological equation describing the precession of the magnetization around an effective magnetic field after it has been excited. Furthermore, we introduce the concept of ferromagnetic resonance in Sec. 2.2 and explain two different experimental excitation geometries, where the external magnetic field is applied parallel and orthogonal to the surface normal. Next, in Sec. 2.3, we study magnon-phonon coupling and present a phenomenological description of the energy density. Moreover, we model the sample geometries used in this thesis with sets of equations, that couple two transverse acoustic phonon modes with one Kittel mode for the investigated magnet/substrate heterostructures and one transverse acoustic phonon mode couples with two Kittel modes for the investigated magnet/substrate/magnet heterostructures. From the solution of these equations, we obtain insight into the effective coupling strength, acoustic and magnetic damping rates in these systems. Lastly, in Sec. 2.4, we write down the set of equations for a magnet/substrate/magnet heterostructure, where both the transverse acoustic phonon modes couple with both the Kittel modes.

In chapter 3, we go into detail about the fabrication process of our samples with DC sputtering technique in the SUPERBOWL machine in Sec. 3.1. Furthermore, we explain the experimental technique for the ferromagnetic resonance measurements done in this thesis and how to extract relevant data from fitting the imaginary and real part of the transmission parameter to the Polder susceptibility in Sec. 3.2. To conclude our experimental methods chapter, we discuss in Sec. 3.3 the experimental setup for ferromagnetic resonance measurements and the MORIA cryostat used for conducting our experiments.

In chapter 4, we characterize a YIG/GGG sample and study the effective magnetoelastic coupling rate as a function of temperature as well as microwave frequency and compare the results for the in-plane and out-of-plane measurement geometries. In addition, we study the temperature dependent behavior of the phononic resonances.

In chapter 5, we focus on CoFe/Sapphire heterostructures and explore the possibility of controlling phononic birefringence with crystalline substrates grown in various directions. We also study the frequency and temperature dependent behavior of magnetoelastic parameters in the heterostructures.

In chapter 6, we investigate CoFe/Silicon samples with different substrate thicknesses and also study the frequency dependence of the magnetoelastic parameters and how the substrate thickness affects them. Additionally, we study the magnetoelastic coupling in CoFe/Si/CoFe trilayer structures and study the magnetoelastic linewidth as a function of the frequency at cryogenic temperatures.

Chapter 7 provides a summary of the in this thesis achieved results.

Finally, in chapter 8, we suggest further research ideas and questions, which could not be addressed in this thesis. As an example we show our first broadband ferromagnetic resonance measurements of CoFe-gratings deposited on silicon single crystal substrates as a

first attempt to induce surface acoustic waves in this material system as compared to the established LiNbO<sub>3</sub> on silicon material system investigated in Refs. [22, 23].



## 2 Theoretical concepts

In this chapter, we describe the theoretical concepts required to interpret the experimental results in this thesis. In Sec. 2.1 we start with explaining the Heisenberg exchange interaction, which describes the coupling of spins through the overlap of their wavefunctions. As a next step, we introduce the definitions of the magnetic moment and the magnetization of a ferromagnetic volume, which we use to explain the magnetization dynamics in an effective field via the so-called Landau-Lifshitz-Gilbert equation. Furthermore, we explain ferromagnetic resonance and derive expressions for the magnetic resonance frequency as a function of the external magnetic field for different geometries, the so called Kittel equations [24] in Sec. 2.2. As a final step, we describe magnon-phonon coupling of the magnetic Kittel mode coupled to phonons in crystalline substrate materials serving as bulk acoustic wave resonators in Sec. 2.3 and derive an expression for the effective magnetoelastic coupling strength in the system as function of microwave frequency.

### 2.1 Macrospin model

#### 2.1.1 Heisenberg exchange interaction

Magnetism is described by quantum mechanics. The Bohr-van Leeuwen theorem states that the net magnetic order in a thermal equilibrium vanishes, when applying classical statistics [25, 26], as the kinetic energy of charge carriers does not change, when exposed to an external magnetic field. Hence, a classical electron system in thermal equilibrium has no magnetic moment. It follows that magnetism has to be a quantum phenomenon manifesting on a macroscopic scale [5]. As a consequence of the individual electron spins  $s_i$  and their interaction with each other - the so-called spin-spin interaction- magnetism can arise in a solid. The magnetic moment of an atom itself is proportional to its total spin momentum  $\mathbf{J} = \mathbf{L} + \mathbf{S}$  composed of the atomic angular momentum  $\mathbf{L}$  and the net spin momentum  $\mathbf{S}$ , which themselves are the total electron angular and spin momenta of the atomic valence shell electrons. To describe the interaction between the individual atomic magnetic moments, it is not sufficient to model the coupling between the magnetic moments of localized electrons of a solid via dipole-dipole interaction, because the energy scales of this interaction are an order of magnitude smaller than the thermal energy at room temperature [5]. Instead, the magnetic coupling is mediated through overlapping of the wavefunctions of the localized electrons, which can be modeled by the Heisenberg exchange mechanism [5, 18, 27, 28]. The free energy density of a solid with Volume  $V$ , summing up over all nearest-neighbor pairs (n.n), is defined as

$$F_{\text{ex}} = -\frac{1}{\hbar^2 V} \sum_{i < j, \text{n.n}} E_{ij} \mathbf{J}_i \cdot \mathbf{J}_j, \quad (2.1)$$

where  $E_{ij}$  is the exchange constant. The Heisenberg model is capable of modelling a ferromagnetic solid with parallel alignment of spins and a antiferromagnetic solid with antiparallel alignment of spins depending on the sign of  $E_{ij}$ . That means for  $E_{ij} > 0$  the ferromagnetic configuration and for  $E_{ij} < 0$  the antiferromagnetic configuration is preferred. This model is also applicable to magnetic metals with free electrons by utilizing mean-field

theory [5].

### 2.1.2 Magnetization

A single atom in a solid has a magnetic moment  $\mu$  proportional to its total spin momentum  $\mathbf{J}$

$$\boldsymbol{\mu} = -\gamma\mathbf{J}, \quad (2.2)$$

where  $\gamma = \frac{g\mu_B}{\hbar}$  is the gyromagnetic ratio with  $g$  the Landé  $g$ -factor [29],  $\mu_B$  the Bohr magneton [30] and  $\hbar$  is the reduced Planck constant [31].

We now define the net sample magnetization of a magnetic volume as the sum over all the individual magnetic moments normalized by the sample volume  $V$

$$\mathbf{M} = \frac{1}{V} \sum_{\boldsymbol{\mu}_i \in V} \boldsymbol{\mu}_i. \quad (2.3)$$

When all magnetic moments are aligned parallel to each other, the magnetization is at its maximum, which is given by the saturation magnetization  $|\mathbf{M}| = M_s$ . In the following we assume  $\mathbf{M} = M_s \mathbf{m}$ , with the unit vector  $\mathbf{m} = (m_x, m_y, m_z)$ .

### 2.1.3 Landau-Lifshitz-Gilbert equation

As a next step, we discuss the magnetization dynamics when exposed to an effective magnetic field  $\mathbf{H}_{\text{eff}}$  of the form

$$\mathbf{H}_{\text{eff}} = \mathbf{H}_{\text{ext}} + \mathbf{H}_{\text{ani}} + \mathbf{H}_{\text{d}}, \quad (2.4)$$

where  $\mathbf{H}_{\text{ext}}$  is the externally applied magnetic field,  $\mathbf{H}_{\text{ani}}$  is the anisotropy field and  $\mathbf{H}_{\text{d}}$  is the demagnetization field. The anisotropy field  $\mathbf{H}_{\text{ani}}$  can consist e.g of contributions that point along certain crystallographic directions due to the crystal symmetry or due to a pinning of the magnetization when a magnetic material is interfaced with an antiferromagnet. The demagnetization term comes from a magnetic anisotropy term called shape anisotropy, that is generated by the magnetization itself to reduce stray fields [5].

The magnetization  $\mathbf{M}$  experiences a torque from the effective field  $\mathbf{H}_{\text{eff}}$  of the form

$$\boldsymbol{\tau} = \frac{d\mathbf{J}}{dt} = -\boldsymbol{\mu} \times \mu_0 \mathbf{H}_{\text{eff}}. \quad (2.5)$$

Now using equation (2.2) and (2.3) and plugging them into Eq. (2.5), we obtain

$$\frac{d\mathbf{M}}{dt} = -\gamma \mathbf{M} \times \mu_0 \mathbf{H}_{\text{eff}}. \quad (2.6)$$

This expression is known as the Landau-Lifshitz equation [32], which states, that in the presence of an effective magnetic field  $\mathbf{H}_{\text{eff}}$ , when excited the magnetization  $\mathbf{M}$  precesses at a fixed angle around  $\mathbf{H}_{\text{eff}}$ . However, in real physical systems there are many relaxation mechanisms for  $\mathbf{M}$ , which are taken into account by a phenomenological damping parameter called the Gilbert damping parameter  $\alpha$ . This parameter was introduced by Gilbert

[33] thus leading to the Landau-Lifshitz-Gilbert equation

$$\frac{d\mathbf{M}}{dt} = -\gamma\mathbf{M} \times \mu_0\mathbf{H}_{\text{eff}} + \frac{\alpha}{M_s}\mathbf{M} \times \frac{d\mathbf{M}}{dt}, \quad (2.7)$$

where again the first term describes the precession of the magnetization  $\mathbf{M}$  around the effective field  $\mathbf{H}_{\text{eff}}$  and the second term is a phenomenological parameter describing the damping of the system. This damping term points perpendicular to both the magnetization  $\mathbf{M}$  and the precession term  $\mathbf{M} \times \mu_0\mathbf{H}_{\text{eff}}$  towards the center of rotation. Hence, this damping term leads to a spiraling motion of the magnetization  $\mathbf{M}$  around  $\mathbf{H}_{\text{eff}}$  until it relaxes in parallel to  $\mathbf{H}_{\text{eff}}$ .

## 2.2 Ferromagnetic resonance

In the previous section, we have established the magnetization dynamics of a magnetization  $\mathbf{M}$  in an effective field  $\mathbf{H}_{\text{eff}}$ . As a next step, we now extend this model by introducing an oscillating magnetic field  $\mathbf{h}_{\text{rf}}(t)$  perpendicular to the effective field  $\mathbf{H}_{\text{eff}}$ , which counteracts the Gilbert damping term as depicted in Fig. 2.1 panel a). This situation can be described by a driven, damped harmonic oscillator [34]. The following derivations are taken from Refs. [18, 34, 35].

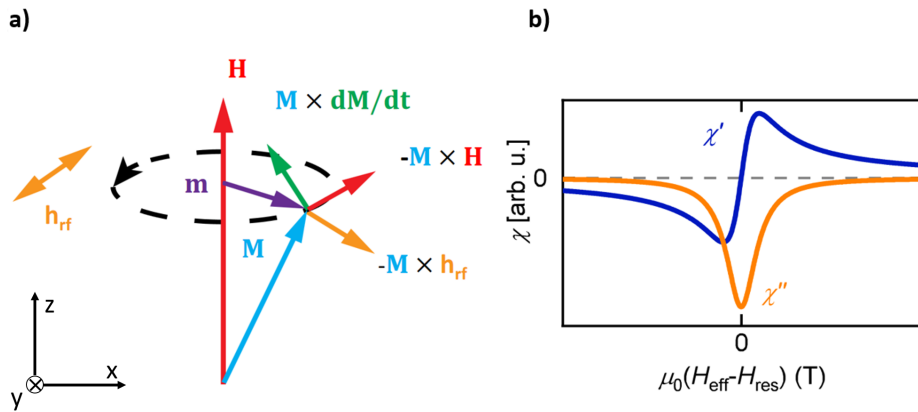


**Figure 2.1:** Ferromagnetic resonance. a) Schematic depiction of ferromagnetic resonance, where the additional driving torque ( $-\mathbf{M} \times \mathbf{h}_{\text{rf}}$ ), generated by the oscillating field  $\mathbf{h}_{\text{rf}}$ , opposes the damping term ( $\mathbf{M} \times \frac{d\mathbf{M}}{dt}$ ) leading to a precession of the magnetization  $\mathbf{M}$  around  $\mathbf{H}_{\text{eff}}$  at a fixed cone angle. b) Real and imaginary part of the Polder susceptibility  $\chi = \chi' + i\chi''$  plotted as function of effective field  $H_{\text{eff}}$ . Taken from Ref. [18].

We start modeling this problem by assuming, that the constant external magnetic field is parallel to the z-axis ( $\mathbf{H}_{\text{ext}} = H_{\text{ext}}\hat{\mathbf{e}}_z$ ) and the magnetization  $\mathbf{M}$  is dynamically driven by an oscillatory field  $\mathbf{h}_{\text{rf}}(t)$  in the x-y-plane, as shown in Fig. 2.1a). This leads to a dynamic response of the magnetization  $\mathbf{m}(t)$  and we can modify the effective field  $\mathbf{H}_{\text{eff}}$  and the magnetization  $\mathbf{M}$  by assuming, that the cone angle  $\varphi$  is small with  $M_x, M_y \ll M_z$  and  $|\mathbf{h}_{\text{rf}}| \ll |\mathbf{H}_{\text{ext}}|$ . Effective field  $\mathbf{H}_{\text{eff}}$  and magnetization  $\mathbf{M}$  can then be written as

$$\begin{aligned} \mathbf{H}_{\text{eff}} &= \mathbf{H}_{\text{ext}} + \mathbf{H}_{\text{ani}} + \mathbf{H}_{\text{d}} + \mathbf{h}_{\text{rf}}(t) \\ \mathbf{M} &= \mathbf{M}_0 + \mathbf{m}(t) = M_0\hat{\mathbf{e}}_z + \mathbf{m}(t). \end{aligned} \quad (2.8)$$

We now use a harmonic Ansatz for the oscillating magnetic field  $\mathbf{h}_{\text{rf}}(t)$  and the magnetiza-

tion  $\mathbf{m}(t)$

$$\begin{aligned}\mathbf{h}_{\text{rf}}(t) &= (h_{\text{rf},x}, h_{\text{rf},y}, 0)^T \cdot e^{i\omega t} \\ \mathbf{m}(t) &= (m_x, m_y, 0)^T \cdot e^{i\omega t},\end{aligned}\quad (2.9)$$

By plugging the equations (2.8) and (2.9) into the LLG-equation (2.7). we get the following expression

$$\begin{pmatrix} h_{\text{rf},x} \\ h_{\text{rf},x} \end{pmatrix} = \hat{\chi}_{\text{P}}^{-1} \begin{pmatrix} m_x \\ m_x \end{pmatrix}, \quad (2.10)$$

with the Polder susceptibility  $\hat{\chi}_{\text{P}}$  [36], which describes the linear response of the magnetization  $\mathbf{m}(t)$  to an external perturbation  $\mathbf{h}_{\text{rf}}(t)$ . It has the form [18]

$$\hat{\chi}_{\text{P}}^{-1} = \begin{pmatrix} \chi_{xx} & \chi_{xy} \\ \chi_{yx} & \chi_{yy} \end{pmatrix} = \frac{\mu_0 M_s}{\text{Det}(\hat{\chi}_{\text{P}}^{-1})} \begin{pmatrix} A_{11} & \frac{i\omega}{\gamma\mu_0} \\ -\frac{i\omega}{\gamma\mu_0} & A_{22} \end{pmatrix}, \quad (2.11)$$

with the diagonal entries

$$\begin{aligned}A_{11} &= H_{\text{ext}} + H_{\text{ani}} + M_s \cdot (N_y - N_z) + \frac{i\omega\alpha}{\gamma\mu_0} \\ A_{22} &= H_{\text{ext}} + H_{\text{ani}} + M_s \cdot (N_x - N_z) + \frac{i\omega\alpha}{\gamma\mu_0},\end{aligned}\quad (2.12)$$

where the  $N_i$  are the demagnetization coefficients, which depend on the sample geometry. We can see, that the susceptibility has a dispersive real part  $\chi'$  and a dissipative imaginary part  $\chi''$ . Its behavior as a function of the effective field  $\mathbf{H}_{\text{eff}}$  is shown in Fig. 2.1b). To derive an expression for the resonance frequency  $f_{\text{res}} = \frac{\omega}{2\pi}$  as a function of the external field  $H_{\text{ext}}$ , we solve  $\text{Det}(\hat{\chi}_{\text{P}}) \stackrel{!}{=} 0$ , which gives us the famous Kittel equation [24]

$$f_{\text{res}} = \frac{\gamma\mu_0}{2\pi} \sqrt{[H_{\text{ext}} + H_{\text{ani}} + (N_x - N_z) \cdot M_s][H_{\text{ext}} + H_{\text{ani}} + (N_y - N_z) \cdot M_s]}. \quad (2.13)$$

In the following we want to distinguish between two geometries of a thin film ferromagnetic sample with a length and width in the mm-range but thickness in the nm-regime.

- For the in-plane geometry (ip), the external magnetic field is applied perpendicular to the surface normal, i.e. in the plane of the sample. Now e.g. for the case that the external magnetic field is parallel to the x-axis, the demagnetization coefficients  $N_i$  take the form  $N_x = 1$  and  $N_y = N_z = 0$ . Consequently the Kittel equation (2.13) can be simplified to

$$f_{\text{res}} = \frac{\gamma\mu_0}{2\pi} \sqrt{H_{\text{ext}}(H_{\text{ext}} + M_s)}. \quad (2.14)$$

- Secondly, for the out-of-plane geometry (oop), the external magnetic field  $\mathbf{H}_{\text{ext}}$  is applied parallel to the surface normal. The demagnetization coefficients for this case are  $N_z = 1$  and  $N_x = N_y = 0$ . Plugging this into equation (2.13) and combining the saturation magnetization and the anisotropy field to an effective magnetization  $M_{\text{eff}} = M_s - H_{\text{ani}}$ , we get the following equation:

$$f_{\text{res}} = \frac{\gamma\mu_0}{2\pi} (H_{\text{ext}} - M_{\text{eff}}). \quad (2.15)$$

Solved for the resonance field:

$$\mu_0 H_{\text{res}} = \mu_0 M_{\text{eff}} + \frac{2\pi f}{\gamma}. \quad (2.16)$$

While the real part of the Polder susceptibility gives insight of the relation between the resonance field  $H_{\text{res}}$  and the resonance frequency  $f_{\text{res}}$ , its imaginary part provides information about the damping of the ferromagnetic resonance. By solving the imaginary part of  $\text{Det}(\hat{\chi}_{\text{P}}) \stackrel{!}{=} 0$ , we receive a relation between the resonance frequency  $f_{\text{res}}$  and the ferromagnetic resonance linewidth  $\Delta H$  of the form

$$\mu_0 \Delta H = \frac{2\pi f \alpha}{\gamma}. \quad (2.17)$$

Considering, that this equation (2.17) gives the half-linewidth-at-half-maximum and accounting for the fact that in real experiments, the linewidth does not go to zero at zero frequency, but usually exhibits a finite value, which we call the inhomogeneous linewidth  $H_{\text{inh}}$ , we have to modify equation (2.17) by multiplying a factor of two, in order to get the full-linewidth-at-half-maximum, and adding an inhomogeneous linewidth term  $\mu_0 H_{\text{inh}}$ . The modified equation for the ferromagnetic linewidth as function of microwave frequency has the form

$$\mu_0 \Delta H = \mu_0 H_{\text{inh}} + 2 \cdot \frac{2\pi f \alpha}{\gamma}. \quad (2.18)$$

The emergence of an inhomogeneous linewidth  $\mu_0 \Delta H_{\text{inh}}$  has several possible causes ranging from thermal heating, misalignment issues and inhomogeneities in the thin film sample.

## 2.3 Magnon-phonon coupling

In this section, we describe magnon-phonon coupling. Here, we discuss its phenomenological description and its microscopic origin in Sec. 2.3.1. Furthermore, we establish a theoretical model for a bulk acoustic wave resonator with one Kittel mode coupling to two transverse acoustic phonon modes and derive an expression for the effective coupling strength in the system in Sec. 2.3.2. In the following section 2.3.3 we introduce a theoretical model for a trilayer system with two Kittel modes and one transverse acoustic phonon mode and describe the possibility of even and odd coupling between the two Kittel modes mediated by the transverse acoustic phonon mode. Eventually, in Sec. 2.4 we combine these two models from the previous sections.

### 2.3.1 Phenomenological description

Magnon-phonon coupling or magnetoelastic coupling describes the coupling between the magnetic and elastic system in a magnetically ordered solid. This coupling is mediated by the interplay between the spin-orbit interaction, the magnetic dipole-dipole interaction and the exchange interaction [37]. The following expressions and derivations are taken from Ref. [37]. We can write down a phenomenological expression of the magnetoelastic

energy in cubic crystals with the external magnetic field  $\mathbf{H}_{\text{ext}}$  along the (100) direction

$$\begin{aligned}
 U_{\text{me}} = & \frac{B_1}{M_0^2} \sum_{\mathbf{k}} M_{\mathbf{k}}^2 e_{\mathbf{k}\mathbf{k}} + \frac{B_2}{M_0^2} \sum_{\mathbf{k}} \sum_{\mathbf{l} \neq \mathbf{k}} M_{\mathbf{k}} M_{\mathbf{l}} e_{\mathbf{k}\mathbf{l}} \\
 & + \frac{A_1}{M_0^2} \sum_{\mathbf{k}} \sum_{\mathbf{l}} \sum_{\mathbf{m} \neq \mathbf{l}} \frac{\partial M_{\mathbf{k}}}{\partial x_{\mathbf{l}}} \frac{\partial M_{\mathbf{l}}}{\partial x_{\mathbf{m}}} e_{\mathbf{l}\mathbf{m}} + \frac{A_2}{M_0^2} \sum_{\mathbf{k}} \sum_{\mathbf{l}} \left( \frac{\partial M_{\mathbf{k}}}{\partial x_{\mathbf{l}}} \right)^2 e_{\mathbf{l}\mathbf{l}},
 \end{aligned} \tag{2.19}$$

where  $e_{\mathbf{k}\mathbf{l}} = \frac{1}{2} \left( \frac{\partial u_{\mathbf{k}}}{\partial x_{\mathbf{l}}} + \frac{\partial u_{\mathbf{l}}}{\partial x_{\mathbf{k}}} \right)$  represent the strain tensor elements, with  $\mathbf{u}(\mathbf{r})$  being the displacement vector,  $M_0$  the saturation magnetization and the indices  $\mathbf{k}, \mathbf{l}, \mathbf{m} = x, y, z$ . The parameters  $A_1, A_2, B_1$  and  $B_2$  are the magnetoelastic coupling constants. With these parameters we can calculate the relative change in length of the magnetic crystal along the (100) and (111) directions  $\lambda_{100}$  and  $\lambda_{111}$  as [38]

$$\begin{aligned}
 \left( \frac{\delta l}{l} \right)_{100} &= \lambda_{100} = -\frac{2}{3} \frac{B_1}{C_{11} - C_{12}} \\
 \left( \frac{\delta l}{l} \right)_{111} &= \lambda_{111} = -\frac{B_2}{3C_{44}},
 \end{aligned} \tag{2.20}$$

where the  $C_{ij}$  are the elements of the cubic stiffness tensor.

### 2.3.2 Tripartite magnon-phonon coupling with two non-degenerate phononic modes

The experiments performed in this thesis aim to enable a better understanding of the magnon-phonon coupling between a magnetic thin film sample and transverse acoustic waves in a crystalline sample serving as a bulk acoustic wave resonator (BAW). The samples investigated in this thesis are thin film ferro- or ferrimagnetic materials deposited on different crystalline BAW substrates, as schematically depicted in Fig. 2.2. When the FMR of the magnetic thin film is in resonance, the elliptically polarized Kittel mode generates deformations in the magnetic material, which also induces an interfacial deformation the substrate material, thus injecting acoustic modes in it, which are elliptical shear waves carrying angular momentum[39].

Due to the finite substrate and film thickness (denoted by  $L$  and  $d$ ) and reflective boundary conditions at the opposite interfaces of the sample, we expect the formation of standing waves for certain frequencies  $f_n$ . In our experiments, for transverse acoustic velocities in the order of  $v_t \simeq 1 \frac{\text{km}}{\text{s}}$  and substrate thicknesses in the order of  $L \simeq 100 \mu\text{m}$ , we excite the FMR in the  $f \simeq 10 \text{ GHz}$  range and drive overtone BAW resonances with modenumbers in the order of  $n \simeq 1000$ . In this high overtone regime, the excitation frequency  $f_n$  can be approximated by

$$f_n = \frac{n}{2(d/\tilde{v}_t + L/v_t)}, \tag{2.21}$$

according to Ref. [40], where  $d$  is the thickness and  $\tilde{v}_t$  is the transverse acoustic velocity of the magnetic material. To calculate the effective coupling rate  $g_{\text{eff}}$  between the magnetic and phononic system, we take into account that for arbitrary propagation directions in the host crystal, there are two different perpendicularly polarized transverse acoustic phonon modes with potentially non-degenerate propagation velocities. The following set

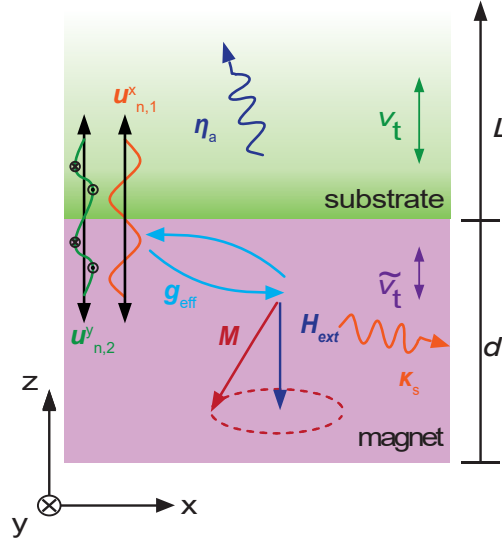


**Figure 2.2:** Schematic illustration of the magnon-phonon coupling mechanism. The precessing magnons of the Kittel mode in the magnet with thickness  $d$  with the damping  $\kappa_s$  couple via an effective coupling rate  $g_{\text{eff}}$  to the phonons  $u_n$  of the non-magnetic substrate with thickness  $L$ . The damping of the non-magnetic substrate/bulk acoustic wave resonator is given by  $\eta_a$ . The expressions  $v_t$  and  $\tilde{v}_t$  are the transverse velocities of the non-magnetic substrate and the magnetic material, respectively.

of equations is adapted from Refs. [41, 42] and expanded for the case of two non-degenerate transverse acoustic phonon modes  $u_{n,1}^+$  and  $u_{n,2}^+$

$$\begin{aligned}
 (\omega - \omega_{\text{mag}} + i\kappa_s)m^+ &= \frac{g_{\text{eff},1}}{2}u_{n,1}^+ + \frac{g_{\text{eff},2}}{2}u_{n,2}^+ + \zeta h^+ \\
 (\omega - \omega_{n,1} + i\eta_{a,1})u_{n,1}^+ &= \frac{g_{\text{eff},1}}{2}m^+ \\
 (\omega - \omega_{n,2} + i\eta_{a,2})u_{n,2}^+ &= \frac{g_{\text{eff},2}}{2}m^+.
 \end{aligned} \tag{2.22}$$

Here,  $\omega_{\text{mag}}$  is the magnetic resonance frequency and  $\omega_{n,1/2}$  is the excitation frequency of the BAW standing waves from the two transverse phonon modes in the substrate according to (2.21). The variables  $u_{n,1/2}^+$  and  $m^+$  are the circularly polarized elastic waves ( $u_{n,1/2}^+ = u_{n,1/2}^x + iu_{n,1/2}^y$ ) and circularly polarized magnetization amplitudes ( $m^+ = m_x + im_y$ ), respectively. Furthermore  $h^+ = h_x + ih_y$  is the oscillating driving field of the microwave stripline inductively coupled at the rate  $\zeta$  to the magnetization  $m^+$ . Now we solve equation (2.22) for  $m^+$  and obtain

$$m^+ = -\frac{h^+(\omega - \omega_{n,1} + i\eta_{a,1})(\omega - \omega_{n,2} + i\eta_{a,2})\zeta}{[g_{\text{eff},1}^2/4(\omega - \omega_{n,2} + i\eta_{a,2}) + g_{\text{eff},2}^2/4(\omega - \omega_{n,1} + i\eta_{a,1}) - (\omega - \omega_{\text{mag}} + i\kappa_s)(\omega - \omega_{n,1} + i\eta_{a,1})(\omega - \omega_{n,2} + i\eta_{a,2})]}. \tag{2.23}$$

We rewrite this expression to

$$m^+ = -\frac{h^+\zeta}{(\omega - \omega_n) - g_{\text{eff},1}^2(\omega - \omega_{n,1})/N_1(\omega) - g_{\text{eff},2}^2(\omega - \omega_{n,2})/N_2(\omega) + i \cdot (\kappa_s + g_{\text{eff},1}^2\eta_{a,1}/N_1(\omega) + g_{\text{eff},2}^2\eta_{a,2}/N_2(\omega))}, \tag{2.24}$$

where we have defined  $N_{1/2} = 4[(\omega - \omega_{n,1/2})^2 + \eta_{a,1/2}^2]$ . In this form, it becomes evident the imaginary part in the denominator of (2.24) can be interpreted as a modified magnetic damping rate  $\tilde{\kappa}_s$  given by

$$\tilde{\kappa}_s = \kappa_s + g_{\text{eff},1}^2 \eta_{a,1} / N_1(\omega) + g_{\text{eff},2}^2 \eta_{a,2} / N_2(\omega). \quad (2.25)$$

Assuming both phononic modes couple equally to the magnetic system ( $g_{\text{eff},1} = g_{\text{eff},2} = g_{\text{eff}}$ ) and utilizing the following relation for the magnetic relaxation rate  $\kappa_s$

$$\kappa_s = \frac{1}{2} \gamma \mu_0 \Delta H_0, \quad (2.26)$$

we solve equation (2.25) for the effective coupling rate  $g_{\text{eff}}$  of the phononic mode 1, i.e.  $\omega = \omega_{n,1}$

$$g_{\text{eff}} = \sqrt{2\gamma\mu_0[\Delta H(\omega = \omega_{n,1}) - \Delta H_0] \cdot \frac{1}{\frac{1}{\eta_{a,1}} + \frac{\eta_{a,2}}{\Delta\omega^2 + \eta_{a,2}^2}}}, \quad (2.27)$$

where  $\Delta\omega = |\omega_{n,1} - \omega_{n,2}|$  is the difference between the two acoustic resonance frequencies. For the phononic mode 2, i.e.  $\omega = \omega_{n,2}$ , an analogue expression for  $g_{\text{eff}}$  to equation (2.27) is obtained, where each of the variable subscripts needs to be changed from 1 to 2. For the case that  $\Delta\omega \ll \eta_{a,1}, \eta_{a,2}$  we can interpret the fraction in Eq. (2.27) as an effective acoustic damping rate

$$\eta_{a,\text{eff}} \approx \frac{1}{\frac{1}{\eta_{a,1}} + \frac{1}{\eta_{a,2}}} = \frac{\eta_{a,1}\eta_{a,2}}{\eta_{a,1} + \eta_{a,2}}. \quad (2.28)$$

Therefore we get for the effective coupling rate

$$g_{\text{eff}} = \sqrt{2\eta_{a,\text{eff}}\gamma\mu_0[\Delta H(\omega = \omega_{n,1}) - \Delta H_0]}, \quad (2.29)$$

which corresponds to the formula given by Müller et al. in Ref. [20]. With equations (2.27) and (2.29), we are now able to calculate the effective coupling rate in our experiments by extracting the change in linewidth, which we call magnetoelastic linewidth  $\Delta H_{\text{me}}$ , at the respective acoustic resonance frequencies  $\Delta H_{\text{me}} = \Delta H(\omega = \omega_{n,1}) - \Delta H_0$  and from the acoustic damping  $\eta_{a,i}$  of each mode, which can be determined from off-magnetic resonance cuts to the microwave transmission as will be discussed in greater detail in the following chapters.

### 2.3.3 Tripartite magnon-phonon coupling with two magnetic layers

In the previous section we established a theoretical description of a tripartite magnon-phonon system with two non-degenerate transverse acoustic phonon modes. Now we investigate a trilayer system with two identical magnetic layers deposited on both sides of a crystalline substrate with degenerate phononic modes, which allows us to utilize  $u_n^+ = u_x + iu_y$ . We want to study the interaction between the two magnetic layers through magnon-phonon coupling. As a first step, we assume a propagation of the standing waves along a crystalline axis, where the two transverse acoustic phonon modes are degenerate (i.e.  $\omega_{n,1} = \omega_{n,2}$ ). The following derivations will closely follow the previous works in

Refs. [21, 41]. We can model the dynamics with the following set of equations adapted from [41]

$$\begin{aligned}
(\omega - \omega_{\text{mag},1} + i\kappa_s)m_1^+ &= \frac{g_{\text{eff},1}}{2}u_n^+ + \zeta_1 h^+ \\
(\omega - \omega_{\text{mag},2} + i\kappa_s)m_2^+ &= \frac{g_{\text{eff},2}}{2}u_n^+ + \zeta_2 h^+ \\
(\omega - \omega_n + i\eta_a)u_n^+ &= \frac{g_{\text{eff},1}}{2}m_1^+ + \frac{g_{\text{eff},2}}{2}m_2^+.
\end{aligned} \tag{2.30}$$

where  $u_n^+$ ,  $m_1^+$  and  $m_2^+$  represent the circularly polarized elastic wave and magnetization amplitudes for the top and bottom magnetic layers. The frequencies  $\omega_{\text{mag},1}$  and  $\omega_{\text{mag},2}$  are the resonance frequencies for the respective magnetization amplitudes, which are driven at a frequency  $\omega$  and the oscillating driving field  $h^+$  coupled inductively to each of the magnetic layers with a coupling rate  $\zeta_i$ . For the case of tripartite coupling with two magnetic layers, we need to distinguish the coupling for even and odd mode numbers  $n$  of the bulk acoustic wave due to the fact, that when  $n$  is even, the excitation field  $h^+$  and the circularly polarized elastic wave  $u_n^+$  are in phase, which corresponds to constructive interference, which leads to a absorption in power, whereas for the case, that  $n$  is an odd integer the circularly polarized elastic wave  $u_n^+$  are  $180^\circ$  out of phase, which corresponds to destructive interference and therefore a reflection of the bulk acoustic wave at the top layer [41]. Consequently, for even mode numbers the effective coupling strength  $g_{\text{eff},i}$  in both magnetic layers is the same (i.e.  $g_{\text{eff},1} = g_{\text{eff},2}$ ) and for odd mode numbers the effective coupling strengths have opposite signs (i.e.  $g_{\text{eff},1} = (-1)g_{\text{eff},2}$ ).

When solving Eq.(2.30) for  $m_1^+$ , we obtain

$$m_1^+ = \frac{-\zeta_1 h^+}{f(\omega)}. \tag{2.31}$$

Again the imaginary part of the denominator can be interpreted as a modified magnetic damping rate  $\text{Im}\{f(\omega)\} = \tilde{\kappa}_s$

$$\begin{aligned}
\tilde{\kappa}_s &= -\frac{\zeta_1}{N(\omega)} \left\{ \frac{g_{\text{eff},1}^2}{2}(\omega - \omega_{\text{mag},2}) - \frac{g_{\text{eff},2}^2}{2}(\omega_{\text{mag},1} + \omega) - (\omega_{\text{mag},1} + \omega) [\eta_a \kappa_s - (\omega - \omega_n)(\omega - \omega_{\text{mag},2})] \right. \\
&\quad \left. - \kappa_s [\eta_a(\omega - \omega_{\text{mag},2}) + \kappa_s(\omega - \omega_n)] \right\} \cdot \zeta_1 [\eta_a(\omega - \omega_{\text{mag},2}) + \kappa_s(\omega - \omega_n)] \\
&\quad - \frac{\zeta_1}{N(\omega)} \left\{ -\frac{g_{\text{eff},1}^2}{2}\kappa_s - \frac{g_{\text{eff},2}^2}{2}\kappa_s - \eta_a \kappa_s^2 + \kappa_s(\omega - \omega_n)(\omega - \omega_{\text{mag},2}) \right. \\
&\quad \left. + (\omega - \omega_{\text{mag},1}) [\eta_a(\omega - \omega_{\text{mag},2}) + \kappa_s(\omega - \omega_n)] \right\} \\
&\quad \cdot \left\{ -\frac{g_{\text{eff},1}g_{\text{eff},2}}{2}\zeta_2 + \frac{g_{\text{eff},2}^2}{2}\zeta_1 + \zeta_1 [\eta_a \kappa_s - (\omega - \omega_n)(\omega - \omega_{\text{mag},2})] \right\},
\end{aligned} \tag{2.32}$$

with  $N(\omega)$

$$N(\omega) = \left\{ -\frac{g_{\text{eff},1}g_{\text{eff},2}}{2}\zeta_2 + \frac{g_{\text{eff},2}^2}{2}\zeta_1 + \zeta_1\eta_a\kappa_s - \zeta_1(\omega - \omega_n)(\omega - \omega_{\text{mag},2}) \right\}^2 + \left\{ \zeta_1\eta_a(\omega - \omega_{\text{mag},2}) + \zeta_1\kappa_s(\omega - \omega_n) \right\}^2. \quad (2.33)$$

We are now interested in the case  $\omega = \omega_{\text{mag},1} = \omega_{\text{mag},2} = \omega_n$ . The equation (2.32) simplifies to

$$\tilde{\kappa}_s(\omega = \omega_{\text{mag},1} = \omega_{\text{mag},2} = \omega_n) = \frac{\zeta_1\kappa_s \left( \frac{g_{\text{eff},1}^2}{2} + \frac{g_{\text{eff},2}^2}{2} + \eta_a\kappa_s \right)}{-\frac{g_{\text{eff},1}g_{\text{eff},2}}{2}\zeta_2 + \frac{g_{\text{eff},2}^2}{2}\zeta_1 + \zeta_1\eta_a\kappa_s}. \quad (2.34)$$

For the uncoupled case ( $g_{\text{eff},1} = g_{\text{eff},2} = 0$ ) we get for the damping  $\tilde{\kappa}_s = \kappa_s$  as naively expected. Now we want an expression to differentiate between the two cases of even and odd coupling between the two magnetic layers. By using  $g_{\text{eff},1} = (-1)^n g_{\text{eff},2}$  and  $\zeta_2 = x \cdot \zeta_1$ , where  $x \in [0, 1]$ , we obtain the modified magnetic damping rates  $\tilde{\kappa}_s$

- Even:

$$\tilde{\kappa}_s = \frac{\kappa_s(g_{\text{eff},1}^2 + \eta_a\kappa_s)}{g_{\text{eff},1}^2(1-x)/2 + \eta_a\kappa_s} > \kappa_s. \quad (2.35)$$

- Odd:

$$\tilde{\kappa}_s = \frac{\kappa_s(g_{\text{eff},1}^2 + \eta_a\kappa_s)}{g_{\text{eff},1}^2(1+x)/2 + \eta_a\kappa_s} > \kappa_s. \quad (2.36)$$

We see, that the modified damping  $\tilde{\kappa}_s$  is enhanced due to phonon pumping in the substrate for both even and odd acoustic modes. Furthermore, in the case of even coupling,  $\tilde{\kappa}_s$  is larger than for the odd case due to the constructive interference between  $h^+$  and  $u_n^+$ .

## 2.4 Quarpartite coupling

In the previous two sections, we introduced tripartite coupling between one Kittel mode and two transverse acoustic phonon modes and tripartite coupling between two Kittel modes and one transverse acoustic phonon mode. Now we want to write down a set of equations, which takes both two magnetic layers and two different perpendicularly polarized phonon modes with potentially different acoustic velocities into account. The dynamic set of equations, which then describes the magnetoelastic coupling is given by

$$\begin{aligned} (\omega - \omega_{\text{mag},1} + i\kappa_s)m_1^+ &= \frac{g_{\text{eff},1}}{2}u_{n,1}^+ + \frac{g_{\text{eff},2}}{2}u_{n,2}^+ + \zeta_1 h^+ \\ (\omega - \omega_{\text{mag},2} + i\kappa_s)m_2^+ &= \frac{g_{\text{eff},2}}{2}u_{n,1}^+ + \frac{g_{\text{eff},1}}{2}u_{n,2}^+ + \zeta_2 h^+ \\ (\omega - \omega_{n,1} + i\eta_{a,1})u_{n,1}^+ &= \frac{g_{\text{eff},1}}{2}m_1^+ + \frac{g_{\text{eff},2}}{2}m_2^+ \\ (\omega - \omega_{n,2} + i\eta_{a,2})u_{n,2}^+ &= \frac{g_{\text{eff},2}}{2}m_1^+ + \frac{g_{\text{eff},1}}{2}m_2^+. \end{aligned} \quad (2.37)$$

It is possible to solve the Eqs. (2.37) for  $m_1^+$ , like we did in the previous sections, but the explicit form of this equation is not elucidative. Furthermore, in this thesis, the samples

with a magnetic layer deposited on both sides show a sufficiently high overlap between their two transverse acoustic phonon modes so we instead use the simpler model utilizing two magnon modes and one phonon mode in Sec. [2.3.3](#).



### 3 Experimental procedure

In this chapter, we describe the fabrication process of our samples utilizing DC magnetron sputtering in the SUPERBOWL sputtering machine. Furthermore, we explain the measurement technique and the experimental setup used for the ferromagnetic resonance experiments. The experimental procedure closely follows the description of previous works in WMI [18, 35, 43].

#### 3.1 Sample fabrication

First we want to describe the fabrication of  $\text{Co}_{25}\text{Fe}_{75}$  thin films, which is used for most samples in this thesis. The growth of these thin films is performed via DC magnetron sputtering utilizing the SUPERBOWL sputtering machine shown in Fig. 3.1.

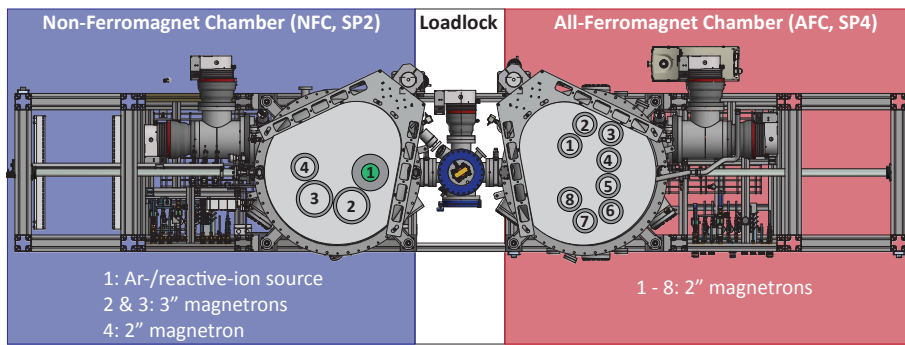


**Figure 3.1:** Illustration of the SUPERBOWL sputtering machine. It consists of two ultra-high-vacuum (UHV) chambers with various target materials installed and a Loadlock for installing and removing samples into the two UHV chambers. Taken from Ref. [35].

First, the sample has to be inserted into the Loadlock, which afterwards is evacuated to a pressure of  $p < 10^{-6}$  mbar before transferring the sample into the SP4 chamber. In the UHV chamber the sample is mounted on a three axes substrate manipulator. For sputtering depositions, Argon gas is injected into the chamber, which is ionized and accelerated towards the target materials by an electric field applied between the target material and an anode ring, forming a plasma state and ejecting atoms from the target material into the chamber. Now the manipulator with the sample is moved over the desired target material (e.g.  $\text{Co}_{25}\text{Fe}_{75}$ ) and the atoms can adhere to the sample surface thus growing a thin film on the substrate. This process is illustrated in Fig. 3.2.

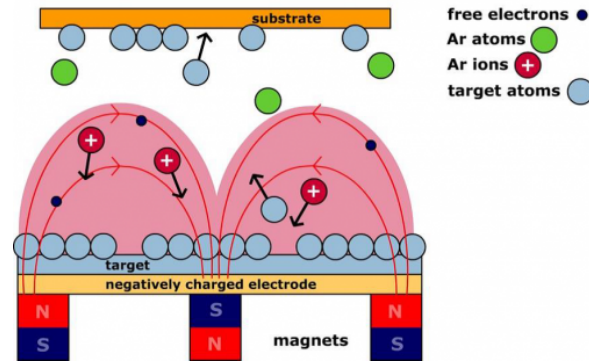


**Figure 3.2:** Schematic of the sputtering process utilizing argon as the inert gas. The argon ions are accelerated towards the target material via an electric field where they collide with the target and eject atoms from its surface, which adhere to the substrate. Permanent magnets beneath the target help stabilizing the argon ion plasma. Taken from [44].

### 3.2 Experimental technique

We used a setup to measure ferromagnetic resonance with a vector network analyzer (VNA-FMR), which consists of the vector network analyzer (VNA) itself, a coplanar waveguide (CPW) and an external magnetic field generated by an electromagnet or superconducting magnet for cryogenic temperatures as shown in Fig 3.3.

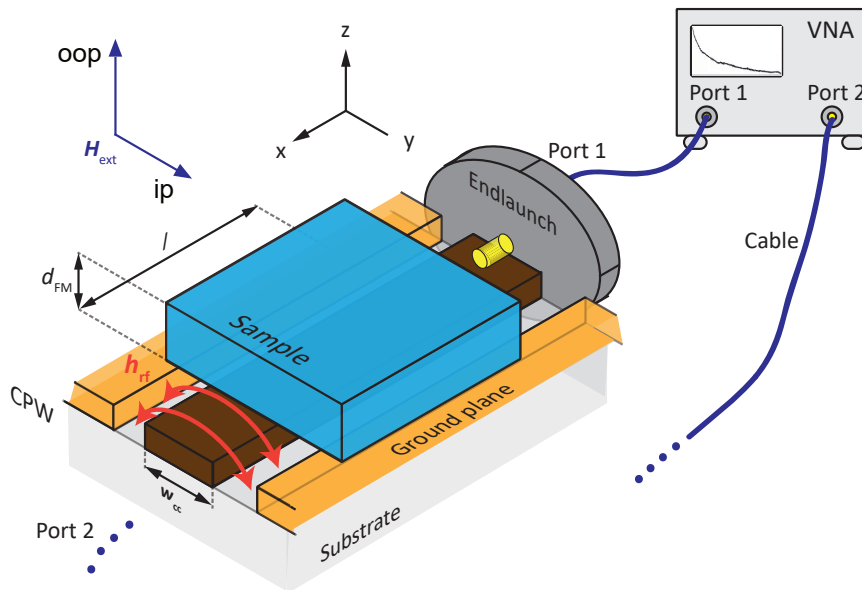


**Figure 3.3:** Schematic diagram for an experimental ferromagnetic resonance setup with a vector network analyzer (VNA). The sample is mounted face-down on the coplanar waveguide (CPW), which is connected on each side to one VNA-port via microwave cables. The VNA creates a sinusoidal microwave signal, which is coupled into the center conductor (CC) of the CPW (brown) through the endlaunches and generates the oscillating magnetic field  $h_{rf}$ . The transmitted signal is detected at port 2 of the VNA. The blue vector indicates the applied magnetic field direction for ip and oop-geometry. Taken from [35].

The sample is placed face down on the CPW and an external magnetic field  $\mathbf{H}_{ext}$  is applied either perpendicular or parallel to the surface normal (see blue arrows in Fig.3.3). In the CPW the microwave signal from the VNA now generates the oscillatory magnetic

field  $\mathbf{h}_{\text{rf}}$ , which excites the magnetization dynamics in the sample. Using the coordinate-system in Fig. 3.3, the rf-field can be approximated by the Karlqvist equations [45]

$$\begin{aligned} h_y(y, z) &= \frac{1}{\pi} \frac{I}{2w_{\text{cc}}} \left( \arctan\left(\frac{y + \frac{w_{\text{cc}}}{2}}{z}\right) - \arctan\left(\frac{y - \frac{w_{\text{cc}}}{2}}{z}\right) \right) \\ h_z(y, z) &= \frac{1}{2\pi} \frac{I}{2w_{\text{cc}}} \ln \left( \frac{(y + \frac{w_{\text{cc}}}{2})^2 + z^2}{(y - \frac{w_{\text{cc}}}{2})^2 + z^2} \right), \end{aligned} \quad (3.1)$$

where  $w_{\text{cc}}$  is the width of the coplanar waveguide and  $I$  is the magnitude of the VNA. When the frequency of the oscillatory magnetic field  $\mathbf{h}_{\text{rf}}$  matches the ferromagnetic resonance frequency  $f_{\text{res}}$  at the given applied external magnetic field  $\mathbf{H}_{\text{ext}}$  according to the Kittel equation (2.13), ferromagnetic resonance is excited. In this case, a current is induced in the CPW by the precessing magnetization according to Faraday's law, hence, energy from the transmitted microwave is absorbed to excite the magnetization dynamics. This can be measured in the complex transmission parameter  $S_{21}$  of the VNA

$$S_{21} = \frac{V_2}{V_1} = \frac{|V_2|}{|V_1|} e^{i(\phi_2 - \phi_1)}, \quad (3.2)$$

which relates the complex voltage  $V_2$  of the microwave signal after transmission measured at port 2 to the complex voltage  $V_1$  of the generated microwave signal at port 1 and their respective phases  $\phi_i$ . By neglecting the back reflected wave  $S_{11} = 0$  and assuming the circuit to be impedance matched, the change in transmission  $\Delta S_{21}$  caused by the FMR in the sample can be calculated as

$$\Delta S_{21} = \frac{S_{21} - S_{21}^0}{S_{21}^0}, \quad (3.3)$$

where  $S_{21}^0$  is the background caused by the frequency-dependent transmission and cable-losses of the setup. We can now account for the change in transmission, when a sample is coupled inductively to the CPW, by assuming a complex inductance  $L_0$  connected in series to the impedance  $Z_0 = 50 \Omega$  of the bare CPW in a simple voltage divider model

$$\Delta S_{21} = -\frac{1}{2} \left( \frac{i\omega L_0}{Z_0 + i\omega L_0} \right) \approx -\frac{i\omega L_0}{2Z_0}, \quad (3.4)$$

where  $\omega$  is the microwave frequency under the assumption that  $\omega L \ll Z_0$ . The factor  $\frac{1}{2}$  is needed because the measurement of  $V_2$  is not between port 1 and 2, but between the CPW and ground [46]. The real-valued inductance  $L_0$  comes from the oscillating magnetic field in the sample. It can be calculated following Ref. [47]

$$\begin{aligned} L_0 &= \frac{\mu_0 l}{w_{\text{cc}} d_{\text{FM}} I^2} \left[ \int_{-\infty}^{\infty} dy \int_{\delta_s}^{\delta_s + d_{\text{FM}}} dz \{ \mathbf{q}(y, z) \hat{\chi}_{\text{P}}(\omega, H_0) \mathbf{h}_{\text{rf}}(y, z, I) \} \right] \\ &\quad \left[ \int_{-\infty}^{\infty} dy \int_{\delta_s}^{\delta_s + d_{\text{FM}}} dz \{ \mathbf{q}(y, z) \mathbf{h}_{\text{rf}}(y, z, I) \} \right] \\ &= \frac{\mu_0 l d_{\text{FM}}}{4w_{\text{cc}}} \chi_{\text{yy}}(\omega, H_0) \eta^2(\delta_s, w_{\text{cc}}), \end{aligned} \quad (3.5)$$

where  $d_{\text{FM}}$  is the thickness of the magnetic material,  $\delta_s$  is the finite distance between sample and CPW,  $\mathbf{q}$  is the normalized amplitude of the Kittel mode and  $\eta(\delta_s, w_{\text{cc}}) = \frac{2}{\pi} \arctan(\frac{w_{\text{cc}}}{2\delta_s})$ ,

which takes values between 0 to 1, when the sample is infinitely far away or in direct contact with the CPW [35]. Now we can use Eqs. (3.4) and (3.5) and plug them into Eq. (3.3) to find an expression for the complex transmission parameter  $S_{21}$

$$\begin{aligned} S_{21}(\omega, H_0) &= S_{21}^0(1 + \Delta S_{21}) = S_{21}^0\left(1 - \frac{i\omega L_0}{2Z_0}\right) \\ &= S_{21}^0\left(1 - \frac{i\omega\mu_0 l d_{\text{FM}}}{8w_{\text{cc}}Z_0}\chi_{yy}(\omega, H_0)\eta^2(\delta_s, w_{\text{cc}})\right) \\ &= S_{21}^0 - iAe^{i\phi}\chi_{yy}(\omega, H_0), \end{aligned} \quad (3.6)$$

where  $A$  includes all the constants and the phase  $\phi$  accounts for the fact that the electrical system has a finite length. This equation (3.6) is only valid for the oop geometry. In the ip geometry we also have to take into account the z-component leaving us with:

$$S_{21}(\omega, H_0) = S_{21}^0 - iAe^{i\phi}\{\chi_{yy}(\omega, H_0) + \chi_{zz}(\omega, H_0)\}. \quad (3.7)$$

In the experiments conducted in this thesis we used a method called frequency-swept FMR, where the external magnetic field  $\mathbf{H}_{\text{ext}}$  is fixed, while sweeping the microwave frequency  $f$ . For our data analysis, it is essential to extract the imaginary and real part of the  $S_{21}$  transmission parameter and fitting them to the Polder susceptibility utilizing Eq. (2.11). Thereby we are able to extract the linewidth  $\Delta H$ , resonance field  $H_{\text{res}}$ , the Gilbert damping parameter  $\alpha$  and the inhomogeneous linewidth  $H_{\text{inh}}$ . Exemplary data for real and imaginary part of the transmission parameter is shown in Fig. 3.4.

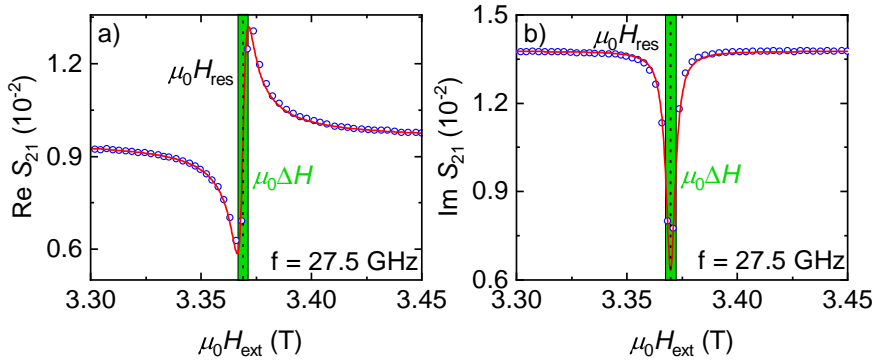


**Figure 3.4:** Raw data of the real a) and imaginary b) part of  $S_{21}$  obtained from a 40 nm  $\text{Co}_{25}\text{Fe}_{75}$  thin film deposited on a  $675 \mu\text{m}$  silicon substrate at  $f = 27.5 \text{ GHz}$  and  $T = 5 \text{ K}$ . The fits of the real and imaginary part (red continuous line) yield the linewidth  $\Delta H$  and the resonance field  $H_{\text{res}}$ .

### 3.3 Experimental setup

To be able to characterize our samples at cryogenic temperatures, we utilized the MORIA liquid helium cryostat, which allows for temperatures in the range of 2 – 300K and high magnetic fields up to 7 T. Our sample is mounted by utilizing an adhesive called ‘Fixogum’ on the coplanar waveguide (CPW) with a center conductor width  $w_{\text{cc}} = 100 \mu\text{m}$  on a copper holder at the end of a Dipstick. To ensure good inductive coupling between sample and CPW, we aimed for a transmission magnitude  $S_{21}$  below  $-30 \text{ dB}$  at  $f = 25 \text{ GHz}$  for the  $\text{Co}_{25}\text{Fe}_{75}$  samples. This dipstick with the sample is then installed into the variable temper-

ature insert and on its top, it is connected to the vector network analyzer (VNA) as shown in Fig. 3.5. The orientation of the sample with respect to the external field can be adjusted via a stepper-motor. With this setup, we can efficiently and with a broad frequency range probe our sample at cryogenic temperatures and high magnetic fields.

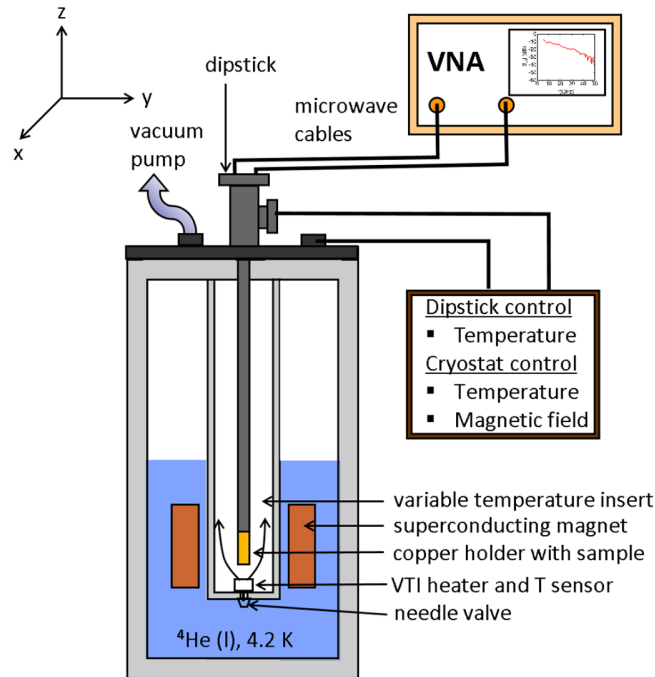


**Figure 3.5:** Schematic of the experimental setup. The cryostat includes a superconducting magnet sitting in a liquid  $^4\text{He}$  bath. Through a needle valve, the variable temperature insert (VTI) regulates the flow of liquid  $^4\text{He}$  into the sample space. A sample heater on the dipstick allows to set a stable temperature. The end of a dipstick contains a copper holder with the sample mounted onto a coplanar waveguide (CPW), which is connected through microwave cables to a vector network analyzer.

An additional heater and temperature sensor at the copper holder of the dipstick itself allows for temperature stabilization and a continuous recording of the sample temperature, which is important because the FMR is very sensitive to changes in temperature and pressure. Most of our measurements were done at  $T = 5\text{ K}$  and a VTI pressure of  $p \simeq 40 - 50\text{ mbar}$ .



## 4 Temperature dependence of magnetoelastic coupling in YIG/GGG heterostructures

Yttrium iron garnet (YIG) grown on a gadolinium gallium garnet (GGG) substrate is known for its low magnetic damping properties at room temperature and therefore a established material platform for the realization of possible spintronic applications in the field of magneto-optics with the potential for coherent information processing [48, 49]. Recently, due to the low sound attenuation constants in YIG grown on GGG substrates, YIG/GGG bulk acoustic resonators have gained interest for applications in quantum information [50–52], especially in the direction of frequency conversion of quantum states. Previous experiments investigated magnon-phonon coupling in YIG-GGG heterostructures at room temperatures in the oop-geometry [41, 42]. Here, on top of room temperature experiments, we also performed FMR experiments at cryogenic temperatures in the oop- and ip-configuration and compare their performances throughout the entire temperature range.

In this chapter, we study the magnetoelastic coupling as function of temperature and frequency for a sample consisting of a 200 nm thin YIG film epitaxially grown on a 500  $\mu\text{m}$  thick GGG substrate with a (111)-orientation. First, in Sec. 4.1, we detail the data analysis procedure performed to calculate the relevant parameters to describe the magnetoelastic coupling. Secondly, in Sec. 4.2, we study and discuss the differences of the magnetoelastic coupling for the ip- and oop-geometry, mapped out over a wide temperature range from cryogenic up to room temperatures. Next, in Sec. 4.3, we investigate the temperature-dependent tuning of the phononic resonances from cryogenic up to room temperatures. Finally, in Sec. 4.4, we take a detailed look at the frequency dependence of the magnetoelastic coupling at  $T = 5$  K for the ip-configuration and  $T = 300$  K for the oop-configuration.

### 4.1 Data analysis for YIG/GGG magnetoelastic coupling

In this section, we describe how we extract the experimental parameters, which characterize the magnon-phonon coupling such as the magnetoelastic linewidth  $\Delta H_{\text{me}}$ , the acoustic damping rate  $\eta_{\text{a}}$  and the magnetic damping rate  $\kappa_{\text{s}}$  from our raw data. Via Equations (2.27), (2.29), and the later defined Eqs. (4.8) and (4.10), these quantities in turn allow to calculate the effective coupling strength  $g_{\text{eff}}$ , the cooperativity  $C = g_{\text{eff}}^2/\eta_{\text{a}}\kappa_{\text{s}}$  and the magnetoelastic coupling parameters  $B_{\text{oop,ip}}$ .

In Fig. 4.1, the data analysis procedure for a YIG/GGG sample at a temperature  $T = 5$  K is exemplary shown. Fig. 4.1 a) shows a colormap of the normalized magnitude of the transmission parameter  $(\text{norm.})|S_{21}| = S_{21}/S_{21}^0$  in a frequency range of 10 MHz around  $f_0 = 7$  GHz. The Kittel mode (dark brown color) and also the avoided crossings of the acoustic modes with the Kittel mode are clearly visible. The avoided crossings show a periodic pattern with a frequency splitting of  $f_{\text{FSR}} = 3.44$  MHz, called the ‘free-spectral-range’ (FSR). For a GGG substrate thickness of  $L = 500$   $\mu\text{m}$  and a transverse velocity of  $v_{\text{t}} = 3568 \frac{\text{m}}{\text{s}}$  [40] this value corresponds well to theory predictions (see Eq. (2.21)). The dark-yellow and cyan horizontal lines represent cuts through  $(\text{norm.})|S_{21}|$  at constant frequency, which are plotted in panel b), where the resonance field  $H_{\text{res}}$  is obtained from fits of the imaginary and real part of the complex transmission parameter  $S_{21}$  to the Polder

susceptibility as defined previously in Sec. 3.2. The dark-yellow data points, representing an on-acoustic resonance cut for  $(\text{norm.})|S_{21}|$ , exhibit a larger linewidth than the off-acoustic resonance cyan datapoints. As established in the theory part Sec. 2.3.2, the difference between the on- and off-resonant FMR-linewidth is interpreted as the magnetoelastic linewidth  $\Delta H_{\text{me}}$ . In panel c), the FMR-linewidth  $\Delta H$ , which is obtained from the fitting of the Polder susceptibility to the imaginary and real part of the transmission parameter  $S_{21}$ , is plotted as a function of the microwave frequency. We clearly see peaks in  $\Delta H$  at the respective frequencies  $f_{n,i}$ , where the transverse acoustic phonon modes cross the Kittel mode. The height of these peaks in reference to the FMR-linewidth  $\mu_0\Delta H_0$ , which is illustrated by the purple line, again is given by  $\Delta H_{\text{me}}$ , whereas the off-resonant FMR-linewidth  $\Delta H_0$  is related to the uncoupled magnetic damping rate  $\kappa_s$  of the system via [20]

$$\kappa_s = \frac{1}{2}\gamma\mu_0\Delta H_0, \quad (4.1)$$

where the factor  $\frac{1}{2}$  stems from the fact that the magnetic damping rate is defined as the half width at half maximum. The black vertical line near the Kittel mode in panel a) corresponds to a cut at constant magnetic field, shown in panel d). We see two dips in the normalized transmission parameter  $(\text{norm.})|S_{21}|$ , which come from the two transverse acoustic phonon modes. Naively, one would expect that along the (111)- direction the two transverse acoustic phonon velocities are degenerate and only one dip in the normalized transmission parameter  $(\text{norm.})|S_{21}|$  would occur. However, due to a small miscut of the substrate the transverse acoustic phonon modes are not propagating along this high symmetry axis and therefore have different sound velocities, which leads to a splitting of the transverse acoustic phonon modes due to slightly different free-spectral-ranges  $f_{\text{FSR}}$ , which is called phononic birefringence [19]. Here, the sum of two Lorentzian functions is fitted to the two dips in order to extract the acoustic damping rates  $\eta_{a,i}$  as also done in Ref. [53]. The difference in the center frequencies of the fits  $\Delta f$  is shown as a black arrow in panel d).

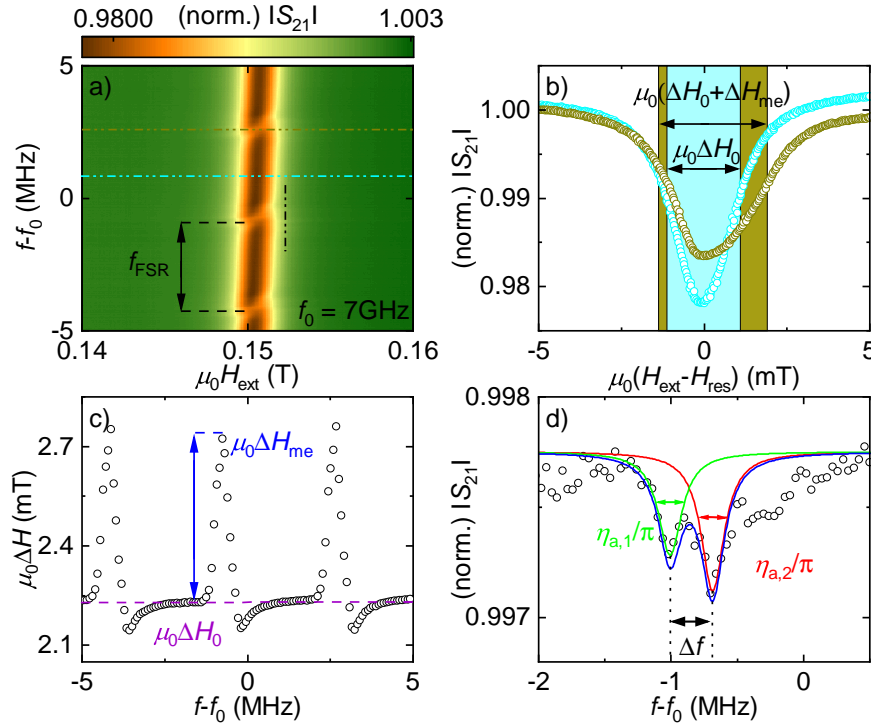


**Figure 4.1:** Data analysis procedure with exemplary data for the complex transmission parameter  $S_{21}$  for YIG/GGG in the ip-geometry at  $T = 5$  K. Panel a) shows a normalized microwave transmission amplitude (norm.)  $|S_{21}|$  around  $f_0 = 7$  GHz and  $H_{\text{ext}} = 0.15$  T. Periodic avoided crossings of the Kittel mode and phonon modes are clearly visible and their difference in frequency, the free spectral range  $f_{\text{FSR}}$ , is indicated as black arrows. The two colored horizontal lines represent cuts at constant frequency, which are shown in panel b). The cyan (dark-yellow) colored line is a cut out-of-resonance (in-resonance) with the  $n^{\text{th}}$  transverse acoustic phonon mode through (norm.)  $|S_{21}|$ . The difference in their linewidths is the magnetoelastic linewidth  $\Delta H_{\text{me}}$ . The black vertical line is a cut at constant magnetic field, which is shown in panel d). Panel c) displays the linewidth  $\Delta H$  as a function of frequency, where again the magnetoelastic linewidth  $\Delta H_{\text{me}}$  is indicated as the peak height. Panel d) is a vertical cut through (norm.)  $|S_{21}|$  at constant  $H_{\text{ext}}$ , which are off-resonant with the Kittel mode. The sum of two Lorentzians fitted to the two dips allows to extract the acoustic damping rates  $\eta_{a,i}$  for each transverse acoustic mode and their difference in center frequencies.

With these extracted values for the magnetic and acoustic damping rates as well as the magnetoelastic linewidth  $\Delta H_{\text{me}}$  from the raw data, we are now able to calculate the coupling rate  $g_{\text{eff}}$  according to Eq. (2.27), the cooperativities  $C$  and the magnetoelastic coupling parameters  $B_{\text{oop,ip}}$  in the following sections.

## 4.2 Differences of magnetoelastic coupling in the ip/oop geometry

This section is focused on the study of the magnetoelastic coupling in the two different measurement geometries (see Fig. 4.2) ip and oop and their respective temperature dependencies. We report an increase of the effective magnon-phonon coupling rates  $g_{\text{eff}}$  in the ip-geometry and its decrease in the oop-geometry towards lower temperatures.

In Fig. 4.2, we show exemplary data for the complex transmission parameter  $S_{21}$  as a function of the microwave frequency  $f - f_0$  ( $f_0 = 7$  GHz) and the external magnetic field  $\mu_0 H_{\text{ext}}$  for the YIG(200 nm)/GGG(500  $\mu\text{m}$ ) sample at  $T = 5$  K and  $T = 300$  K as well as for both the ip- and oop-geometry.

In Fig. 4.2 a) and b) a sketch of the two measurement geometries is shown. The sample is placed face down onto the CPW with the YIG layer in contact with the CPW. The external magnetic field  $H_{\text{ext}}$  is applied parallel to the surface normal in panel a) and orthogonal to the surface normal and the CPW line in panel b), thus defining the oop and ip-geometry, respectively. We see a small FMR-linewidth  $\Delta H$  in Fig. 4.2 c) and d) of YIG at  $T = 300$  K as expected for YIG [40, 54, 55]. However, for  $T = 5$  K, its FMR-linewidth is significantly higher, because of the FMR-mode coupling to paramagnetic GGG at lower temperatures [56, 57]. Note that the range of the external magnetic field in panels c) and d) is 5 mT around the resonance field and in panels e) and f), it is 20 mT around the resonance field, in order to have a better visual representation of the Kittel modes.

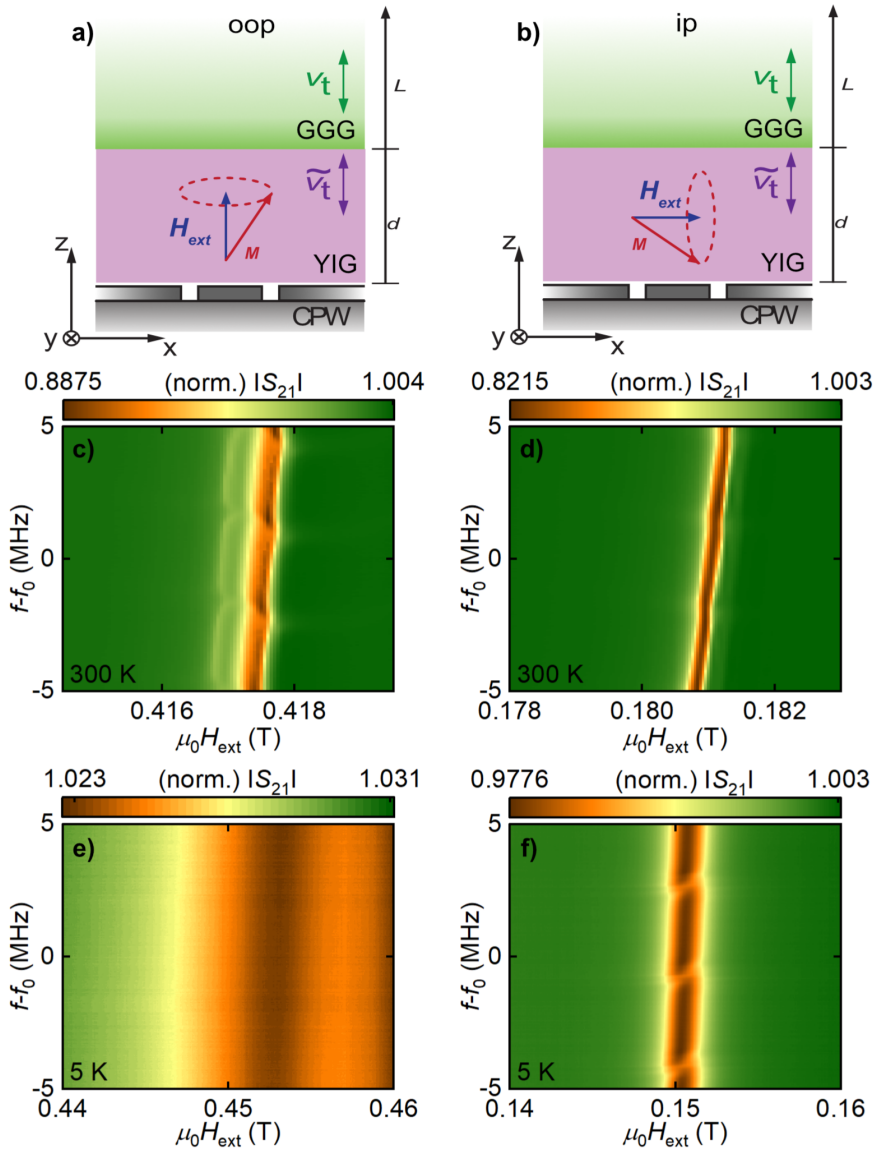


**Figure 4.2:** Schematic representation of the sample in the oop- and ip-geometry in panels a) and b), respectively. Depicted in the graphics are the transverse sound velocities  $v_t$ ,  $\tilde{v}_t$  and the thicknesses of the two materials  $L$ ,  $d$  of GGG and YIG, respectively. Taken from Ref. [19]. In the second and third row (panels c-f)), we show colormaps of the normalized magnitude of the transmission amplitude  $(\text{norm.})|S_{21}|$  at  $f_0 = 7$  GHz. The second row shows RT-data at  $T = 300$  K and the third row shows data at  $T = 5$  K.

From the colormaps in Fig. 4.2, we see, that in ip at  $T = 5$  K, the avoided crossings are much sharper in panel f) than at RT in panel d). For the oop-geometry, we observe clear avoided crossings at RT in panel c), however at cryogenic temperatures in panel e), the linewidth becomes very broad and no signs of an anticrossing with the transverse acoustic phonon modes are visible. When looking at the magnetoelastic linewidth  $\Delta H_{\text{me}}$ , extracted from the raw data as shown in Fig. 4.1 c), for the ip- and oop-geometry in Fig. 4.3 a), we find that the magnetoelastic linewidth increases towards lower temperatures for the ip-geometry (red data), whereas it decreases for the oop-geometry (green data). The local maximum for  $\Delta H_{\text{me}}$  at around  $T = 50$  K may hint at the presence of a slowly-relaxing impurity mechanism in our YIG thin films [17, 54]. The value at  $T = 5$  K for  $\mu_0 \Delta H_{\text{me}}$  for the ip-configuration is roughly four times higher than the maximum value for the oop-configuration at  $T = 300$  K. Furthermore, at around  $T = 150$  K, the magnetoelastic linewidth  $\Delta H_{\text{me}}$  for the ip-geometry becomes larger than for the oop-geometry. This is at first not expected because according to Ref. [39], the impact of magnetoelastic coupling on the FMR-linewidth is expected to be reduced for the ip-configuration compared the oop-configuration. We are going to address this unexpected behavior later in this section.

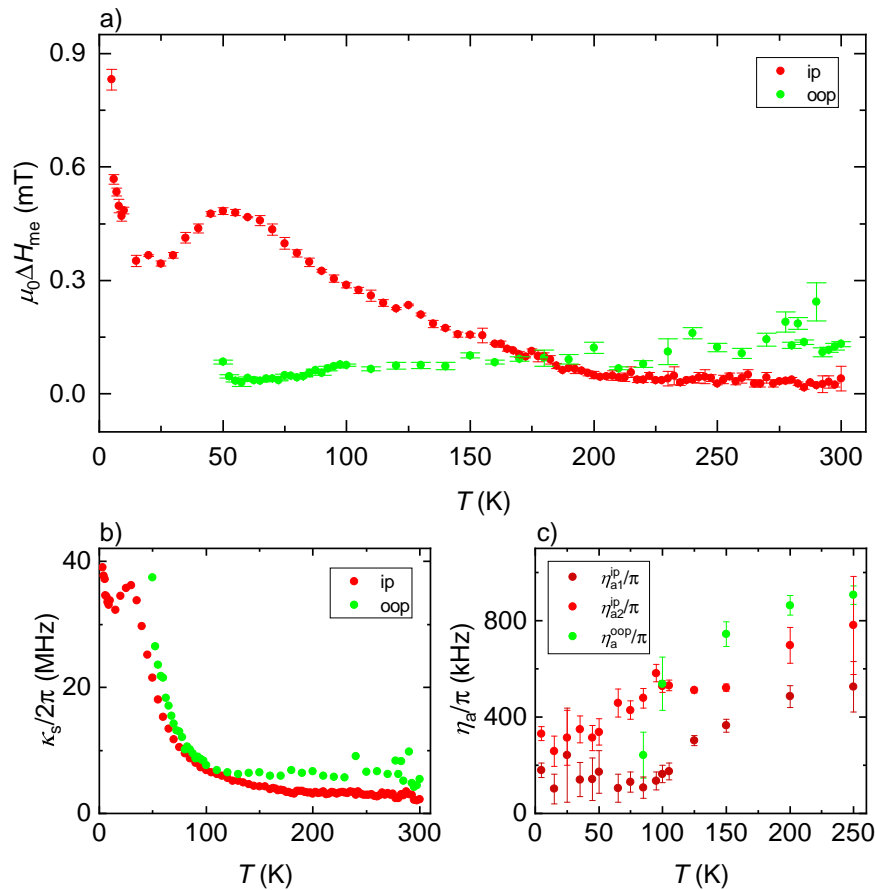


**Figure 4.3:** a) Experimental data for the magnetoelastic linewidth  $\Delta H_{\text{me}}$  in the ip/oop-geometry as a function of the temperature. b), c) Magnetic  $\kappa_s$  and acoustic damping rate  $\eta_a$  in the ip/oop-geometry as a function of the temperature up to  $T = 250$  K. For higher temperatures, fitting the normalized complex transmission parameter (norm.)  $|S_{21}|$  to Eq. (2.25) did not yield reasonable values.

Shown in Fig. 4.3 b) is the temperature dependence of the magnetic damping rate  $\kappa_s$ , which increases in both geometries towards lower temperatures as expected due to coupling of the FMR with the increasing magnetic moment of the paramagnetic GGG at cryogenic temperatures [54]. In panel c), we plot the temperature dependence of the acoustic damping rate  $\eta_a$  for both geometries. In the ip-geometry, we can resolve the two transverse acoustic phonon modes, shown as the red and magenta points in Fig. 4.3 c). The acoustic damping decreases for decreasing temperatures as expected from literature [58, 59]. With these values, we can now calculate the effective coupling strength  $g_{\text{eff}}$  according to Eqs. (2.27) and (2.29) and the cooperativity  $C$ , shown in Fig. 4.4. Here for the ip-configuration, we also see an increase in the effective coupling strength  $g_{\text{eff}}$  and cooperativity  $C$  towards lower temperatures, but with a local maximum for the effective coupling rate in ip around  $T = 65$  K and for the cooperativity at around  $T = 100$  K. While for the oop-configuration, we report a decrease towards lower temperatures. Furthermore, surprisingly, in Fig. 4.4 a), the two calculated values for the effective coupling rates  $g_{\text{eff},1}$  and  $g_{\text{eff},2}$  in the ip-configuration begin to differ significantly for temperatures below  $T \approx 150$  K, while one would naively expect that the transverse acoustic phonon modes should couple equally to the Kittel mode. This may come from the fact, that the two phonon modes in the ip-configuration exhibit different acoustic damping rates  $\eta_{a,i}^{\text{ip}}$  (see Fig. 4.3 c)). However, for elevated temperatures, there is a overlap of the transverse acoustic phonon modes, which makes it difficult to precisely determine the acoustic damping rates  $\eta_{a,i}$ .

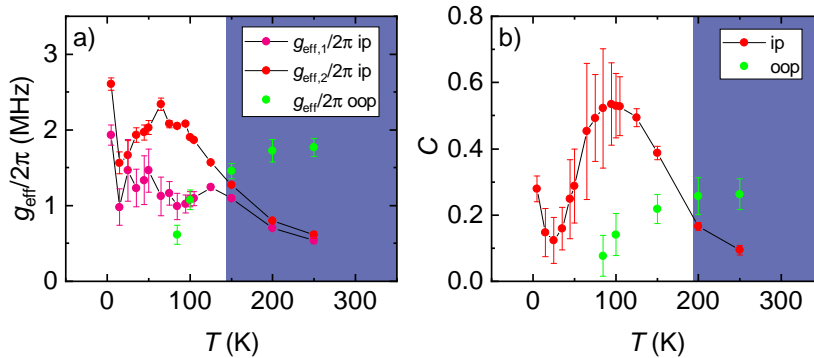


**Figure 4.4:** Extracted effective coupling strength  $g_{\text{eff}}$  a) and the cooperativity  $C$  b) versus the temperature for the ip and oop-geometry. For both panels, the regime, where the values for the oop-geometry are higher than their ip-counterparts, are highlighted by a blue background.

From Fig. 4.4, we conclude, that for temperatures below  $T = 150$  K, the coupling between the phononic and the magnetic system is more efficient in the ip-geometry than in the oop-geometry, as in this temperature range, both the effective coupling strength  $g_{\text{eff}}$  and the cooperativity  $C$  are larger in the ip-configuration than in the oop-configuration.

In the following, we want to explain, how the magnon-phonon coupling rate can become larger in the ip-geometry than the oop-geometry at cryogenic temperatures. To this end, we introduce a theoretical expression for calculating the effective coupling strength  $g_{\text{eff}}$  [18, 41]

$$g_{\text{eff}}(f) = B \sqrt{\frac{2g\mu_B}{hfM_s\tilde{\rho}_t dL}} \left[ 1 - \cos\left(2\pi f \frac{d}{\tilde{v}_t}\right) \right], \quad (4.2)$$

where  $h$  is the Planck constant,  $\tilde{\rho}_t = 5170 \frac{\text{kg}}{\text{m}^3}$  [40] is the volume density of the YIG layer,  $\tilde{v}_t = 3843 \frac{\text{m}}{\text{s}}$  is the transverse sound velocity in YIG [40] and  $d = 200 \text{ nm}$  the thickness of the YIG layer. Furthermore,  $M_s$  is the saturation magnetization of the YIG film and  $L = 500 \mu\text{m}$  the thickness of the GGG substrate. Utilizing Eq. (4.2), we are able to solve  $g_{\text{eff}}(f)$  for the magnetoelastic coupling parameter  $B$  in the oop- and ip-geometry as a function of temperature at a fixed frequency  $f_0 = 7 \text{ GHz}$  and under the assumption, that the volume density  $\tilde{\rho}_t$ , the transverse sound velocity  $\tilde{v}_t$  and the thicknesses  $d$  and  $L$  of YIG and GGG respectively are temperature-independent<sup>1)</sup>. To quantify the temperature dependence of  $M_s$ , separate broadband ferromagnetic resonance experiments have been performed as function of temperature. From these experiments, we find, that the anisotropy field is two orders of magnitude smaller than the effective magnetization [62]. Consequently, we can approximate  $M_s \approx M_{\text{eff}}$ . As a next step, we derive the expressions for the effective magnetoelastic coupling parameters  $B_{\text{oop,ip}}$  for the ip- and oop-configuration.

For a cubic crystal, when the external magnetic field is applied in an arbitrary direction, the expression for the magnetoelastic energy in Eq. (2.19) needs to be transformed into a new coordinate system. The following derivations will closely follow the previous works done by R. C. LeCraw and R. L. Comstock in Ref. [63]. Firstly, we have to express the unit vectors  $\mathbf{e}_i$  of the cubic lattice in the unit vectors  $\mathbf{e}_\nu$  of the new coordinate system, such that  $\mathbf{e}_i = \sum_\nu a_{i\nu} \mathbf{e}_\nu$ . With these coefficients  $a_{i\nu}$  we can transform the strain components  $e_{ij}$  and the magnetization components  $\alpha_i$  to

$$\begin{aligned} e_{ii} &= \sum_{(\nu\mu)} a_{i\nu} a_{i\mu} e_{\nu\mu}, \\ e_{ij} &= \sum_{(\nu\mu)} (a_{i\nu} a_{j\mu} + a_{j\nu} a_{i\mu}) e_{\nu\mu}, \\ \alpha_i &= \sum_\nu a_{i\nu} \alpha_\nu, \end{aligned} \quad (4.3)$$

where  $(\nu\mu)$  represent the Cartesian axis directions, i.e.  $(xx)$ ,  $(yy)$ ,  $(zz)$ ,  $(xy)$ ,  $(xz)$  and  $(yz)$ . The first part of the magnetoelastic energy in Eq. (2.19) can be written as

$$U_{\text{me}} = B_2 \left( \sum_i \alpha_i^2 e_{ii} + \sum_{(ij)} \alpha_i \alpha_j e_{ij} \right) + (B_1 - B_2) \sum_i e_{ii}, \quad (4.4)$$

where the first term is invariant under transformation. Hence, we only need to apply this coordinate transformation for the second term. When the external magnetic field is applied in the (111)-direction (oop), now labeled as the  $z'$ -axis, the  $(\bar{1}\bar{1}2)$ -direction as the  $x'$ -axis and

---

<sup>1)</sup>Note, that, while this is a rough estimate, we nonetheless can expect that these parameters exhibit changes with temperature, which are comparatively small ( $\lesssim 1\%$ , according to Refs. [40, 60, 61]) to that of the magnetoelastic coupling parameter  $B$ .

the  $(\bar{1}\bar{1}0)$  as the  $y'$ -axis, the unit vectors from the cubic lattice are expressed as follows:

$$\begin{aligned}\mathbf{e}_x &= -\frac{1}{\sqrt{6}}\mathbf{e}_{x'} + \frac{1}{\sqrt{2}}\mathbf{e}_{y'} + \frac{1}{\sqrt{3}}\mathbf{e}_{z'}, \\ \mathbf{e}_y &= -\frac{1}{\sqrt{6}}\mathbf{e}_{x'} - \frac{1}{\sqrt{2}}\mathbf{e}_{y'} + \frac{1}{\sqrt{3}}\mathbf{e}_{z'}, \\ \mathbf{e}_z &= \sqrt{\frac{2}{3}}\mathbf{e}_{x'} + \frac{1}{\sqrt{3}}\mathbf{e}_{z'}.\end{aligned}\tag{4.5}$$

Plugging these vectors into Eq. (4.4), the first part of the magnetoelastic energy in Eq.(2.19) becomes [63, 64]

$$\begin{aligned}U_{\text{me}}^{(111)} &= B_2(\alpha_{x'}\alpha_{z'}e_{x'z'} + \alpha_{y'}\alpha_{z'}e_{y'z'}) \\ &+ \frac{2(B_1 - B_2)}{3} \left[ \alpha_{x'}\alpha_{z'} \left( \frac{1}{\sqrt{2}}(e_{x'x'} - e_{y'y'}) + e_{x'z'} \right) \right] + \alpha_{y'}\alpha_{z'} \left( e_{y'z'} - \frac{1}{\sqrt{2}}e_{x'y'} \right),\end{aligned}\tag{4.6}$$

where only the terms linear or quadratic in  $\alpha_{z'}$  are considered, while omitting the terms containing  $e_{z'z'}$  corresponding to the generation of longitudinal phonons.

For a shear strain polarized along the external magnetic field  $\mathbf{H}_{\text{ext}}$ , which are transverse acoustic waves propagating along the  $z$ -axis, the relevant free energy terms are

$$\frac{2B_1 + B_2}{3}(\alpha_{x'}\alpha_{z'}e_{x'z'} + \alpha_{y'}\alpha_{z'}e_{y'z'}),\tag{4.7}$$

where the prefactor is the effective coupling constant for the oop-geometry

$$B_{\text{oop}} = \frac{2B_1 + B_2}{3}.\tag{4.8}$$

For the ip-geometry configuration, the external magnetic field  $\mathbf{H}_{\text{ext}}$  is applied along the  $(\bar{1}\bar{1}2)$ -direction or the  $(\bar{1}\bar{1}0)$ -direction or along a linear combination of the two. Unfortunately, in our experiments we do not know the exact crystalline direction along which the external magnetic field  $\mathbf{H}_{\text{ext}}$  is applied. Hence, we calculate the magnetoelastic energy for both  $(\bar{1}\bar{1}2)$ - and  $(\bar{1}\bar{1}0)$ -direction and again only take into account the terms linear or quadratic in  $\alpha_{z'}$ , while omitting the strain along the  $z'$ -direction  $e_{z'z'}$  corresponding to the

generation of longitudinal phonons

$$\begin{aligned}
U_{\text{me}}^{(\bar{1}\bar{1}2)} &= B_2(\alpha_{x'}\alpha_{z'}e_{x'z'} + \alpha_{y'}\alpha_{z'}e_{y'z'}) \\
&+ (B_1 - B_2) \left[ -\frac{1}{\sqrt{3}}\alpha_{x'}\alpha_{z'} \left( -\frac{1}{\sqrt{3}}e_{x'z'} + \frac{2}{\sqrt{6}}e_{x'y'} \right) \right. \\
&\quad \left. - \frac{\sqrt{2}}{3}\alpha_{y'}\alpha_{z'} \left( e_{x'x'} - \frac{2\sqrt{2}}{3}e_{y'z'} \right) + \frac{1}{6}\alpha_{z'}^2 \left( e_{x'x'} + \frac{2}{3}e_{y'y'} - \frac{\sqrt{2}}{3}e_{y'z'} \right) \right], \\
U_{\text{me}}^{(1\bar{1}0)} &= B_2(\alpha_{x'}\alpha_{z'}e_{x'z'} + \alpha_{y'}\alpha_{z'}e_{y'z'}) \\
&+ (B_1 - B_2) \left[ \left( \frac{2}{\sqrt{6}}\alpha_{x'}\alpha_{z'} - \frac{1}{\sqrt{3}}\alpha_{y'}\alpha_{z'} \right) \left( \frac{2}{\sqrt{6}}e_{x'z'} - \frac{1}{\sqrt{3}}e_{y'z'} \right) \right. \\
&\quad \left. + \alpha_{z'}^2 \left( \frac{1}{3}e_{x'x'} + \frac{1}{6}e_{y'y'} - \frac{\sqrt{2}}{3}e_{x'y'} \right) \right].
\end{aligned} \tag{4.9}$$

In the ip-configuration, the transverse acoustic phonon modes are propagating perpendicular to the direction of the external magnetic field  $\mathbf{H}_{\text{ext}}$ . Hence we are interested in the prefactor of the strain component  $e_{x'y'}$ , which is the effective coupling constant in the ip-configuration. It is interesting to note, that for the two different expressions for the magnetoelastic energy  $U_{\text{me}}$  along the  $(\bar{1}\bar{1}2)$ - and  $(1\bar{1}0)$  crystal direction, the magnetoelastic coupling constant takes the same form

$$B_{\text{ip}} = \frac{\sqrt{2}}{3}(B_2 - B_1). \tag{4.10}$$

Furthermore, in the following, we assume, that the magnetoelastic coupling parameters  $B_1$  and  $B_2$  are temperature-dependent. Hence, by comparing Eqs. (4.8) and (4.10), we find, that for the case  $B_{\text{ip}} > B_{\text{oop}}$  i.e. that the ip magnetoelastic coupling parameter is bigger than its oop counterpart, the magnetoelastic coupling parameters must fulfill the following relation, that  $8.2 \cdot B_1 < B_2$ . With this, we can now calculate the magnetoelastic coupling parameters for the ip- and oop-geometry  $B_{\text{oop,ip}}$ . The results are plotted in Fig. 4.5. The literature values for  $B_{\text{oop,ip}}$  in Fig. 4.5 are calculated from the magnetoelastic coupling parameters  $B_1$  and  $B_2$  using Eqs. (4.8) and (4.10) and those are in turn calculated from the temperature-dependent magnetostriction constants  $\lambda_{100}, \lambda_{111}$  [65] using Eqs. (2.20), where  $C_{11} = 269$  GPa,  $C_{12} = 107.7$  GPa and  $C_{44} = 76.4$  GPa are the entries of the elastic stiffness tensor of YIG, which for this calculation are assumed to be temperature-independent. The literature values for the oop magnetoelastic coupling parameter  $B_{\text{oop,literature}}$  (olive green) are constant at around  $B_{\text{oop,literature}} \approx 5 \times 10^5 \frac{\text{J}}{\text{m}^3}$  over the entire temperature range, while the literature values for the ip magnetoelastic coupling parameter  $B_{\text{ip,literature}}$  (orange) are situated below the oop literature values at  $B_{\text{ip,literature}} \approx 2 \times 10^5 \frac{\text{J}}{\text{m}^3}$  at  $T = 250$  K and increase towards lower temperatures and almost reach the oop magnetoelastic coupling value at  $T = 5$  K.

The experimental data for the oop magnetoelastic coupling parameter  $B_{\text{oop}}$  (green) first has a strong increase towards higher temperatures and then saturates above  $T = 200$  K. The experimental data for the ip magnetoelastic coupling parameters  $B_{\text{ip},1}$  (magenta) and  $B_{\text{ip},2}$  (red) both increase towards lower temperatures and agree well with each other for  $T > 120$  K but then start to split up for lower  $T$ . While  $B_{\text{ip},1}$  has a plateau towards lower

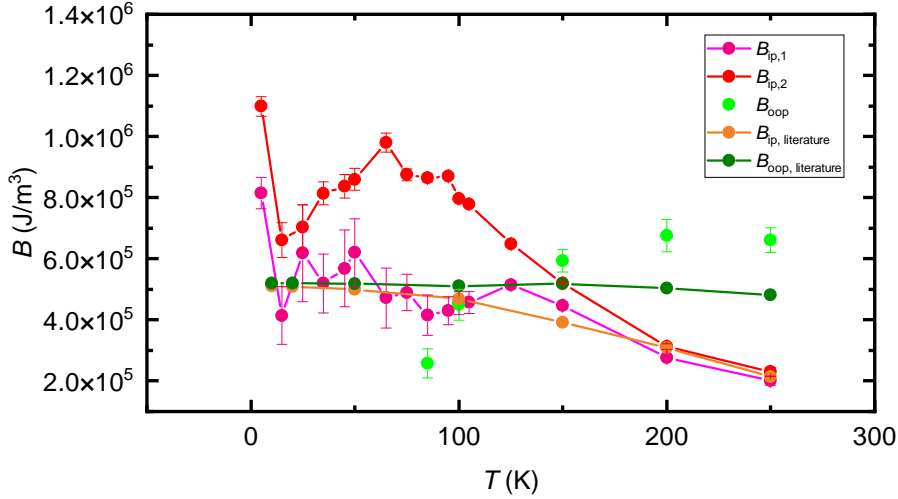


**Figure 4.5:** Temperature dependence of the magnetoelastic coupling parameters  $B_{ip,oop}$  and comparison with literature values from Ref. [66].

temperatures and then strongly increases at  $T = 5$  K,  $B_{ip,2}$  exhibits larger values than  $B_{ip,1}$  for  $T < 120$  K, with a local maximum at around  $T = 60$  K and also increases strongly at  $T = 5$  K. From Fig. 4.5, in analogy to our observations in figures 4.3 and 4.4, we find, that the crossing point, where  $B_{ip,2} > B_{oop}$ , is also situated at around  $T = 150$  K. The values extracted from our experiments in Fig. 4.5 do not quite match the literature values but at least qualitatively  $B_{oop}$  exhibit a similar behavior to the literature curve  $B_{oop,theory}$  from room temperatures down to around  $T = 100$  K. The experimental data for one of the two magnetoelastic coupling parameter  $B_{ip,1}$  matches the literature curve  $B_{ip,theory}$  with good agreement, while the other one  $B_{ip,2}$  is situated well above the literature curve for temperatures below  $T = 150$  K. Possible causes for the disparity of our results for the oop magnetoelastic coupling parameter  $B_{oop}$  and one ip magnetoelastic parameter  $B_{ip,2}$  from theory are, that especially for the oop data, it gets progressively more difficult to determine the acoustic damping rates with reducing temperatures using the method proposed in Sec. 4.1. Also fitting problems arise for the ip-geometry at lower temperatures because the phononic modes split and secondary side modes manifest additionally to the two transverse acoustic phonon modes, which is not accounted for in the model in Sec. 2.3. Moreover, the literature values are for bulk YIG crystals, while in our experiments, we are measuring YIG thin films grown on a GGG substrate, where, despite of the low lattice mismatch between YIG and GGG, there could be additional stresses due to different thermal expansion coefficients.

These difficulties could eventually lead to the drop of the values for  $B_{oop}$  at temperatures below  $T = 100$  K with respect to the theory values  $B_{oop,theory}$ . Furthermore it could also explain the differences in  $B_{ip,1}$  and  $B_{ip,2}$  below  $T = 100$  K. But this needs further investigation and an expansion of the present theoretical model.

### 4.3 Study of the temperature dependent tuning of the phononic resonances

In the next part of this chapter, we investigate the temperature-dependent tuning of the BAW resonances. As is apparent from Fig. 4.2, the avoided crossing features for the ip-

configuration become less prominent in the (norm.) $|S_{21}|$ - data, when going to higher temperatures. Therefore, instead of analyzing the (norm.) $|S_{21}|$ - data, we instead study the temperature-dependence of the phononic peaks in the FMR-linewidth  $\Delta H$  (see Fig. 4.1) in a frequency range of 20 MHz around  $f_0 = 7$  GHz in the ip-geometry, which are visible throughout the entire experimentally investigated temperature range. In Fig. 4.6 a), we plot the magnetoelastic linewidth  $\Delta H_{\text{me}}$  as a function of the frequency  $f - f_0$  with  $f_0 = 7$  GHz and as a function of the temperature  $T$  ranging from 3 K – 300 K. We can clearly see, that the phononic peaks (blue) up to  $T = 25$  K remain at the same resonance frequencies and then start to shift to lower frequencies with increasing temperature at an increasing slope, meaning the free-spectral-range decreases more and more strongly with increasing temperature.

Furthermore, in Fig. 4.6 b), the temperature-evolution of the free-spectral-range is shown for frequencies around  $f_0$  as the black data points. Here,  $f_{\text{FSR}}$  is extracted as the frequency spacing of the peaks in  $\Delta H_{\text{me}}$  in panel a). We observe a reduction of the FSR with increasing temperature, which we associate as discussed above to the change in acoustic properties and dimensions of the GGG BAW resonator. We model the temperature-dependence of  $f_{\text{FSR}}$  using Eq.(2.21), where we need to account for the thermal expansion of the GGG substrate thickness  $L(T)$  and the temperature-dependent transverse sound velocity  $v_t(T) = \sqrt{G(T)/\rho(T)}$ , where  $\rho$  is the material density and  $G$  is the shear modulus of the material. It was shown in previous works [18, 20], that literature values for the temperature dependent parameters  $G(T)$ ,  $\alpha^*(T)$  and  $\rho(T)$  plugged into Eq.(2.21) mimic the experimentally measured  $f_{\text{FSR}}$  with good agreement. Unfortunately to our knowledge, there exist only values for the thermal expansion coefficient  $\alpha^*(T)$  [67] and no temperature dependent values of the shear modulus  $G(T)$  and the density  $\rho(T)$  of GGG have been published in literature. Hence, we cannot precisely map  $f_{\text{FSR}}$  in Fig. 4.6b) to Eq.(2.21). Thus we account only for the thermal expansion of GGG from  $\alpha^*(T)$  in Eq.(2.21) and show the results of these calculations as red data points in Fig. 4.6 b) with constant transverse sound velocity  $v_t$  and shear modulus  $G$  over the whole temperature range. Note, that we only consider the temperature dependence of the acoustic properties of the GGG substrate, as the thickness  $d = 200$  nm of the YIG layer is rather small compared to the thickness  $L = 500$   $\mu\text{m}$  of the GGG substrate and hence the YIG layer has a negligible impact on  $f_{\text{FSR}}$ .

When comparing the temperature-dependence of the experimental data  $f_{\text{FSR}}$  and the from literature values extracted data for the free-spectral-range  $f_{\text{FSR}}^{\text{literature}}$ , we find that both decrease monotonically towards higher temperatures. However, we do not obtain a quantitative agreement and the slope of the temperature evolution is considerably different for our experimental data as compared to our simple model. We attribute these deviations to the fact that we could not account for the temperature dependence of the volume density  $\rho$  and the shear modulus  $G$ , which are connected with the transverse sound velocity  $v_t$ , hence, introduce a temperature dependence for the transverse sound velocity  $v_t$ . We expect that with knowledge of these temperature-dependent parameters, a good quantitative agreement between experiment and model can be obtained.

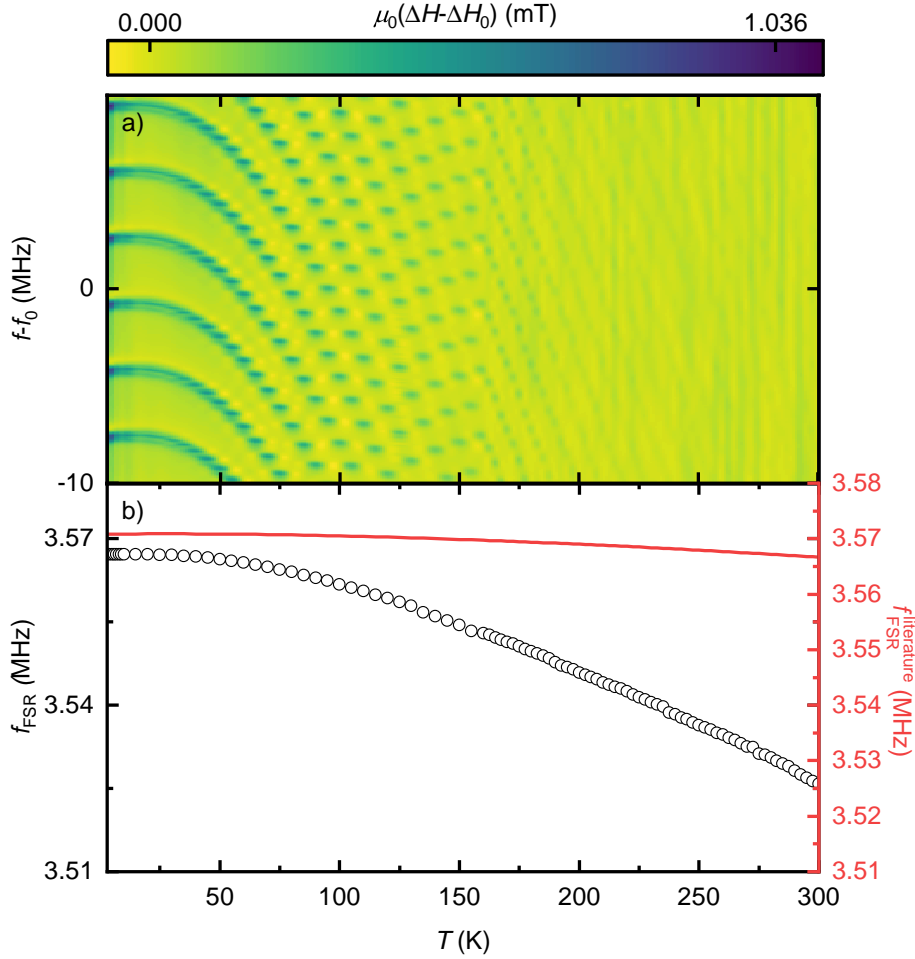


**Figure 4.6:** a) Colormap of the magnetoelastic linewidth evolution  $\Delta H_{me}$  around  $f_0 = 7$  GHz as function of the temperature. b) Plot of the extracted free spectral range  $f_{FSR}$  as function of temperature (black data) and a plot of the free spectral range calculated with literature values for only the thermal expansion coefficient (red data).

#### 4.4 Frequency dependence of the magnetoelastic coupling

Finally, in this section, we briefly discuss the results of the frequency-dependence of the magnetoelastic coupling in YIG/GGG for the ip- and oop-configuration at  $T = 5$  K and  $T = 300$  K, respectively. At these temperatures the effective magnetoelastic coupling rates  $g_{eff}$  are the largest for their respective geometry configurations as shown in Sec. 4.2. For this purpose, we characterize the magnetoelastic coupling for the ip-geometry at center frequencies ranging from  $f_0 = 4$  GHz to  $f_0 = 15$  GHz with a distance of  $\Delta f = 1$  GHz and for the oop-geometry from  $f_0 = 3$  GHz to  $f_0 = 9$  GHz at frequency-steps of  $\Delta f = 1$  GHz, while recording  $S_{21}$  around the resonance field in a frequency-window of 10 MHz. In Fig. 4.7 a), the frequency-dependence of the acoustic damping rates for both geometries are shown, where there are two data sets for the ip-geometry, because of the splitting of the two transverse acoustic phonon modes. The acoustic damping rates increase quadratically

with frequency as expected from Refs. [53, 68]. The data is fitted with a quadratic function

$$\eta_a(f) = \eta_a^0 + \xi f^2, \quad (4.11)$$

following Ref. [53]. We find a good agreement between Eq. (4.11) and our experimental results. From the fit we obtain the following parameters, shown in Tab. 4.1.

	$\eta_a^0/\pi$ [kHz]	$\xi/\pi$ [1/GHz]
300 K oop	$135.9 \pm 51.8$	$14.5 \pm 1.5$
5 K ip mode 1	$342.3 \pm 50.8$	$3.7 \pm 0.5$
5 K ip mode 2	$96.1 \pm 27.5$	$1.2 \pm 0.2$

**Table 4.1:** Fitted values for the acoustic damping rates  $\eta_a$  in Fig. 4.7 a) according to Eq. (4.11).

The value for the  $\xi$  parameter is in good agreement with the value from Ref. [53], while the inhomogeneous phonon linewidth  $\eta_a^0$  is about half the value in Ref. [53]. This is attributed to the fact, that the YIG thin film investigated in Ref. [53] is about three times thicker than the one investigated in this thesis. Hence, we infer, that the acoustic damping rate is impacted strongly by the FM thin film layer. For the ip values for the phononic damping rates at  $T = 5$  K, we see significant differences in the inhomogeneous phononic linewidths  $\eta_a^0$  and  $\xi$ . This means that one transverse acoustic phonon mode is intrinsically more strongly damped in this geometry. Unfortunately, to our knowledge, there do not exist literature values for the transverse acoustic phonon damping rates of GGG at cryogenic temperatures.

In panel b), the frequency-dependence of the magnetic damping rates  $\kappa_s$  from the ip- and oop-geometry are shown. We find, that they increase linear with frequency as expected from Eq. (2.18). The extracted parameters for the Gilbert damping  $\alpha$  are  $\alpha_{\text{oop}} = 4.8 \times 10^{-5}$  for the oop-geometry and  $\alpha_{\text{ip}} = 7.7 \times 10^{-4}$  for the ip-geometry, which is in good agreement with literature values (see Ref. [54, 69–71]). In panel c) the effective coupling rate, which is calculated from Eqs. (2.27) and (2.29), is plotted as a function of frequency. The ip-effective coupling rate  $g_{\text{eff1}}^{5\text{K,ip}}$  at  $T = 5$  K is larger over the entire frequency range than the oop-coupling rate at  $T = 300$  K, thus showcasing, that the magnetoelastic coupling for the ip-geometry at cryogenic temperatures is more efficient than for the oop-geometry at room temperature. Furthermore, the theoretical frequency-dependent coupling rates, calculated from Eq. (4.2), are shown as continuous lines (gray, dark red, dark green), where we use  $\rho_t = 5170 \frac{\text{kg}}{\text{m}^3}$  [40] for the volume density of the YIG layer,  $\tilde{v}_t = 3843 \frac{\text{m}}{\text{s}}$  as the transverse sound velocity [40],  $d = 200$  nm as the thickness of the YIG layer and  $\mu_0 M_s = 172$  mT as the saturation magnetization of YIG at room temperature and  $\mu_0 M_s = 242$  mT, both values for the saturation magnetization  $\mu_0 M_s$  are extracted from broadband FMR experiments, for YIG at  $T = 5$  K. Furthermore, for the theory curves of  $g_{\text{eff}}^{300\text{K,oop}}/2\pi$  and  $g_{\text{eff1}}^{5\text{K,ip}}/2\pi$ , we used  $B_{\text{oop}} = 6.6 \times 10^5 \frac{\text{J}}{\text{m}^3}$  and  $B_{\text{ip,1}} = 1.1 \times 10^5 \frac{\text{J}}{\text{m}^3}$  as calculated in the previous Sec. 4.2. For the second ip effective coupling rate  $g_{\text{eff2}}^{5\text{K,ip}}/2\pi$  we achieved good matching between theory and experiment for  $B_{\text{ip,2}} = 7.6 \times 10^5 \frac{\text{J}}{\text{m}^3}$ , which is in good agreement to the in Sec. 4.2 calculated value of  $B_{\text{ip,2}} = 8.1 \times 10^5 \frac{\text{J}}{\text{m}^3}$ .

The theoretical curves show good agreement with our data up to  $f = 9$  GHz, but differ from the data significantly for higher frequencies which could be due to a lower value for

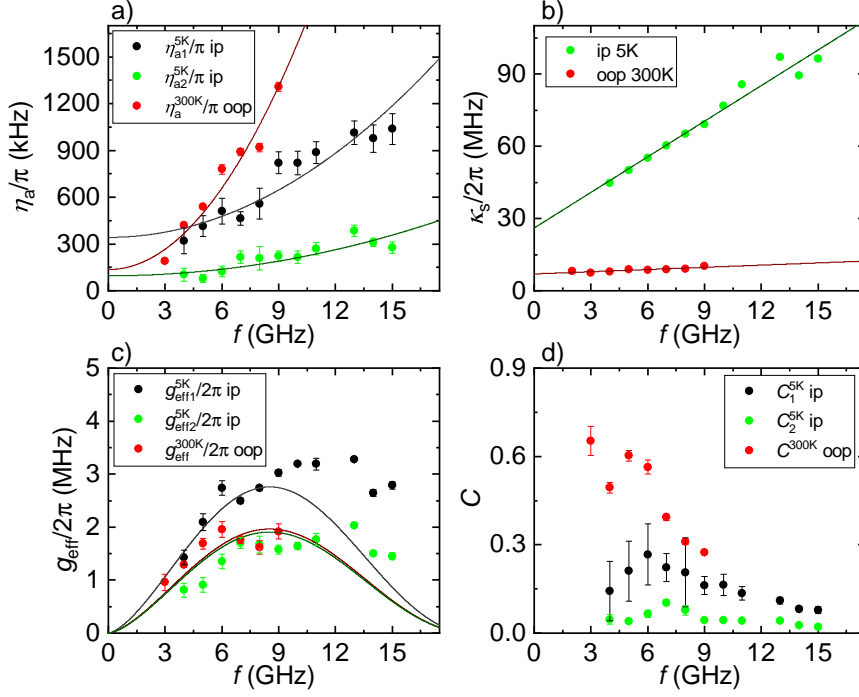


**Figure 4.7:** a) Acoustic damping rate  $\eta_a$  as a function of the microwave frequency. The continuous lines represent a theory model for the acoustic damping rate as a function of frequency. b) Magnetic damping rate  $\kappa_s$  as a function of the microwave frequency. The continuous lines represent a linear fit curve according to the theory in Sec. 2.2. c) The calculated data for the effective coupling rates  $g_{\text{eff}}$  using Eq. (2.27) are shown. The continuous lines represent a theory model following Eq. (4.2). d) Calculated cooperativity as a function of the microwave frequency.

$d_{\text{YIG}}$ . Finally, in panel d), the cooperativity  $C$  is plotted as a function of the microwave frequency. Here, the cooperativity for the oop-geometry at room temperatures is larger than the ip-geometry cooperativity at  $T = 5\text{K}$  due to the fact, that the room temperature oop magnetic damping rates are much smaller for the oop-configuration than ip magnetic damping rates at cryogenic temperatures (see panel b)). Since the effective coupling strength  $g_{\text{eff}}$  is throughout the entire frequency range higher than the acoustic damping rates  $\eta_a$ , but lower than the magnetic damping rates  $\kappa_s$ , we enter the Purcell regime ( $\eta_a < g_{\text{eff}} < \kappa_s$ ) as defined in Ref. [72].

## 5 Dependence of the magnetoelastic coupling on the orientation of the substrate in CoFe/Sapphire heterostructures

In the previous chapter 4, we have encountered a resonance-frequency splitting of the two transverse acoustic BAW resonator modes, which we attribute to a small miscut of the YIG-GGG sample leading the transverse acoustic waves to propagate not exactly parallel to the (111)-direction, but at a slight angle [19]. This leads to a frequency splitting of the orthogonally polarized standing wave phonon modes, because their group velocities are no longer degenerate and therefore their induced standing waves in the BAW resonator exhibit different free-spectral-ranges. We label this phenomenon, analog to optical birefringence [73, 74], as a phononic birefringence effect [19]. Now we want to investigate this birefringence effect and study to what extent it is possible to control it in the substrate material.

In this chapter we investigate the magnetoelastic coupling between a  $\text{Co}_{25}\text{Fe}_{75}$  thin film deposited on different sapphire ( $\text{Al}_2\text{O}_3$ ) substrates with different crystalline orientations. In Sec. 5.1, we explain the hexagonal crystal system and how the different planes of orientation lie in the unit cell. Furthermore we study the degeneracy of the transverse acoustic sound velocities for an arbitrary direction in the hexagonal crystal system and calculate the difference in the fast and slow transverse sound velocity as a function of the propagation direction. We also show experimental data that verifies the non degeneracy of the transverse sound velocities in two certain crystalline directions. In Sec. 5.2, we study the frequency dependence of the magnetoelastic linewidth  $\Delta H_{me}$ , as defined in Sec. 4.1, for both cryogenic temperatures  $T = 5$  K and room temperatures  $T = 300$  K. Lastly in Sec. 5.3, we focus on the temperature dependence of various parameters like the magnetic  $\kappa_s$  and acoustic  $\eta_a$  damping rates, the Gilbert damping parameters  $\alpha$  and the inhomogeneous linewidths  $\mu_0 H_{inh}$  for each of the substrates with different crystalline orientations.

### 5.1 Crystalline direction dependence of the transverse acoustic sound velocity

In this section, we want to investigate this phononic birefringence effect of the two transverse acoustic phonon modes and their sound velocities by studying the phononic birefringence effect for sapphire substrates ( $\text{Al}_2\text{O}_3$ ) that are grown in crystalline directions for which we expect a significant splitting of the phonon modes.

In Fig. 5.1, a schematic of the hexagonal close packed (hcp) crystal structure of sapphire with two unit cells is depicted. This figure displays the three different crystalline orientations c-plane (dark blue), a-plane (light blue) and r-plane (violet) and their corresponding surface normal. The unit vectors  $a_1$ ,  $a_2$ ,  $a_3$  and  $c$  used in the hexagonal crystal system are shown as black arrows. These allow us to define the different planes with Miller indices [5]: (0001) for the c-plane, (0 $\bar{1}$ 10) for the a-plane and (0 $\bar{1}$ 12) for the r-plane.

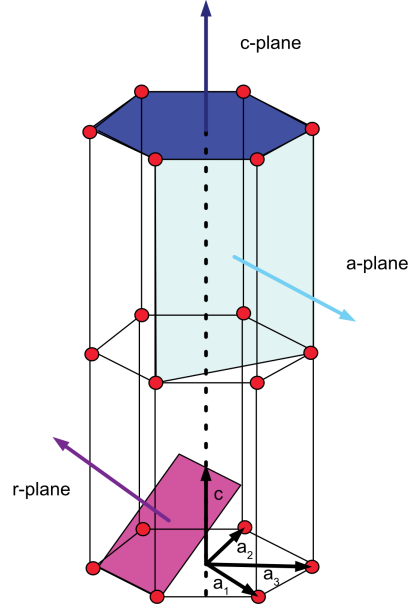


**Figure 5.1:** Schematic of a hexagonal crystal lattice with 2 unit cells stacked on top of each other. The unit vectors  $a_1$ ,  $a_2$ ,  $a_3$  and  $c$  of the hexagonal unit cell are depicted as black arrows in the bottom of the lower unit cell. The c-plane (dark blue). Its normal vectors are represented arrows in their respective colors.

In the following, we study the splitting of the so called slow and fast transverse acoustic sound velocities as a function of the crystal direction. These velocities can be computed by solving the Christoffel equation [75, 76]

$$\sum_{lm} \left( \sum_{ij} q_i C_{ijklm} q_j - \rho \omega^2 \delta_{lm} \right) u_m = 0, \quad (5.1)$$

where  $\rho$  is the volume density of the material,  $\omega$  the angular frequency,  $\mathbf{q}$  the wave vector,  $\delta_{lm}$  is the Kronecker delta and  $\mathbf{C}$  the stiffness tensor. We use the entries for the stiffness tensor and the volume density  $\rho$  of sapphire to numerically solve the christoffel equation using the python tool developed in Ref. [76]. In Fig. 5.2, we show a 3D color plot of the velocity difference  $\Delta v_t$  of the fast and slow transverse acoustic sound velocities as a function of the propagation direction. Furthermore, the surface normal vectors for the different planes in the hexagonal lattice system are depicted by black arrows. For the propagation of the two transverse acoustic phonon modes along the c-plane surface normal, we expect a degeneracy of the two velocities, i.e.  $\Delta v_t = 0$ . Along the surface normal of the r-plane, we expect  $\Delta v \approx 95 \frac{\text{m}}{\text{s}}$  and along the a-plane surface normal  $\Delta v \approx 990 \frac{\text{m}}{\text{s}}$ .

For our study of the impact of phononic birefringence on the magnetoelastic coupling in sapphire, we fabricated two samples with  $d = 35$  nm thick  $\text{Co}_{25}\text{Fe}_{75}$  sputter-deposited on top of both sides polished a-plane and r-plane sapphire ( $\text{Al}_2\text{O}_3$ ) substrates and performed ferromagnetic resonance experiments at room temperatures. In Fig. 5.3, we show data for the normalized complex transmission parameter  $(\text{norm.})|S_{21}|$  measured around  $f_0 = 9$  GHz in a range of 100 MHz and as a function of the external magnetic field  $\mu_0 H$  in a range of 60 mT around the resonance field  $H_{\text{res}}$  of  $\text{Co}_{25}\text{Fe}_{75}$  at  $f_0 = 9$  GHz. We observe a multitude of avoided crossings of the transverse acoustic phonon modes of both samples, which notably

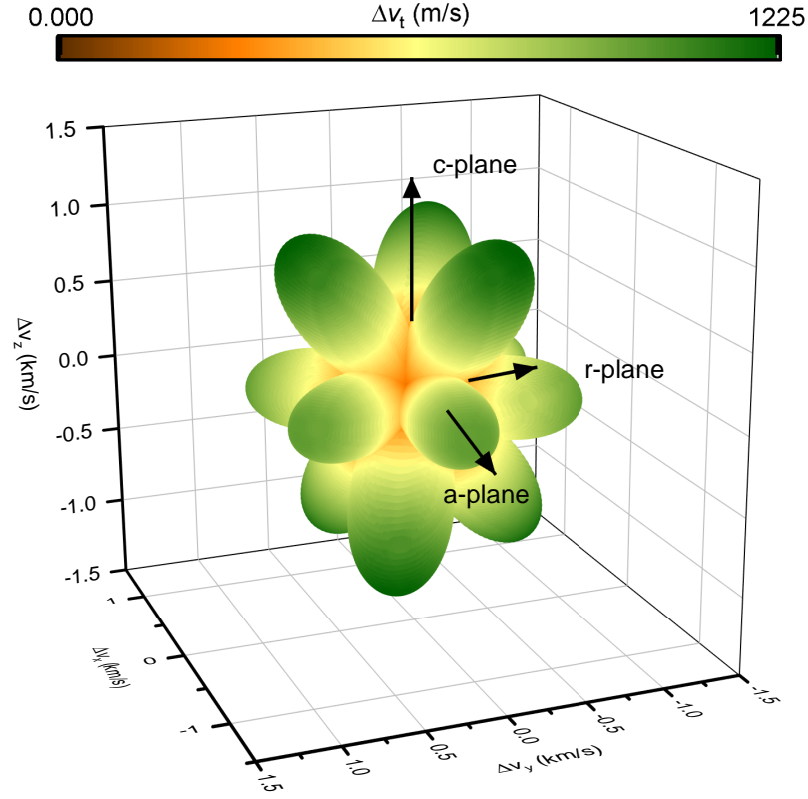


**Figure 5.2:** 3D color plot of the difference  $\Delta v_t$  in transverse acoustic sound velocities depending on the propagation direction in the hexagonal lattice structure of sapphire. The different planes in the hexagonal crystal system are represented by their normal as black arrows.

do not exhibit one singular frequency-periodicity. Panel a) shows the data for the a-plane substrate, where black arrows highlight some of the avoided crossings. We clearly see avoided crossing features with two different free spectral ranges  $f_{\text{FSR},1} = 5.2 \text{ MHz}$  and  $f_{\text{FSR},2} = 6.1 \text{ MHz}$ , described by Eq. (2.21), which leads the features to merge and drift apart periodically in frequency. In panel b), corresponding measurement data for the r-plane substrate, using the same settings as in panel a), is shown. We again see two periodic avoided crossing features with different free spectral range, however they drift apart in frequency at a slower rate, meaning the difference in the two free-spectral-ranges  $f_{\text{FSR}}$  of the fast and slow transverse phonons is lower than in the a-plane. This is expected, as the difference in the transverse sound velocities for the r-plane direction is smaller than for the a-plane direction, meaning that also the difference in the free spectral range is smaller, which causes the transverse acoustic phonon modes to marginally drift apart as a function of frequency.

We extract the free spectral ranges and consecutively the fast and slow transverse sound velocities by taking a vertical cut at constant field through the Kittel mode and plotting the normalized complex transmission parameter (norm.)  $|S_{21}|$  as a function of the frequency  $f - f_0$ . Then the respective differences in frequencies of two consecutive peaks are averaged and the velocity of the two acoustic modes is calculated via Eq. (2.21) using the substrate

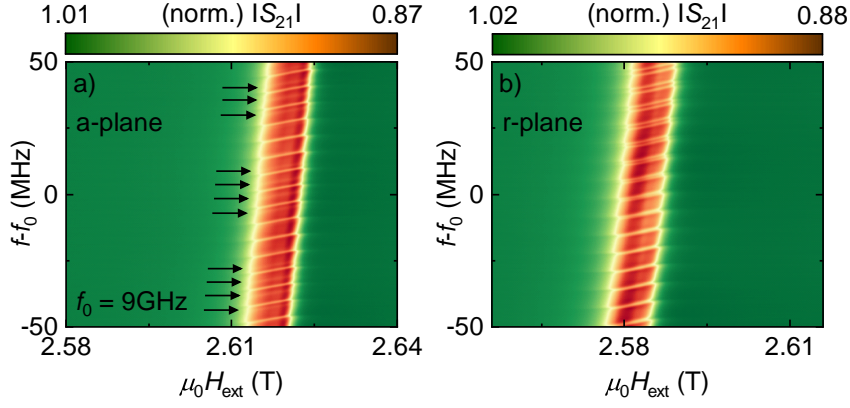


**Figure 5.3:** Colormaps of the normalized complex transmission parameter (norm.) $|S_{21}|$  as a function of the external magnetic field  $\mu_0 H_{\text{ext}}$  in a range of 60 mT and the microwave frequency  $f - f_0$  around  $f_0 = 9$  GHz in a range of 100 MHz for the CoFe/a-plane sapphire (a) and CoFe/r-plane sapphire (b) samples. Multiple periodic avoided crossings of the transverse acoustic phonon modes with the Kittel mode are visible. For panel a), in order to better visualize these avoided crossings, some are indicated via black arrows.

thickness of  $L = 500 \mu\text{m}$ . The extraction of the free-spectral-ranges is shown in Fig. 5.4 for the a-plane sample, where we plot a cut of the normalized complex transmission parameter (norm.) $|S_{21}|$  at the resonance field  $H_{\text{res}}$ . The values for the fast and slow transverse acoustic sound velocities and their differences in velocity are listed in Tab. 5.1.

	a-plane	r-plane
$v_{\text{st}}$ [m/s]	$5171 \pm 40$	$6493 \pm 150$
$v_{\text{ft}}$ [m/s]	$6053 \pm 40$	$6693 \pm 42$
$\Delta v$ [m/s]	$882 \pm 80$	$200 \pm 192$

**Table 5.1:** Values for the fast and slow transverse acoustic sound velocities for the two different sapphire substrates and their differences in velocity.

The differences in velocity are approximately in the same range we expected from the solution of the Christoffel equation (5.1) plotted in Fig. 5.2. This agreement confirms the validity of the underlying magnetoelastic model (see Sec. 2.3.2) and confirms that we can control the velocity difference of the fast and slow transverse phonon modes by selecting a certain crystal orientation of the substrate.

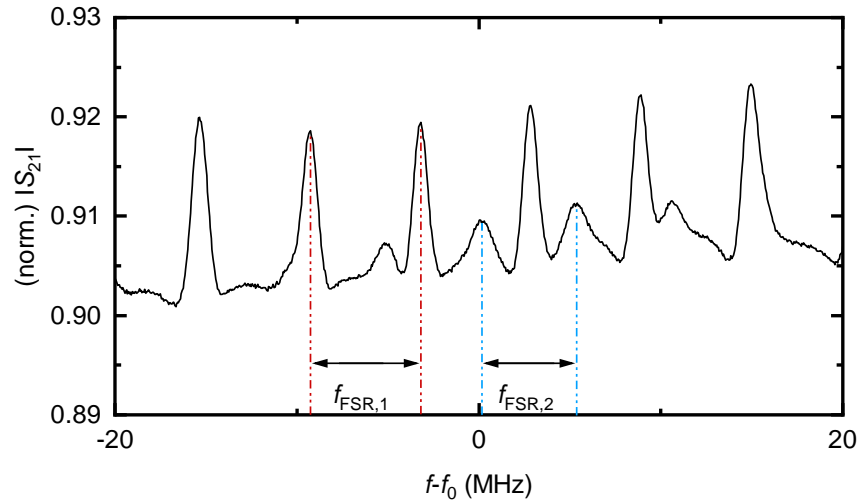


**Figure 5.4:** Plot of a vertical cut of  $(\text{norm.})|S_{21}|$  at the resonance field  $H_{\text{res}}$  as a function of the microwave frequency  $f - f_0$  around  $f_0 = 9$  GHz. The colored vertical lines represent the two free-spectral-ranges  $f_{\text{FSR},i}$ .

## 5.2 Frequency dependence of the magnetoelastic linewidth

In this section, we study the magnetoelastic linewidth, as defined in Sec. 4.1 and its frequency dependence at room temperature  $T = 300$  K and at cryogenic temperatures  $T = 5$  K. For this purpose, we performed FMR-experiments for three different samples of  $\text{Co}_{25}\text{Fe}_{75}$  deposited on sapphire, which differ in the crystalline orientation of the sapphire substrate (c-plane, a-plane, r-plane), as defined in Fig. 5.1 In detail, we conducted the experiments in a frequency span ranging from  $f_0 = 9$  GHz up to 18 GHz in steps of 0.5 GHz in a range of 20 MHz around  $f_0$ . Furthermore, we carried out the room temperature measurements for the CoFe/c-plane sample studied in Ref. [19, 20] at frequencies ranging from 6 GHz up to 19.5 GHz in steps of 1.5 GHz. The FMR-experiments at room temperature are using an electromagnet capable of generating magnetic fields of up to  $\mu_0 H_{\text{ext}} = 3$  T. Hence, using this room temperature setup, we could not study the magnetoelastic coupling for frequencies above  $\simeq 20$  GHz, where the resonance field of CoFe exceeds 3 T. However, using a superconducting magnet capable of generating magnetic fields of up to 7 T, the measurements at cryogenic temperatures were performed at 6 GHz up to 39 GHz in steps of 3 GHz for the a-plane and r-plane sample, due to time constraints we could not perform frequency-dependent measurements at room temperature in this setup. For the c-plane sample the measurements were done from 6 GHz up to 42 GHz in steps of 6 GHz.

In Fig. 5.5 a), we plot the magnetoelastic linewidth as a function of the microwave frequency  $f$  at room temperature  $T = 300$  K for the three different samples with different crystalline orientation of the substrate (c-plane (black), a-plane (red), r-plane (green)). The magnetoelastic linewidth for the c-plane sample (black data) is near zero, which we attribute to the high acoustic damping rate of the transverse acoustic phonon modes propagating along the c-axis direction. The magnetoelastic linewidth  $\Delta H_{\text{me}}$  for the a-plane sample (red data) increases with frequency until it has a maximum at  $f = 10$  GHz and then

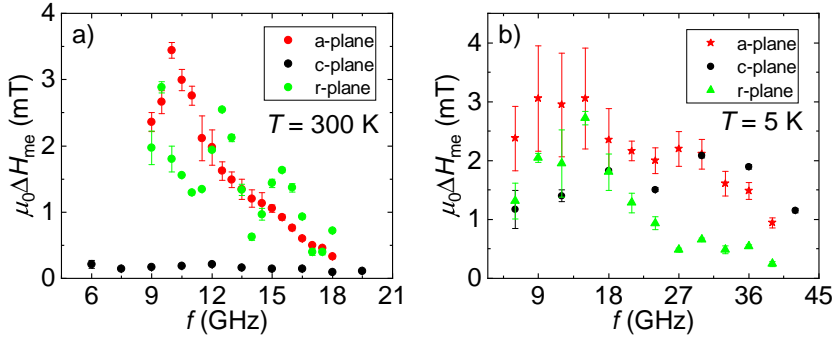


**Figure 5.5:** Magnetoelastic linewidth  $\Delta H_{me}$  as a function of the microwave frequency  $f_0$  for the samples with different crystalline orientations of the substrate at room temperature  $T = 300$  K (panel a) and at cryogenic temperature  $T = 5$  K (panel b).

decreases with frequency and approaches zero. The magnetoelastic linewidth for the r-plane sample (green data) overall decreases with increasing frequency but it oscillates with a period of  $f = 3$  GHz. This effect comes from the periodic merging of the two transverse acoustic phonon modes due to their different free-spectral-ranges as already discussed in the previous Sec. 5.1. This periodic overlaying of the two transverse phonon modes leads to an increase of the magnetoelastic linewidth  $\Delta H_{me}$ , which is visible in Fig. 5.5.

Overall we can conclude, that magnetoelastic coupling at room temperature is more efficient for the a-plane and r-plane sapphire sample compared to the c-plane sapphire sample, which we attribute to lower elastic damping rates. This finding is of interest for room-temperature experiments on the magnon-phonon coupling in sapphire.

In Fig. 5.5 b), we plot the magnetoelastic linewidth  $\Delta H_{me}$  as a function of the microwave frequency  $f$  at cryogenic temperature  $T = 5$  K for the three different samples. The magnetoelastic linewidth  $\Delta H_{me}$  for the c-plane sample (black circles) is nearly constant. The data for the a-plane sample (red circles) has a slight frequency dependence and decreases towards higher frequencies, and the data of the r-plane sample (green circles) increases with frequency until it reaches a maximum at 15 GHz and then decreases to almost zero for higher frequencies. As compared to the room temperature data in panel a), all three samples seem to perform equally in terms of magnetoelastic coupling, which is expected due to the polycrystalline growth of the used CoFe thin films. At cryogenic temperatures, the magnetoelastic linewidth  $\Delta H_{me}$  does not exhibit a strong frequency dependence as compared to the room temperature measurements due to the reduced elastic loss rates at cryogenic temperatures. Also the linewidth of the acoustic resonances is significantly smaller at lower temperatures, which reduces the overlapping of the two transverse acoustic phonon modes and thus impacts the visible change in the magnetoelastic linewidth  $\Delta H_{me}$ . Nonetheless, at lower temperatures, it is still possible to discern the different free-spectral-ranges of the acoustic modes and thereby to study magnetoelastic coupling. Here, due to the lower  $\eta_a$  at cryogenic temperatures, the two transverse phononic modes can be tracked up to higher frequencies.

### 5.3 Temperature dependence of the magnetic and acoustic parameters

In this section, we study the temperature dependence of the magnetization dynamics and magnetoelastic coupling parameters of the  $\text{Co}_{25}\text{Fe}_{75}$ /sapphire samples to investigate, whether different substrate orientations have an impact on them. We investigate four different samples, which differ in the crystalline orientation of the used sapphire substrate and deposit  $d = 35$  nm thick  $\text{Co}_{25}\text{Fe}_{75}$  on all these substrates on both-sides polished a-plane, r-plane and c-plane substrates as well as an additional one-side polished c-plane substrate, where the formation of bulk acoustic waves is suppressed. We then characterize these samples using broadband ferromagnetic resonance (bbFMR) experiments up to  $f = 50$  GHz and extract the Gilbert damping parameter  $\alpha$  and the inhomogeneous linewidth  $\mu_0 H_{\text{inh}}$  by fitting the magnetic linewidth  $\mu_0 \Delta H$ , extracted from the Polder susceptibility fits explained in Sec. 3.2, with Eq.(2.18). We perform these experiments for temperatures ranging from cryogenic temperatures  $T = 5$  K up to room temperatures  $T = 300$  K in steps of 10 K.

In Fig. 5.6 a), we plot the Gilbert damping parameter  $\alpha$  as a function of the temperature for each of the four samples. The Gilbert damping parameter  $\alpha$  seems to stay constant up to  $T = 200$  K and then slightly increases towards higher temperatures. We achieve comparable Gilbert damping parameters to literature values in Ref. [77], The Gilbert damping parameters for the a-plane sample (red) are the lowest, next are the data from the r-plane sample (green), the c-plane 1SP sample (blue) and the highest values for the Gilbert damping parameters are measured for the c-plane (black) sample. In Fig. 5.6 b), we plot the inhomogeneous linewidth  $\mu_0 H_{\text{inh}}$  as a function of the temperature for the four different samples. The data of the r-plane (green), a-plane (red) and c-plane 1SP (blue) show the same increase in temperature and all samples exhibit a local maximum around  $T = 25$  K followed by an increase towards higher temperatures. The order for highest to lowest values for the inhomogeneous linewidths  $H_{\text{inh}}$  is opposite as compared to the Gilbert damping parameters  $\alpha$ . The data for the c-plane sample (black) has the lowest inhomogeneous linewidth, then the c-plane 1SP sample (blue), then the r-plane sample (green) and the a-plane sample (red). We attribute this disparity to a simple sample-to-sample variation. It is also possible that, since for the Gilbert damping parameter  $\alpha$  the order of the different samples from highest to lowest values is inverse as compared to the inhomogeneous linewidth  $\mu_0 \Delta H_{\text{inh}}$ , this observation is an artifact from the fit of the bbFMR data with Eq. (2.18) indicating a deviation from a strictly linear in frequency dependence of  $\mu_0 \Delta H$  throughout the investigated temperature range.

We conclude that the choice of the crystalline orientation of the substrate material has a negligible impact on the Gilbert damping parameter  $\alpha$  and the inhomogeneous linewidth  $\mu_0 H_{\text{inh}}$ .

As a next step, we compare the magnetic  $\kappa_s$  and acoustic damping rates  $\eta_{a,i}$  at the microwave frequency  $f_0 = 18$  GHz (taken from Ref. [18]) of the c-plane sample<sup>2)</sup> with the inhomogeneous linewidth  $\mu_0 H_{\text{inh}}$  as a function of the temperature in Fig. 5.7. In panel a) we plot the magnetic damping rate  $\kappa_s$  (black data) as a function of the temperature, which shows the same behavior as the inhomogeneous linewidth  $\mu_0 H_{\text{inh}}$  (red data) with a local maximum at around  $T = 25$  K and an overall increase towards higher temperatures.

<sup>2)</sup>Due to time constraints we refrained from carrying out a full analysis for the a-plane and r-plane samples.

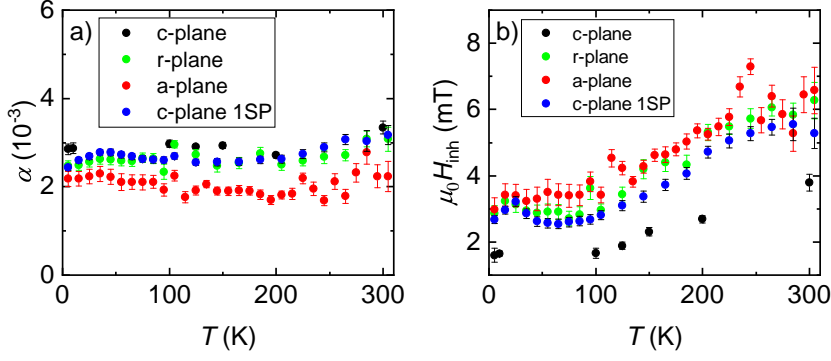


**Figure 5.6:** a) Gilbert damping parameter  $\alpha$  as a function of the temperature for the four different samples. b) The inhomogeneous linewidth  $H_{\text{inh}}$  as a function of temperature for the four different samples.

This is expected due to Eq. (2.18), which relates the magnetic linewidth  $\Delta H$ , which due to the temperature-independent Gilbert damping  $\alpha$  (see Fig. 5.6(a)) is directly related to the magnetic damping via Eq. (2.26), with the inhomogeneous linewidth  $H_{\text{inh}}$ . However, the inhomogeneous linewidth  $H_{\text{inh}}$  at  $f = 18$  GHz still contributes significantly to the magnetic damping  $\kappa_s$ . In panel b), we plot the two acoustic damping rates  $\eta_{a,i}$  (green/blue data) (taken from Ref. [18]) and compare them to the inhomogeneous linewidth  $H_{\text{inh}}$  as a function of the temperature. The acoustic damping rates  $\eta_{a,i}$  saturate towards for both low and elevated temperatures and show a strong increase in the intermediate temperature range. This behavior is expected and up to  $T = 150$  K, we can describe the temperature-dependence according to Ref. [78] using

$$\eta_{a,i} = \eta_{a,i}^0 + \beta_{a,i} T^4, \quad (5.2)$$

where the  $T^4$  term originates from phonon-phonon scattering of the standing waves with thermal phonons [59].

The fit of Eq. (5.2) to the data for the acoustic damping rates  $\eta_{a,i}$  in Fig. 5.7b) yields the values presented in Tab. 5.2.

$\eta_{a,1}/\pi$ [MHz]	$\beta_{a,1}/\pi$ [mHz/K <sup>4</sup> ]	$\eta_{a,2}/\pi$ [MHz]	$\beta_{a,2}/\pi$ [mHz/K <sup>4</sup> ]
$0.32 \pm 0.01$	$4.56 \pm 0.32$	$0.44 \pm 0.04$	$1.94 \pm 0.06$

**Table 5.2:** Fitted values for the acoustic damping rates  $\eta_{a,i}$  in Fig. 5.6b) using Eq. (5.2) (data for the loss rates taken from Ref. [18]).

The fitted values presented in Tab. 5.2 are in reasonably good agreement with the literature values from Ref. [78]. We find a correlation between the acoustic damping rates  $\eta_{a,i}$  and the inhomogeneous linewidth  $H_{\text{inh}}$ , since both increase towards higher temperatures. This can be explained by the fact that with higher acoustic damping rates  $\eta_a$  the magnetization dynamics are also more damped due to the magnetoelastic coupling [20].

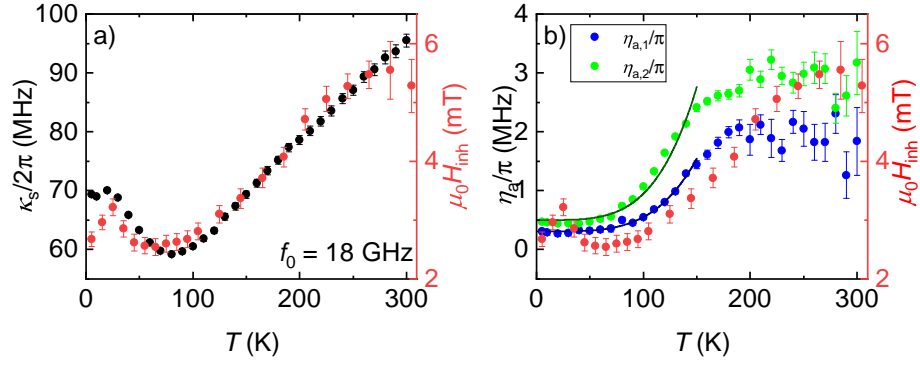


**Figure 5.7:** a) Plot of the magnetic damping rate  $\kappa_s$  (black) at  $f_0 = 18$  GHz (data taken from [18]) and the inhomogeneous linewidth  $\mu_0 H_{\text{inh}}$  (red) as a function of temperature. b) Plot of the acoustic damping rates  $\eta_{a,i}$  (green, blue) at  $f_0 = 18$  GHz (data taken from [18]) and the inhomogeneous linewidth  $\mu_0 H_{\text{inh}}$  (red) as a function of temperature. The continuous lines represent fits to Eq.(5.2).



## 6 Magnetoelastic coupling in CoFe/Si heterostructures

In the previous chapter 5, we studied the magnetoelastic coupling between  $\text{Co}_{25}\text{Fe}_{75}$  thin films deposited on sapphire ( $\text{Al}_2\text{O}_3$ ) substrates with different crystalline orientations and its effects due to the acoustic birefringence. In this chapter, we investigate the magnetoelastic coupling between a ferromagnetic  $\text{Co}_{25}\text{Fe}_{75}$  thin film on a silicon (001) substrate via FMR-experiments at cryogenic temperatures. We chose silicon as a substrate material due to its CMOS (complementary metal-oxide-semi-conductor) compatibility, which could be useful for possible future applications. In Sec. 6.1, we explain our data analysis procedure, which enables us to determine the experimental parameters that are important for calculating the magnetoelastic coupling rate  $g_{\text{eff}}$ , the cooperativity  $C$  and the oop magnetoelastic coupling parameter  $B_{\text{oop}}$ . In Sec. 6.2, we characterize samples with different  $\text{Co}_{25}\text{Fe}_{75}$  layer thicknesses, in order to determine an optimal layer thickness in terms of magnetic damping and magnetoelastic coupling. Furthermore, in Sec. 6.3, we investigated the magnon-phonon coupling for two different silicon substrate thicknesses and compared their performances. Finally, in Sec. 6.4, we study a CoFe/Si/CoFe trilayer structure at cryogenic temperatures and compared the magnetic linewidth of two samples with different substrate thicknesses.

### 6.1 Data analysis for CoFe/Si magnetoelastic coupling

As a first step, we explain the data analysis procedure performed in this chapter to extract the experimental parameters like the magnetoelastic linewidth  $\Delta H_{\text{me}}$ , the acoustic damping rate  $\eta_{\text{a}}$  and the magnetic damping rate  $\kappa_{\text{s}}$ , which characterize the magnon-phonon coupling. With these parameters we are able to calculate the effective coupling rate  $g_{\text{eff}}$  and the cooperativity  $C = g_{\text{eff}}^2 / \eta_{\text{a}} \kappa_{\text{s}}$ . The data analysis procedure is very similar to the one presented in 4.1, but with one crucial difference, that the splitting of the transverse acoustic phonon modes is more dominant in the present case and its implications are discussed in the following.

In Fig. 6.1, we illustrate the data analysis procedure for CoFe grown on a Si(001) BAW resonator sample with a silicon substrate thickness of  $L = 675 \mu\text{m}$  at cryogenic temperatures  $T = 5 \text{ K}$  and around  $f_0 = 24 \text{ GHz}$ . In panel a), we show a colormap of the normalized complex transmission parameter  $(\text{norm.})|S_{21}| = S_{21}/S_{21}^0$  as a function of the frequency  $f - f_0$  with  $f_0 = 24 \text{ GHz}$  within a frequency range of 20 MHz and as a function of the magnetic field around  $\mu_0 H_{\text{ext}} = 3.238 \text{ T}$  within a magnetic field range of 50 mT. We can clearly recognize the periodic avoided crossings of the Kittel mode (dark brown color) with the transverse acoustic phonon modes and their free-spectral-range (black vertical arrow), which is the difference in frequency of two neighboring modes. Here, we find  $f_{\text{FSR}} = 4.32 \text{ MHz}$ . This value corresponds well with the from Eq. (2.21) calculated value for the free-spectral-range using a Silicon substrate thickness  $L = 675 \mu\text{m}$  and  $v_{\text{T}} = 5850 \frac{\text{m}}{\text{s}}$  [79]. The light and dark blue horizontal lines represent on- and off-resonant cuts at constant frequency of the complex transmission parameter  $(\text{norm.})|S_{21}|$ , which are shown as a function of the magnetic field  $\mu_0 H_{\text{ext}}$  in panel b). The on-resonant light blue data points exhibit a larger linewidth than the off-resonant dark blue data points. We define the difference in their linewidths as the magnetoelastic linewidth  $\Delta H_{\text{me}}$ . In panel c), the magnetic linewidth  $\mu_0 \Delta H$ , which

is extracted from fits to the Polder susceptibility (explained in Sec. 3.2), is plotted versus the frequency  $f - f_0$  in a 10 MHz range. We clearly see two distinct periodic peaks at their respective phonon frequencies  $f_{n,i}$  in the data, which can be associated with two different magnetoelastic linewidths  $\Delta H_{me,1/2}$ , where the individual phonon mode crosses the Kittel-mode. The separation of these periodic peaks in the magnetoelastic linewidth  $\mu_0\Delta H$ , in contrast to only one visible peak in the magnetoelastic linewidth  $\mu_0\Delta H$  for the data of the YIG/GGG sample in Sec. 4 This is attributed to the fact, that the acoustic damping rate of each transverse acoustic phonon mode is small enough so that the two modes can be separated from each other. The off-resonant magnetic linewidth is connected to  $\kappa_s$  via Eq. (2.26).

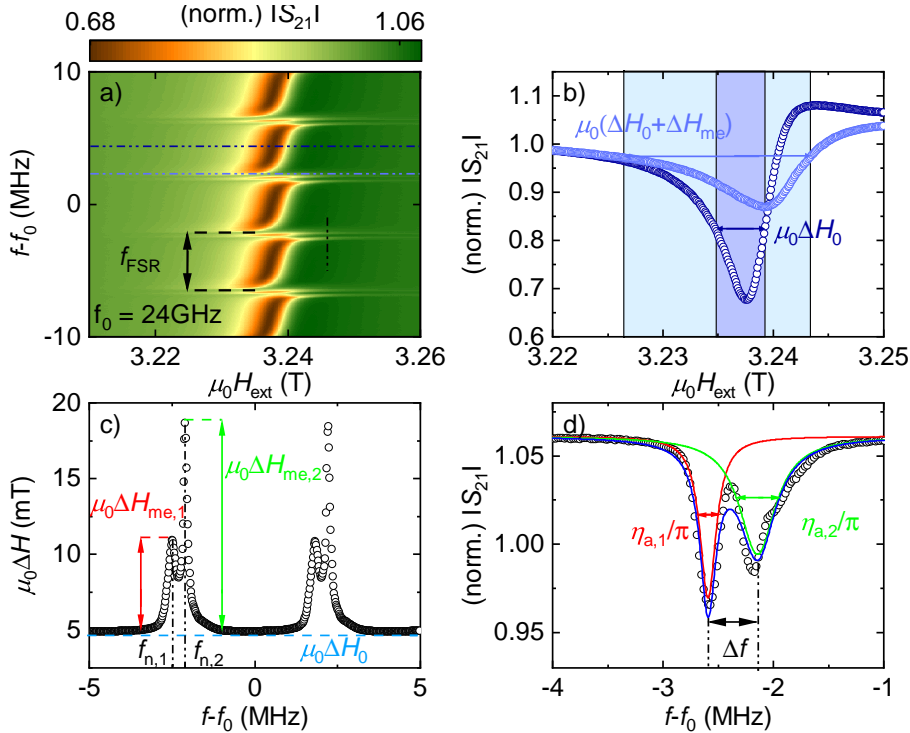


**Figure 6.1:** Illustration of the data analysis procedure with exemplary data for the complex transmission parameter  $S_{21}$  for CoFe/Si-sample in the oop-geometry at  $T = 5$  K. Panel a) shows a normalized microwave transmission amplitude  $(\text{norm.})|S_{21}|$  around  $f_0 = 24$  GHz and  $H_{\text{ext}} = 3.238$  T. Periodic avoided crossings of the Kittel mode and phonon modes are clearly visible and their difference in frequency, the free spectral range  $f_{\text{FSR}}$ , is indicated by a black arrow. The two colored horizontal lines represent cuts through  $(\text{norm.})|S_{21}|$  at constant frequencies, which are plotted in panel b). The dark (light) blue colored line is a cut out-of-resonance (in-resonance) with the  $n^{\text{th}}$  transverse acoustic phonon mode. The difference in their linewidths is the magnetoelastic linewidth  $\Delta H_{me}$ . The black vertical line is a cut through  $(\text{norm.})|S_{21}|$  at constant magnetic field, which is shown in panel d). Panel c) displays the linewidth  $\Delta H$  as a function of frequency, where the magnetoelastic linewidth  $\Delta H_{me}$  is indicated as the peak height. Panel d) is a vertical cut through  $(\text{norm.})|S_{21}|$  at constant  $H_{\text{ext}}$ , which are off-resonant with the Kittel mode. The sum of two Lorentzian functions fitted to the two dips allows to extract the acoustic damping rates  $\eta_{a,i}$  for the two transverse acoustic mode and their difference in center frequencies.

The vertical black line in panel a) represents a cut at constant magnetic field, which is off-resonant of the Kittel mode. The resulting  $(\text{norm.})|S_{21}(f)|$  is shown in panel d). We fit the data to the sum of two Lorentzians, according to (2.25) and extract the acoustic damping

rates for each transverse acoustic phonon mode from the respective linewidths. The difference in their center frequencies  $\Delta f$  is shown as a black arrow. Thereby, we can match the two acoustic damping rates to the magnetoelastic linewidth for both modes by matching their center frequencies.

With the extracted values for the acoustic damping rates  $\eta_{a,i}$ , the magnetic damping  $\kappa_s$  and the magnetoelastic linewidths  $\Delta H_{me}$  we are now able to calculate the effective coupling rates between each transverse acoustic phonon mode via Eq. (2.27) and the Kittel mode and their cooperativities  $C$  in the following sections.

## 6.2 Layer thickness optimization of $\text{Co}_{25}\text{Fe}_{75}$ for Magnon-Phonon coupling

In this section, we discuss the layer thickness optimization of a  $\text{Co}_{25}\text{Fe}_{75}$  layer in a  $\text{Ta}(3\text{ nm})/\text{Cu}(3\text{ nm})/\text{Co}_{25}\text{Fe}_{75}(x\text{ nm})/\text{Cu}(3\text{ nm})/\text{Pt}(3\text{ nm})$  sandwich structure with regards to achieving the maximum magnetoelastic linewidth  $\Delta H_{me}$ . To this end, we fabricate samples with different  $\text{Co}_{25}\text{Fe}_{75}$  layer thicknesses of  $d = 35\text{ nm}, 40\text{ nm}, 50\text{ nm}, 60\text{ nm}$  on silicon substrates with uniform thickness of  $L = 675\ \mu\text{m}$  and perform FMR experiments at cryogenic temperatures  $T = 5\text{ K}$  with frequencies  $f_0$  ranging from 6 GHz up to 45 GHz in steps of 3 GHz and with a range of 40 MHz around  $f_0$  to extract the higher values of  $\Delta H_{me}$  as function of  $f$  for the individual samples. The result is plotted in Fig. 6.2 a), where we find, that the magnetoelastic linewidth  $\Delta H_{me}$  for the data points of the  $d = 40\text{ nm}$   $\text{Co}_{25}\text{Fe}_{75}$  layer exhibits a peak at  $f_0 = 24\text{ GHz}$ , which also constitutes the maximum  $\Delta H_{me}$  of all the characterized samples in this study. However, we did not fabricate a second example with a  $d = 40\text{ nm}$  CoFe thin film layer to proof the reproducibility of these results. Furthermore, panel a) shows that the peak of each set of data in the magnetoelastic linewidth  $\Delta H_{me}$  shifts to higher frequencies with thinner CoFe-layers  $d$ . This is expected, when we look at the expression for the magnetoelastic coupling strength in Eq. (4.2), which has a dependence on the layer thickness  $d$  and since according to Eq. (2.27) the magnetoelastic linewidth  $\Delta H_{me}$  contributes to the magnetoelastic coupling strength, its maximum has also a dependence on the layer thickness  $d$ . We also see in Fig. 6.2 b), that for the thinner CoFe layer thicknesses  $d = 35\text{ nm}, 40\text{ nm}$ , the magnetic linewidth, which is correlated with the magnetic damping rate via Eq. (2.26), is lower than for the thicker layers  $d = 50\text{ nm}, 60\text{ nm}$  due to eddy current damping, which is proportional to the layer thickness squared  $\propto d^2$  [77]. On the other hand, from Eq. (4.2), it is evident, that higher effective coupling rates can be achieved for higher CoFe layer thicknesses. Hence, we have a trade-off between the magnetic damping and magnetoelastic coupling mechanism. For  $d = 40\text{ nm}$  it seems to be near the optimum in terms of the achieved magnetoelastic coupling, i.e. we achieve both low magnetic damping and high magnetoelastic linewidth  $\Delta H_{me}$ , which contributes to the effective magnetoelastic coupling rate  $g_{eff}$  shown in Sec. 6.3.

Up to now we have only studied the maximum  $\Delta H_{me}$  induced by one of the two phonon resonance modes. In Fig. 6.3, the two magnetoelastic linewidths  $\Delta H_{me,1}$  and  $\Delta H_{me,2}$  of both orthogonally polarized transverse phonon modes defined in 6.1 c) are plotted as a function of the microwave frequency for the sample with a 40 nm thin  $\text{Co}_{25}\text{Fe}_{75}$  layer. The shape of both data sets is similar and have a visible maximum in  $\Delta H_{me}$  at around  $f = 24\text{ GHz}$ . We currently do not understand, why one transverse mode exhibits a higher

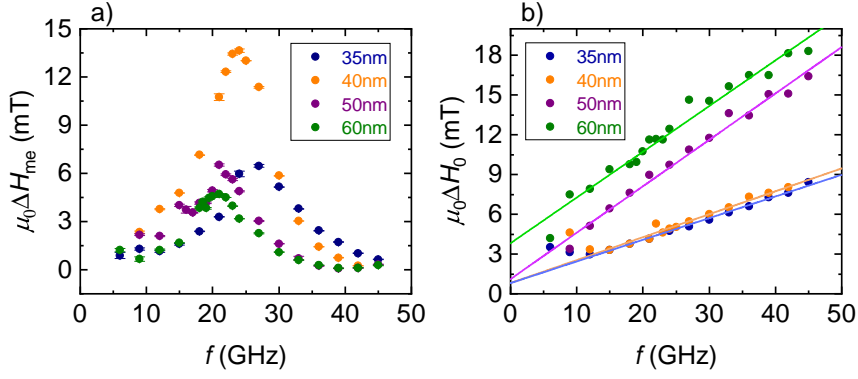


**Figure 6.2:** a) Extracted magnetoelastic linewidth  $\Delta H_{me}$  for different  $\text{Co}_{25}\text{Fe}_{75}$  layer thicknesses as a function of the microwave frequency  $f$ . b) Magnetic linewidth  $\Delta H_0$  for different  $\text{Co}_{25}\text{Fe}_{75}$  layer thicknesses as a function of the microwave frequency. The continuous lines represent fits according to Eq. (2.18).

effective coupling rate than the other as for a polycrystalline thin film of  $\text{Co}_{25}\text{Fe}_{75}$  grown on a crystalline silicon (001) substrate, we would not expect a distinction between the excitation of the two transversal acoustic phonon modes via magnetoelastic coupling. The precise reason for this difference in magnetoelastic coupling will be the subject of future experiments.

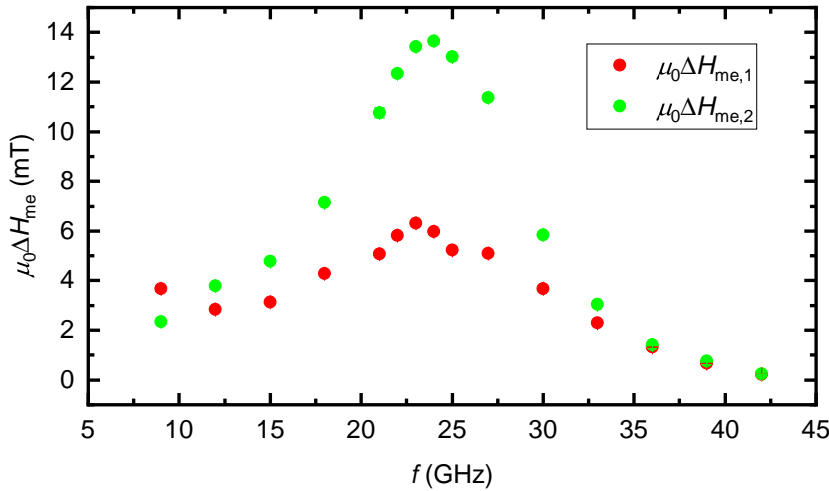


**Figure 6.3:** Comparison of the two magnetoelastic linewidths  $\Delta H_{me,1}$  and  $\Delta H_{me,2}$  of the two orthogonally polarized phonon modes as a function of the microwave frequency for 40 nm  $\text{Co}_{25}\text{Fe}_{75}$  layer thickness.

### 6.3 Dependence of the magnetoelastic coupling on the substrate thickness

Utilizing the established data analysis procedure outlined in Sec. 6.1 and the optimal layer thickness for magnetoelastic coupling of  $\text{Co}_{25}\text{Fe}_{75}$  of  $d = 40$  nm, we now study different silicon bulk acoustic resonator thicknesses. To this end, we deposit the optimized CoFe multilayer stack with the optimized CoFe layer thickness of  $d = 40$  nm on a silicon sub-

strate with a thickness of  $L = 290 \mu\text{m}$  and perform bbFMR experiments at  $T = 5 \text{ K}$  and  $f_0$  ranging from 6 GHz to 45 GHz in a frequency-window of 40 MHz around  $f_0$ , due to the higher free-spectral-range  $f_{\text{FSR}}$  because of the lower substrate thickness, in steps of 3 GHz to characterize the magnetoelastic coupling parameters in this sample. In Fig. 6.4, we plot a comparison for the normalized microwave transmission  $(\text{norm.})|S_{21}|$  as function of  $f$  and  $H_{\text{ext}}$  of the two CoFe/Si BAW resonator samples with different substrate thicknesses of  $L = 290 \mu\text{m}$  (panel a)) and  $L = 675 \mu\text{m}$  (panel b)). In panel a), we find, that the free-spectral-range of the  $L = 290 \mu\text{m}$  substrate is  $f_{\text{FSR}} = 9.96 \text{ MHz}$ , which is in good agreement with the value calculated from Eq. (2.21) for a silicon substrate with  $L = 290 \mu\text{m}$  and  $v_{\text{T}} = 5850 \frac{\text{m}}{\text{s}}$  [79]. Fig. 6.4 also shows, that the avoided crossings for the thinner substrate  $L = 290 \mu\text{m}$  in panel a) are not as strongly pronounced as those for the thicker substrate  $L = 675 \mu\text{m}$  in panel b), which indicates a higher acoustic damping rate for the transverse acoustic phonon modes in the  $L = 290 \mu\text{m}$  CoFe/Si sample compared to the  $L = 675 \mu\text{m}$  CoFe/Si sample. In panel a), we also find, that there are more than two periodic avoided crossings, which indicates the coupling of the magnetization to additional standing transverse acoustic modes, which we attribute to a reverberation effect of multiple reflected phonon modes[80], which play a role due to the reduced silicon substrate thickness.

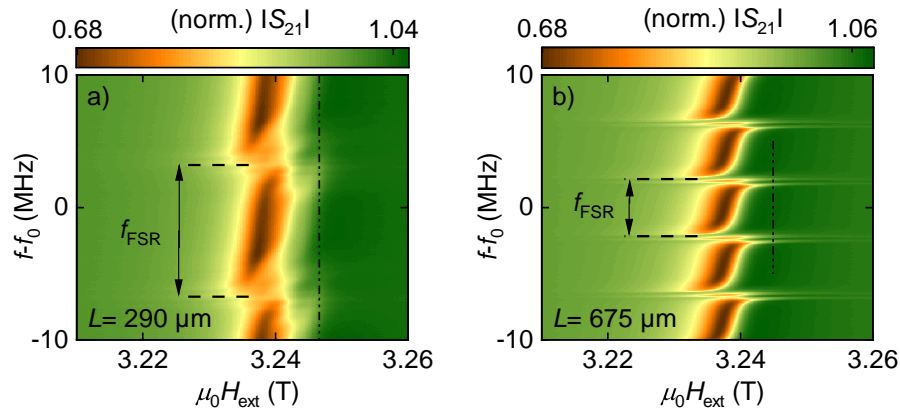


**Figure 6.4:** Comparison of the magnetoelastic coupling at  $f_0 = 24 \text{ GHz}$  and  $T = 5 \text{ K}$  of the two samples with different silicon substrate thicknesses  $L = 290 \mu\text{m}$  (a)) and  $L = 675 \mu\text{m}$  (b)). Both panels show the normalized microwave transmission amplitude  $(\text{norm.})|S_{21}|$  as a function of the microwave frequency  $f - f_0$  for  $f_0 = 24 \text{ GHz}$ . The free-spectral-ranges are indicated with a black arrow and the horizontal black lines represent cuts at constant field which are plotted in Fig. 6.5

In Fig. 6.5, we plot the normalized complex transmission parameter  $(\text{norm.})S_{21}$  at constant magnetic field, off-resonant with the Kittel mode (black data) and in the same frame we plot the magnetic linewidth  $\mu_0 \Delta H$  as a function of frequency (red data). Both data sets are plotted for frequencies around  $f_0 = 24 \text{ GHz}$ . Panel a) shows the data from the  $L = 290 \mu\text{m}$  sample and panel b) shows the data from the  $L = 675 \mu\text{m}$  sample. For the CoFe/Si sample with  $L = 675 \mu\text{m}$  in panel b), we are able to match each magnetoelastic linewidth  $\Delta H_{\text{me},i}$  to a specific transverse acoustic phonon mode, represented by a dip in the normalized complex transmission parameter  $(\text{norm.})S_{21}$ , as the peaks and dips are situated at the same frequency. However, this is not the case in panel a), where we see an overlay of many modes in both  $(\text{norm.})|S_{21}|$  and  $\Delta H$ , which do not manifest at the same

frequencies. As we cannot precisely match the individual features to the specific phonon modes, for our data analysis procedure for the  $L = 290 \mu\text{m}$  sample, we only extract the magnitude of the enveloping magnetoelastic linewidth  $\Delta H_{\text{me}}$  in analogy to our data analysis procedure in chapter 4.

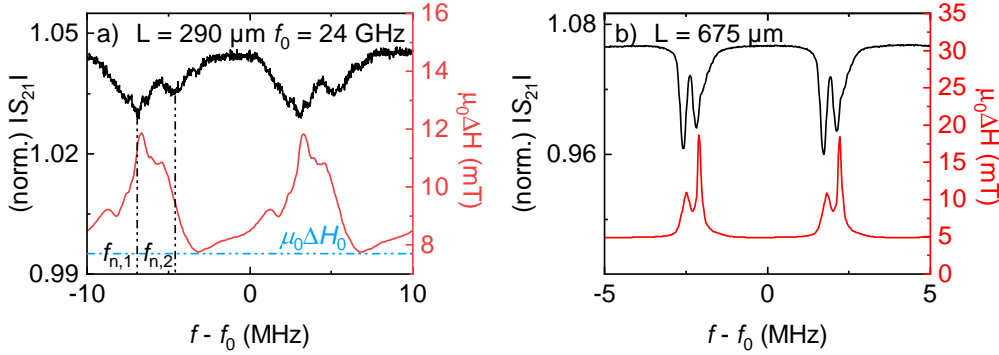


**Figure 6.5:** Comparison of the magnetoelastic coupling at  $f_0 = 24 \text{ GHz}$  and  $T = 5 \text{ K}$  of the two CoFe/Si samples with substrate thicknesses  $L = 290 \mu\text{m}$  (panel a) in a frequency range of 20 MHz and  $L = 675 \mu\text{m}$  (panel b) in a frequency range of 10 MHz. Both panels show a vertical cut of the normalized complex transmission parameter (norm.) $|S_{21}|$  at constant magnetic field (black line) as a function of the microwave frequency (see Fig. 6.1 d)) and the magnetic linewidth  $\mu_0\Delta H$  (red line) as a function of the microwave frequency.

In Fig. 6.6, we plotted the acoustic  $\eta_{a,i}$  and magnetic  $\kappa_s$  damping rates as a function of the microwave frequency, which are extracted from the raw data in (norm.) $|S_{21}|$  using the data analysis procedure described in Sec. 6.1. In panel a), the acoustic damping rates of the two CoFe/Si-samples with different  $L$  are plotted. Here, we show two data sets for each sample, because of the splitting of the two transverse acoustic phonon modes induced by a small miscut of the substrate [19]. They are plotted on a logarithmic scale on the  $\eta_a$ -axis, because the acoustic damping rates for the  $L = 290 \mu\text{m}$ -sample is by an order of magnitude higher than for the  $L = 675 \mu\text{m}$  sample. We attribute this to a broadening of the acoustic modes induced by the imperfect plan-parallelism of the top and bottom BAW resonator interfaces, which comes into play more strongly for the thinner substrate due to its larger aspect ratio. This leads to an imperfect constructive interference of the acoustic waves in the BAW resulting in a more strongly damped standing wave for the thinner CoFe/Si-sample. The frequency-dependence of  $\eta_a$  for Si can be modeled with a linear function following the "Akhiezer theory"[81], where the acoustic damping is induced by the relaxation of thermally excited phonons. The fitted values  $b$  for the slopes are shown in Tab. 6.1.

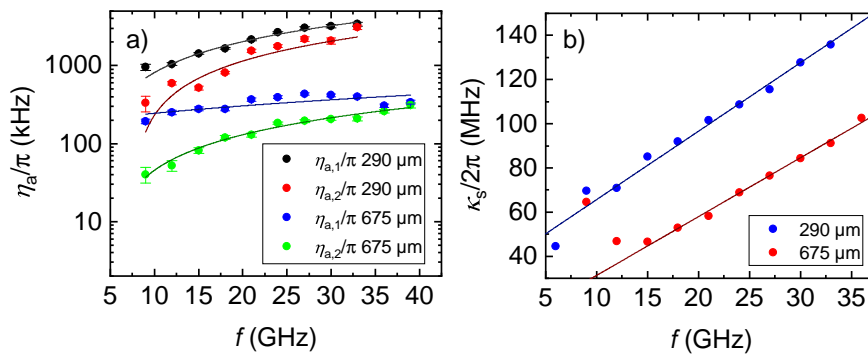
$b$	290 $\mu\text{m}$ mode 1	290 $\mu\text{m}$ mode 2	675 $\mu\text{m}$ mode 1	675 $\mu\text{m}$ mode 2
	$1.21(70) \times 10^{-4}$	$0.91(19) \times 10^{-4}$	$0.06(2) \times 10^{-4}$	$0.08(1) \times 10^{-4}$

**Table 6.1:** Values of the slopes of the linear fits in Fig. 6.6

The values of the slopes in Tab. 6.1 for the two transverse phonon modes for each sample are in good agreement with each other, but differ by more than an order of magnitude for the two different Si substrates. Therefore, the frequency dependence of the acoustic

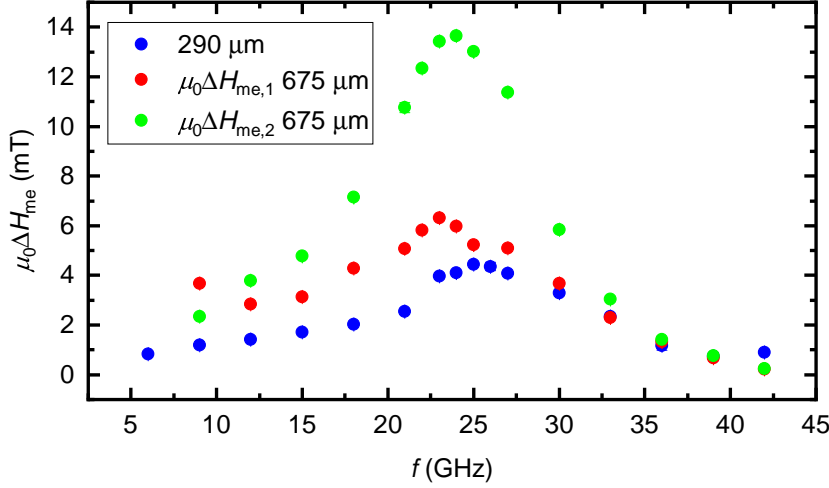
damping rates  $\eta_{a,i}$  seems to vary for different Si substrates.

Fig. 6.6 b) shows the magnetic damping, extracted from the off-resonant linewidth  $\Delta H_0$  via Eq. (2.26). The continuous lines represent a linear fit according to the model established in Sec. 2.2. The extracted parameters for the Gilbert damping parameter  $\alpha$  of CoFe are  $\alpha_{290\mu\text{m}} = 4.9(3) \times 10^{-3}$  and  $\alpha_{675\mu\text{m}} = 4.3(2) \times 10^{-3}$ , which are in good agreement with literature values (see Refs. [77, 82]). From this analysis we find that the slope of  $\kappa_s(f)$  for both samples is very similar, but the y-axis intercept of the linear fit is considerably larger for the  $L = 290\mu\text{m}$  sample ( $\kappa_s(f = 0) = 34.6(35)$  MHz) than for the  $L = 675\mu\text{m}$  sample ( $\kappa_s(f = 0) = 4.7(22)$  MHz), which might be an indication for a larger surface roughness contributing to inhomogeneous broadening. We note that the increase in  $\kappa_s$  for the  $L = 675\mu\text{m}$  sample at low frequencies is attributed to a slight misalignment of the external magnetic field with respect to the surface normal of the sample.



**Figure 6.6:** a) Acoustic damping rates from the  $L = 290\mu\text{m}$  and the  $L = 675\mu\text{m}$  samples as a function of the microwave frequency. The continuous lines represent a linear fit for the acoustic damping rate as a function of frequency according to Ref.[81]. b) Magnetic damping rates of both samples as a function of the microwave frequency. The continuous lines represent a fit model according to Eq. 2.18 in the theory in Sec.2.2.

In Fig. 6.7, we compare the magnetoelastic linewidth  $\Delta H_{\text{me}}$  of the two CoFe/Si-samples as a function of the microwave frequency. For the  $L = 675\mu\text{m}$  sample, we plot both magnetoelastic linewidths  $\Delta H_{\text{me},1}$  and  $\Delta H_{\text{me},2}$  for the two transverse acoustic modes. Here, we find, that both of the two transverse acoustic phonon modes have a higher impact on the magnetic linewidth  $\mu_0\Delta H$  in the  $L = 675\mu\text{m}$  substrate than for the  $L = 275\mu\text{m}$  substrate. This is attributed to the fact that the acoustic damping rate is by an order of magnitude higher in the  $L = 290\mu\text{m}$  sample than in the  $L = 675\mu\text{m}$  sample, which means that the modes are broader and tend to overlap. In addition, the magnetoelastic coupling strength in Eq. (4.2) is proportional to  $\sqrt{\frac{1}{L}}$ . Hence, we expect a higher effective coupling rate for the  $L = 290\mu\text{m}$  sample than for the  $L = 675\mu\text{m}$  sample. For the magnetoelastic linewidth  $\Delta H_{\text{me}}$ , this increase in the effective coupling rate is counterbalanced by the increase of the acoustic damping rate by an order of magnitude for the thinner sample (see Eq. (2.27)). Thus, our observations can be rationalized with the presented magnetoelastic coupling model. However, we see room for further improvement of magnetoelastic coupling effects if we are able to improve for example the acoustic properties of the thinner Si substrates. Having extracted and discussed all the magnetoelastic coupling parameters needed to calculate the effective coupling rate  $g_{\text{eff}}$  and the cooperativity  $C = g_{\text{eff}}/\eta_a\kappa_s$ , we plot in Fig. 6.8



**Figure 6.7:** Comparison of the magnetoelastic linewidth  $\Delta H_{\text{me}}$  of the  $L = 290 \mu\text{m}$  sample with both the magnetoelastic linewidths  $\Delta H_{\text{me},1}$  and  $\Delta H_{\text{me},2}$  of the  $L = 675 \mu\text{m}$  sample as a function of the microwave frequency.

in panel a) the effective coupling strength  $g_{\text{eff}}$  and in panel b) the cooperativity  $C$  as a function of the microwave frequency  $f$ . Note that we are limited in the upper frequency for the  $L = 290 \mu\text{m}$  sample due to the fact that we could only extract values for  $\eta_{a,i}$  up to 33 GHz. In panel a) the value of the data points for the  $L = 290 \mu\text{m}$  sample (red and black) increase with frequency up to around  $f = 27$  GHz, where they exhibit a maximum and decrease for higher frequencies. The values for the  $L = 675 \mu\text{m}$  show the same behavior but with a maximum situated at around  $f = 24$  GHz. The two effective coupling rates  $g_{\text{eff},i}$  for the  $L = 290 \mu\text{m}$  sample are higher than for the  $L = 675 \mu\text{m}$  sample, which is expected as the coupling strength according to Eq. (4.2) is  $\propto \sqrt{\frac{1}{L}}$  and confirms our assumptions above for  $\Delta H_{\text{me}}$ . The effective coupling rates for the  $L = 290 \mu\text{m}$  sample are similar in their values, which is also expected due to the fact, that the two transversely polarized phonon modes are expected to couple equally strong to the circularly precessing magnetization vector. However, the coupling strengths of the  $L = 675 \mu\text{m}$  sample are considerably different in magnitude in particular around the peak frequency  $f = 24$  GHz. As already stated in Sec. 6.2, we do not presently understand, why the two orthogonally polarized transverse phonon modes should couple differently to the magnetization.

The continuous lines represent fits to the effective coupling rates following Eq. (4.2), where we use fixed values for  $M_s = 1.904 \times 10^6 \frac{\text{A}}{\text{m}}$  [83], as well as for the volume densities  $\tilde{\rho}_t = 8110 \frac{\text{kg}}{\text{m}^3}$  and  $\tilde{v}_t = 3170 \frac{\text{m}}{\text{s}}$  [84]. The only free parameter is the magnetoelastic coupling parameter  $B_{\text{oop}}$ . For the low frequency regime the fit agrees well with the experimental data. However for higher frequencies a clear deviation between data and fits is observed. Especially, the frequency values for the maximum values in  $g_{\text{eff}}$  differ between fit and experiment. This indicates that further corrections to the model are necessary to fully account for the magnetoelastic system at hand.

The fitted values for the magnetoelastic coupling parameter  $B_{\text{oop}}$  are listed in Tab. 6.2. The values of the  $L = 290 \mu\text{m}$  sample and the  $L = 675 \mu\text{m}$  sample are in good agreement with each other for both the more and less strongly coupled transverse acoustic modes.

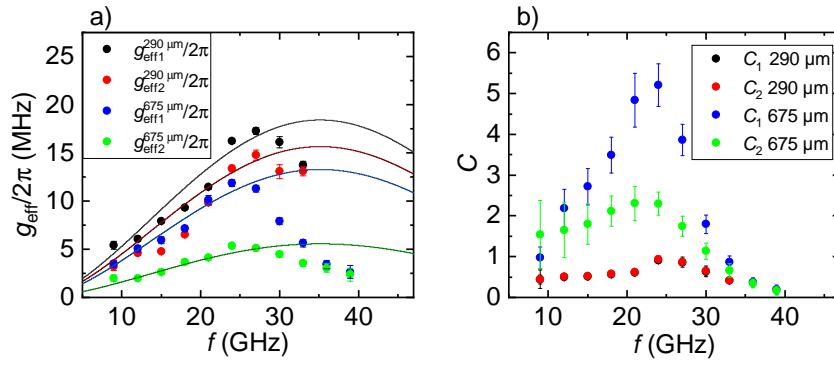


**Figure 6.8:** a) The effective coupling rate  $g_{\text{eff}}$ , calculated according to Eq. (2.27) and (2.29), of the  $L = 675 \mu\text{m}$  substrate and the  $L = 290 \mu\text{m}$  substrate with two separate transverse acoustic phonon modes are shown as a function of the microwave frequency. The continuous lines represent fits for  $g_{\text{eff}}$  using Eq. (4.2). b) The calculated cooperativity  $C$  is plotted as a function of the microwave frequency.

Consequently, it appears, that the difference in the magnetoelastic coupling strength  $g_{\text{eff}}$  arises from a difference in the magnetoelastic coupling parameter  $B_{\text{oop}}$  for the two transverse acoustic phonon modes in these samples. This raises the question, if the  $\text{Co}_{25}\text{Fe}_{75}$  is perfectly polycrystalline or if it exhibits a crystalline texturing, that influences the coupling of the transverse acoustic phonon modes with the Kittel mode [19].

	$g_{\text{eff}1}^{290 \mu\text{m}}/2\pi$	$g_{\text{eff}2}^{290 \mu\text{m}}/2\pi$	$g_{\text{eff}1}^{675 \mu\text{m}}/2\pi$	$g_{\text{eff}2}^{675 \mu\text{m}}/2\pi$
$B_{\text{oop}} [\frac{\text{MJ}}{\text{m}^3}]$	18.6(9)	12.7(11)	21.6(9)	9.3(4)

**Table 6.2:** Fitted values for the oop magnetoelastic coupling parameter  $B_{\text{oop}}$  from the curves displayed in Fig. 6.8.

In Fig. 6.8b), the extracted values for the cooperativity of the  $L = 290 \mu\text{m}$  (black and red) are very similar. Both cooperativities increase with frequency up to  $f = 24 \text{ GHz}$ , which is at their maxima, and then decrease towards higher frequencies. The cooperativities are situated in below 1, which means we do not have a very efficient conversion of magnons into phonons and vice versa, which is mainly due to the high acoustic damping rates  $\eta_{a,i}$  (shown in Fig. 6.6 a)). For the  $L = 675 \mu\text{m}$  sample, we observe a similar trend. The cooperativities increase up to around their maxima at  $f = 24 \text{ GHz}$  and decrease again towards higher microwave frequencies. The cooperativities are situated in the high-cooperativity regime ( $C > 1$ ) for frequencies up to  $f = 30 \text{ GHz}$ , which implies a good conversion between magnons and phonons due to the low acoustic damping rates in this Si-substrate (shown in Fig. 6.6 a)). With both samples, we achieved a coupling in the Purcell regime, as defined in Ref. [72], where  $\kappa_s > g_{\text{eff}} > \eta_a$ .

Having discussed the cooperativity  $C$  and effective coupling rates  $g_{\text{eff}}$  and its dependence on the magnetoelastic linewidth  $\Delta H_{\text{me}}$ , the acoustic damping rate  $\eta_a$ , the magnetic damping rate  $\kappa_s$  and the substrate thickness  $L$ , we want to map the observed discrepancy between experimentally determined  $g_{\text{eff}}$  and the theoretical model from Eq. (4.2) onto a frequency dependent oop magnetoelastic coupling parameter  $B_{\text{oop}}$ . We note that such an approach contradicts our present understanding of the magnetoelastic coupling parameter and should be regarded as a phenomenological approach to expand our model to also rep-

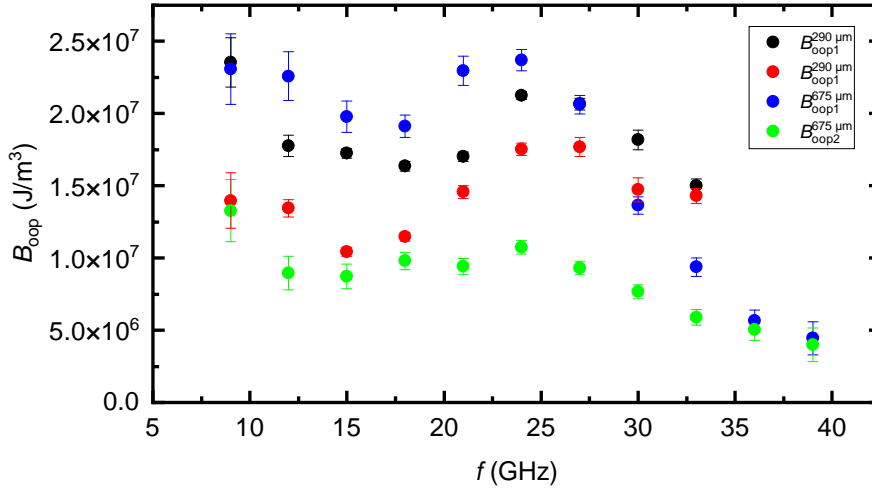


**Figure 6.9:** Magnetoelastic coupling parameter  $B_{\text{oop}}$ , calculated from the two magnetoelastic coupling strengths  $g_{\text{eff},i}$ , as a function of the microwave frequency  $f$ . For each sample two magnetoelastic coupling parameters  $B_{\text{oop},i}$  are shown due to the two transverse acoustic phonon modes.

resent our experimental results. The oop magnetoelastic coupling parameter  $B_{\text{oop}}$  is calculated from the frequency-dependent coupling strength  $g_{\text{eff}}$  and Eq. (4.2) as a function of the microwave frequency. The frequency-dependence of  $B_{\text{oop}}$  is plotted for both samples and both transverse acoustic phonon modes in Fig. 6.9. All four sets of data start at  $f = 9$  GHz and decrease with increasing frequency to  $f = 15$  GHz (red and green data) respectively  $f = 18$  GHz (black and blue data). Then they increase up to around  $f = 24$  GHz, where there is a local maximum and decrease again towards higher microwave frequencies. For  $\text{Co}_{25}\text{Fe}_{75}$   $B_{\text{oop}} = 4.9 \times 10^6 \frac{\text{J}}{\text{m}^3}$  has been reported in Ref. [83]. We here find values for the magnetoelastic coupling parameter  $B_{\text{oop}}$  that are in good agreement with literature values calculated from Refs. [85, 86]. Also the differences in value between the coupling parameters of each sample's transverse acoustic phonon modes and the coupling parameters for the different sample thicknesses are quite prominent. Since the coupling parameter  $B_{\text{oop}}$  is a material property for the  $\text{Co}_{25}\text{Fe}_{75}$  and not the silicon, it is unusual that the substrate thickness has an impact on it. A next step to better understand this observation might be to look into the microstructure of our  $\text{Co}_{25}\text{Fe}_{75}$  thin films deposited on these two Si substrates.

In Fig. 6.10, we plot both effective coupling rates  $g_{\text{eff}}$  at the microwave frequency  $f = 24$  GHz of the  $L = 290 \mu\text{m}$  and the  $L = 675 \mu\text{m}$  sample as a function of the substrate thickness  $L$ . We labeled the higher effective coupling rates (black data) as  $g_{\text{eff},1}$  and the lower one (red data) as  $g_{\text{eff},2}$ . We find, that with increasing substrate thickness  $L$ , the effective coupling rate  $g_{\text{eff}}$  decreases as expected from Eq. (4.2). From this finding, we conclude, that going to thinner substrates may help with achieving the strong coupling limit, defined as  $g_{\text{eff}} > \eta_a, \kappa_s$ , and of course higher cooperativities. At present  $\kappa_s$  is about a factor of 6 larger than  $g_{\text{eff}}$ . Thus we need to reduce the elastic damping rate  $\eta_a$  and the magnetic damping rate  $\kappa_s$  for thin substrates to further increase the magnetoelastic linewidth  $\Delta H_{\text{me}}$  and approach the strong coupling limit.

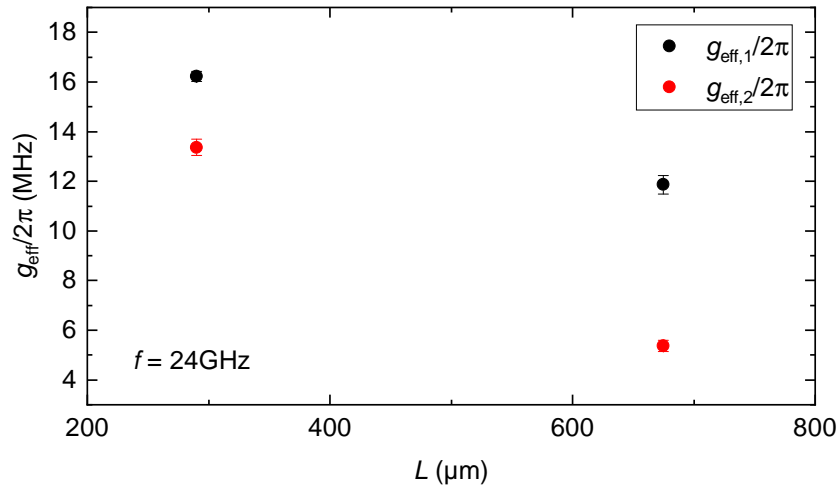


**Figure 6.10:** Effective coupling rate  $g_{\text{eff}}$  at the microwave frequency  $f = 24$  GHz as a function of the substrate thickness  $L$ .

#### 6.4 Tripartite Magnon-phonon coupling in a CoFe/Si/CoFe trilayer sample

In the previous sections of this chapter, we have discussed the magnetoelastic coupling of a CoFe/Si heterostructure at cryogenic temperatures  $T = 5$  K. We addressed the different parameters and their frequency-dependence that describe magnon-phonon coupling.

In this section, we investigate the coupling of the two Kittel modes of magnetic CoFe thin films via phonons in symmetric CoFe/Si/CoFe samples (see Sec. 2.3.3) with  $\text{Co}_{25}\text{Fe}_{75}$  deposited on both sides of polished silicon substrates with  $L = 675 \mu\text{m}$  and  $L = 290 \mu\text{m}$  and perform FMR-experiments at cryogenic temperatures  $T = 5$  K. In order to ensure, that both magnetic layers are driven by the oscillating magnetic field  $h_{\text{rf}}$ , we placed these samples on a broader CPW with a center conductor width of  $w_{\text{cc}} = 1$  mm as compared to the previous FMR-experiments, where we used a CPW with  $w_{\text{cc}} = 100 \mu\text{m}$ .

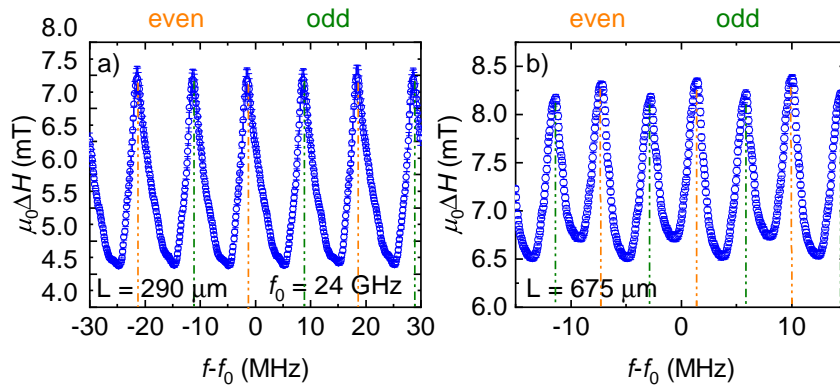


**Figure 6.11:** a) Plot of the magnetic linewidth  $\mu_0\Delta H$  for the  $L = 290 \mu\text{m}$  as a function of the microwave frequency around  $f_0 = 24$  GHz in a range of 60 MHz. The even and odd modes are indicated with orange and green lines, respectively. Panel b) shows  $\mu_0\Delta H$  for the  $L = 675 \mu\text{m}$  sample around  $f_0 = 24$  GHz for a frequency-range of 30 MHz.

In Fig. 6.11 a), the magnetic linewidth  $\mu_0\Delta H$  of the  $L = 290 \mu\text{m}$  sample is shown around  $f_0 = 24 \text{ GHz}$  in a range of 60 MHz. We see six peaks in the magnetic linewidth induced by magnetoelastic coupling. The orange and green lines show the even and odd modes, which can be barely distinguished for this sample. In panel b), the magnetic linewidth  $\mu_0\Delta H$  of the  $L = 675 \mu\text{m}$  sample is shown around  $f_0 = 24 \text{ GHz}$  in a range of 30 MHz. Within this frequency, we can again identify six peaks in  $\Delta H$  induced by magnetoelastic coupling. The difference in the height of the peaks corresponding to even and odd acoustic modes, marked by orange and green lines, respectively, is here much clearer visible for this sample compared to panel a). Not only the magnitude of the peaks in  $\Delta H$  varies periodically for both even and odd acoustic modes, but also the height of the dips. This is expected from the theory in Sec. 2.3.3, where we have different magnetic damping rates  $\tilde{\kappa}_s$  for the even and odd modes, while the even mode has a higher damping rate and because of Eq. (2.26) also a higher magnetic linewidth than the odd mode. The fact that the height of the peaks and dips for the  $L = 675 \mu\text{m}$  sample in panel b) for the even and odd modes are rather different indicates that the coefficient  $x = \frac{\zeta_2}{\zeta_1}$  of the coupling rates  $\zeta_i$  is near 1 and so the two magnetic layers couple almost equally to the oscillating magnetic driving field of the CPW  $\mathbf{h}_{\text{rf}}$ . For the  $L = 290 \mu\text{m}$ , the opposite is true, because of the fact that the heights of the peaks in the magnetic linewidth are similar, which according to Eq. (2.35) and (2.36) means, that  $x = \frac{\zeta_2}{\zeta_1}$  approaches zero meaning the second magnetic layer does almost not couple to the oscillating magnetic field  $\mathbf{h}_{\text{rf}}$ . Naively, this is not expected from the Karlquist equation, which predicts a monotonous decrease in  $\mathbf{h}_{\text{rf}}$  with increasing  $z$ , which would result in a weaker tripartite coupling for the thicker Si/CoFe/Si-sample with  $L = 675 \mu\text{m}$ . However, we also have to take into account, that the acoustic damping in the  $L = 290 \mu\text{m}$  sample is much higher than for the  $L = 675 \mu\text{m}$  as shown in Fig. 6.6 a), which also impacts the efficiency of the magnon-phonon coupling as stated in Sec. 6.3, because a higher acoustic damping rate  $\eta_a$  leads to a lower coupling between the two magnetic layers. Furthermore, as we can see from Fig. 6.11 the magnetoelastic linewidth  $\Delta H_{\text{me}}$ , the height of the peaks, is smaller here compared to the one-side deposited CoFe/Si samples. We attribute this to a higher acoustic damping rate, which originates from an increase in surface roughness due to the both-sided sputter process, which deposits the CoFe. This will be part of future research on this topic.

## 7 Summary

In this thesis, we have studied the magnetoelastic coupling between magnetic thin films and bulk acoustic wave resonators using thin film magnetic materials deposited on different substrate materials by performing ferromagnetic resonance (FMR) experiments at various temperatures ranging from cryogenic temperature  $T = 5$  K up to room temperature  $T = 300$  K in the MORIA cryostat. The impact of magnetoelastic coupling manifests as avoided crossings between the magnetic Kittel mode and the bulk acoustic wave resonances [18, 19]. For the analysis of the effective magnetoelastic coupling rate  $g_{\text{eff}}$ , We have derived a theoretical model, which accounts for both transverse acoustic phonon modes coupling with the Kittel mode as well as the impact of the coupling on the magnetic linewidth and the acoustic damping rates of the two transverse acoustic phonon modes (see Sec. 2.3.2).

In detail, we have studied magnetoelastic coupling in one YIG/GGG sample and  $\text{Co}_{25}\text{Fe}_{75}$  thin films deposited on sapphire, grown in different orientations, and on various silicon substrates. We performed broadband ferromagnetic resonance experiments as well as ferromagnetic resonance around distinct frequencies for both ip- and oop-geometry configurations.

### 7.1 Temperature dependence of magnetoelastic coupling in YIG/GGG heterostructures

To summarize the results presented in chapter 4, we have investigated the magnetoelastic coupling of a  $d = 200$  nm YIG thin film epitaxially grown on a  $L = 500$   $\mu\text{m}$  thick GGG substrate grown in the (111)-direction via FMR experiments. We have established a data-analysis procedure (see Fig. 4.1), which enables us to calculate the effective coupling strengths  $g_{\text{eff}}$ , the cooperativities  $C$  of the coupled magnetic and acoustic modes and the magnetoelastic coupling parameters  $B$ . We have performed FMR experiments, with the sample placed face-down on a coplanar waveguide (CPW) for the ip- and oop-geometry at various temperatures ranging from cryogenic temperatures  $T = 5$  K up to room temperatures  $T = 300$  K. When going to lower temperatures, the effective coupling strength  $g_{\text{eff}}$  and cooperativity for one acoustic phonon mode in the ip-configuration becomes larger than for the oop-configuration at  $T = 150$  K (see Fig. 4.4), which is naively not expected, since the oop-configuration is believed to have a more efficient coupling. Next, we mapped out the magnetoelastic coupling parameters for the ip- and oop-configuration  $B_{\text{oop,ip}}$  as a function of temperature. We have calculated the free magnetoelastic energy density for an external magnetic field applied in each of the three crystalline axes, that are the basis for an orthonormal coordinate system in the crystal. From this calculation, we have determined the magnetoelastic coupling parameters  $B_{\text{oop,ip}}$  as a function of the principal magnetoelastic coupling parameters  $B_{1,2}$  for the cubic (111)-direction. We compare the calculated literature values for  $B_{1,2}$ , with experimentally extracted values. For one transverse acoustic phonon mode measured in the ip-configuration, the data is in good agreement with the literature. However, We find discrepancies in the data for the other transverse acoustic phonon mode measured in the ip-configuration and for the oop-configuration for temperatures below  $T = 150$  K, while for higher temperatures the experimental and literature

data are in good agreement (see Fig. 4.5). In a next step, we have studied the temperature-dependent tuning of the phononic resonances. Here, we have extracted the free-spectral-range  $f_{\text{FSR}}$  as a function of the temperature and compare it to the free-spectral-range obtained by literature values for the temperature-dependent thermal expansion coefficient (see Fig. 4.6). Unfortunately, we had to neglect the temperature dependence of the volume density and the shear modulus, because of a lack of literature values. However, previous works [18, 20] show, that the study of the temperature-dependent tuning of the phononic resonances is a promising method to study the temperature dependence of the thermal expansion coefficient, shear modulus and volume density. Lastly, we have investigated the frequency dependence of the magnetoelastic parameters and compare the oop-geometry at  $T = 300$  K with the ip-geometry at  $T = 5$  K (see Fig. 4.7). In terms of effective coupling strength the ip-geometry at  $T = 5$  K performs slightly better than the oop-geometry at  $T = 300$  K, while the opposite is true for the cooperativity. The data for the effective coupling strength matches the theoretical expected coupling strength only up to around  $f = 9$  GHz. We attribute this discrepancy to a lower film thickness of the YIG layer than the provided nominal value.

## 7.2 Dependence of the magnetoelastic coupling on the orientation of the substrate in CoFe/Sapphire heterostructures

In chapter 5, we have studied the magnetoelastic coupling of a  $d = 35$  nm thin film  $\text{Co}_{25}\text{Fe}_{75}$  deposited on sapphire ( $\text{Al}_2\text{O}_3$ ) substrates with different crystalline orientations with thickness  $L = 500$   $\mu\text{m}$ . First, we discuss the hexagonal crystal system of sapphire and explain the different crystalline orientations with planes located in the unit cell (see Fig. 5.1). Our substrates are polished on both sides and are grown in three different directions: the c-plane, a-plane and r-plane direction. We have solved the famous Christoffel equation for sapphire along the different crystalline directions to extract the magnitudes of the two transverse sound velocities of sapphire as a function of the propagation direction. We have then used these values to calculate their difference along the three different crystalline directions of the substrates (see Fig. 5.2). We have performed FMR experiments with the a-plane and r-plane sample at room temperature with the samples mounted face down onto the CPW in the oop-geometry. Along these two directions, the transverse acoustic sound velocities are non-degenerate and we measured the expected resulting periodical splitting and merging of the phonon resonances as a function of the microwave frequency. Furthermore, we have mapped out the avoided crossings of the phonon and Kittel modes (see Fig. 5.3). For certain microwave frequencies, we can distinguish the two transverse acoustic phonon modes. We have calculated from the measured free-spectral-ranges  $f_{\text{FSR}}$  the difference for the transverse acoustic sound velocities and achieve good agreement with the numerically calculated values from the Christoffel equation. Moreover, we have studied the frequency dependence of the magnetoelastic linewidth for the three different samples at cryogenic temperature  $T = 5$  K and room temperature  $T = 300$  K. We find, that the c-plane sample shows almost no magnetoelastic coupling at room temperature, while the a-plane and r-plane samples show a strong decrease in  $\Delta H_{\text{me}}$  towards higher frequencies. At cryogenic temperatures, all three samples exhibit a comparable  $\Delta H_{\text{me}}$  and the magnetoelastic

coupling is still measurable at higher frequencies (see Fig. 5.5). Lastly, we have studied the temperature dependence of the magnetic and acoustic parameters in the bulk acoustic wave resonator. For this part, we have additionally characterized the magnetization dynamics of  $\text{Co}_{25}\text{Fe}_{75}$  grown on an additional c-plane sample, which is only polished on one side, thus hindering the formation of standing waves in this sample. We have mapped out the Gilbert damping parameter  $\alpha$  and the inhomogeneous linewidth  $H_{\text{inh}}$  as a function of temperature from cryogenic temperature  $T = 5\text{ K}$  up to  $T = 300\text{ K}$  (see Fig. 5.6). We find, that the Gilbert damping parameter has almost no temperature dependence, while the inhomogeneous linewidth increases towards higher temperatures for all four samples. This behavior correlates with the temperature dependence of the magnetic and acoustic damping parameters, which also increase towards higher temperatures (see Fig. 5.7). This correlation can be explained with the higher acoustic damping rates generating more magnetization damping due to the magnetoelastic coupling.

### 7.3 Magnetoelastic coupling in CoFe/Si heterostructures

In chapter 6, we have investigated the magnetoelastic coupling of a  $\text{Co}_{25}\text{Fe}_{75}$  thin film deposited on a  $L = 675\ \mu\text{m}$  (001) silicon substrate via FMR experiments. For this sample, we have found two distinct periodic peaks for the magnetic linewidth as a function of the microwave frequency, while for the YIG/GGG sample in chapter 4, we measured instead of distinct peaks an overlay of many modes. For this reason, we have adjusted the data analysis process from chapter 4 to match the experimental data better (see Fig. 6.1). Using this modified model, we then calculate the effective coupling strength and the cooperativity of our CoFe/Si-BAW resonator samples as a function of the microwave frequency. To achieve maximum effective coupling rates, we optimize the layer thickness of the  $\text{Co}_{25}\text{Fe}_{75}$  thin film and find, that  $d = 40\text{ nm}$  is an optimal layer thickness in terms of low magnetic damping and high magnetoelastic linewidth (see Fig. 6.2). As a next step, we study the magnitudes of the two magnetoelastic linewidths of the Kittel mode coupling to the two transverse phonon modes as a function of the microwave frequency and find, that both magnetoelastic linewidths exhibit difference magnitudes, indicating, that the two transverse acoustic phonon modes couple differently to the Kittel mode (see Fig. 6.3). Next, we have prepared a sample with  $40\text{ nm}$   $\text{Co}_{25}\text{Fe}_{75}$  thin film deposited on a  $290\ \mu\text{m}$  (001) silicon substrate to study the dependence of the magnetoelastic parameters on the substrate thickness. We have found, that the acoustic damping rates for the thinner substrate are an order of magnitude higher than for the thicker substrate and furthermore, the magnetic damping rates are also higher by a factor of up to two. Up to around  $f = 27\text{ GHz}$ , the effective coupling rates are in good agreement with the theoretical prediction, but for higher frequencies the disparity between theory and experimental values become prominent. The two effective coupling strengths of the thicker sample are significantly different, which is not expected (see Fig. 6.8 a)). From the data for the effective coupling strengths, we calculate the oop magnetoelastic parameters for each transverse acoustic phonon mode in each sample and achieve a good agreement. Furthermore, we report a frequency dependence of the oop magnetoelastic coupling parameter, which is not expected (see Fig. 6.9). The effective coupling rates as a function of the microwave frequency are larger for the thinner

sample, which is expected due to a  $\sqrt{\frac{1}{L}}$  dependence of the effective coupling strength (see Fig. 6.10), while the cooperativity of the thicker sample is higher with  $C > 1$  and the thinner sample has cooperativities  $< 1$ , due to the higher acoustic damping of the thinner Si sample (see Fig. 6.8 b)). Lastly, we deposited  $d = 40$  nm  $\text{Co}_{25}\text{Fe}_{75}$  thin films on both sides of a both sides polished Si substrate to study tripartite coupling [41]. We have then performed FMR experiments at  $T = 5$  K and plotted the magnetic linewidth as a function of the microwave frequency (see Fig. 6.11). Here, we have found the expected periodic changes in the peaks for even and odd elastic resonances, which can be explained by the fact that the excited chiral phonons in the substrate interfere constructively or destructively with the precessing magnetization dynamics in the  $\text{Co}_{25}\text{Fe}_{75}$  top layer for even and odd elastic resonance. Evidently, a constructive (destructive) interference of the modes leads to a higher (lower) magnetic linewidth.

## 8 Outlook

Since the dynamically precessing magnetization in ferromagnetic resonance can excite chiral phonons, which transport angular momentum, a bulk acoustic wave resonator is a good platform for investigating phononic angular momentum transport [19]. The results on the magnetoelastic coupling in YIG/GGG in chapter 4 demonstrate, that at cryogenic temperatures, the ip-configuration exhibits a higher magnetoelastic coupling and cooperativity. This finding is of interest for applications in quantum computing, where the systems operate at low temperatures. The temperature dependent tuning of the phononic resonances in Sec. 4.3 could be a viable option to determine the temperature dependence of material parameters like the volume density, shear modulus and the thermal expansion coefficient [20], which also can be of interest for possible sensor applications. But still some aspects need further research such as the temperature dependence of the magnetoelastic coupling rates below  $T = 150$  K, which is in both the ip- and oop-geometry not yet fully understood. In chapter 5, we have shown that it is possible to control the birefringence of the transverse acoustic phonon modes by depositing CoFe on substrates grown along selected crystallographic directions, where the two transverse acoustic modes are strongly non-degenerate. This can be used to realize phononic retarders like phononic half-wave plates or quarter-wave plates, which, analogous to the optical devices, can shift the polarization direction of linearly polarized phonons or convert circularly into linearly polarized phonons and vice versa [87, 88]. Here, it is possible to repeat the experiments with other substrate materials e.g. silicon grown for example along the (110) direction to verify, that the strong birefringence effects detected for sapphire in this thesis are reproducible for other substrate materials.

In chapter 6, we have already achieved good magnetoelastic coupling in CoFe/Si in the Purcell-enhanced regime [72]. We believe, that when going to thinner Si substrates, it might be possible to further enhance the coupling of the magnetic Kittel and the transverse acoustic phonon modes to reach strong and even ultrastrong coupling [72]. This could be achieved, when using a silicon-on-insulator substrate, with a  $L = 220$  nm silicon layer on top, which is, after depositing the  $\text{Co}_{25}\text{Fe}_{75}$  stack on top, removed from the insulator substrate via HF vapor etching leaving us with 40 nm CoFe on top of 220 nm silicon. For these samples, we would expect bulk acoustic wave resonances with free-spectral-ranges of  $f_{\text{FSR}} = 10$  GHz and an increase in coupling strength by a factor of up to  $\approx 1000$ , which is sufficient to get into the strong coupling limit, if the acoustic and magnetic loss rates remain unchanged with regards to the samples investigated in this thesis.

Regarding the silicon samples with  $\text{Co}_{25}\text{Fe}_{75}$  deposited on both sides, it would be interesting, to additionally measure the magnetization dynamics of the top magnetic layer via the spin rectification effect [89, 90], which allows for an electrical detection of the ferromagnetic resonance, which in turn will contribute to a better understanding of the magnetoelastic coupling of the two magnetic layers via the acoustic modes in the crystalline substrate. Also other substrate materials than silicon and other crystalline directions will be interesting to try.

Due to the large magnetoelastic coupling in  $\text{Co}_{25}\text{Fe}_{75}$ /Si heterostructures, this material system is also promising for the realization of surface acoustic wave (SAW) resonators [22, 23].

As a first step in this direction, we have prepared samples incorporating magnetic gratings, whose width  $w$  are equal to the spacing  $s$ , on top of a  $L = 675 \mu\text{m}$  substrate, as shown in Fig. 8.1 a). One sample was structured with  $w = s = 5 \mu\text{m}$  gratings, which corresponds to surface acoustic waves with a frequency of  $f = 1 \text{ GHz}$  and the other sample has got gratings with  $w = s = 2.5 \mu\text{m}$ , which corresponds to surface acoustic waves with a frequency of  $f = 2 \text{ GHz}$ . We have performed broadband ferromagnetic resonance experiments at  $T = 5 \text{ K}$ . In Fig. 8.1, we plot the derivative divide of the real part of the complex transmission parameter as function of the applied field  $\mu_0 H$  and the microwave frequency  $f$  [91]. We find additionally to the Kittel mode magnetic resonance modes at higher frequencies for both gratings. These additional modes cannot be explained as perpendicular standing spin waves (PSSW) due to the fact that the frequency spacing is too small for the used film thickness. They seem to be dependent on the grating since in Panel a) these modes are closer in frequency spacing compared to the features in panel b).

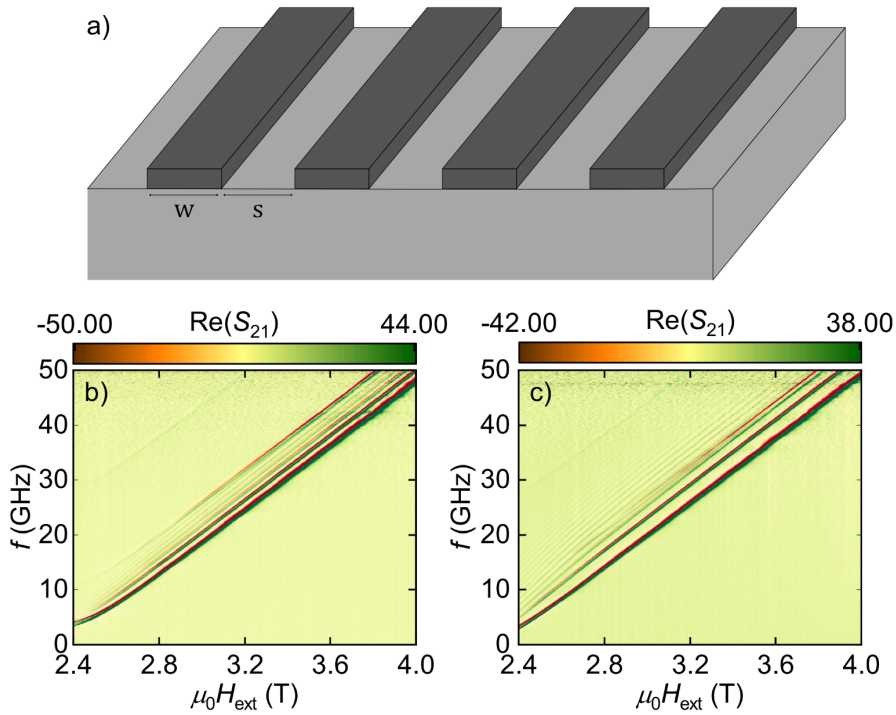


**Figure 8.1:** a) Shows a schematic of the Gratings with width  $w$  and spacing  $s$ . The derivative of the real part of the complex transmission parameter  $S_{21}$  as a function of the microwave frequency  $f$  and applied magnetic field  $\mu_0 H$  for gratings with a spacing of  $s = 5 \mu\text{m}$  and a width of  $w = 5 \mu\text{m}$  (b)) and  $s = 2.5 \mu\text{m}$  and  $w = 2.5 \mu\text{m}$  (c)) at  $T = 5 \text{ K}$ .

The idea for these experiments is to check, if it is possible, to excite surface acoustic waves by driving a ferromagnetic resonance in the magnetic grating. The frequency of the SAW resonance modes is determined by the grating period and hence, we would expect a broadening of the linewidth at the respective frequencies. However, at lower frequencies the Kittel mode deviates from a linear behavior and therefore it is not possible to measure at such low frequencies, because this deviation is caused by the setup, since we are limited by the perpendicular alignment of the surface of the substrate to the applied magnetic field. We additionally perform measurements with higher resolution in frequency to map out

the Kittel mode. We extract the magnetic linewidth  $\mu_0\Delta H$  as a function of the frequency  $f$ , plotted in Fig. 8.2.

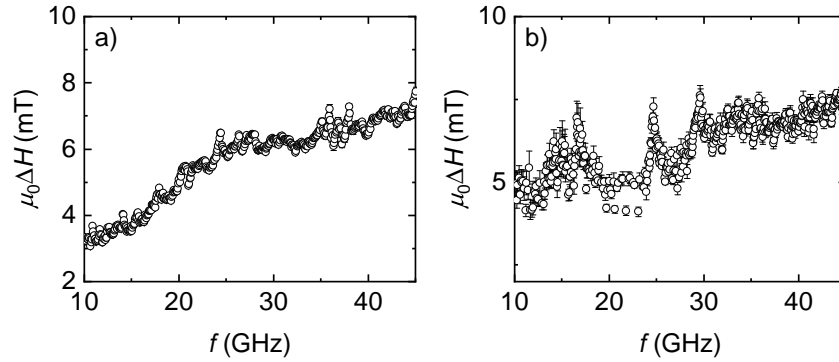


**Figure 8.2:** Magnetic linewidth as a function of the frequency for both grating configurations  $w = s = 5 \mu\text{m}$  (a) and  $w = s = 2.5 \mu\text{m}$  (b).

We see periodic features in  $\Delta H(f)$  in both panels of Fig. 8.2, with a higher frequency periodicity in panel b) compared to panel a). Overall, this aspect also needs further research to unambiguously assign these features to SAW resonance modes and rule out other origins like standing waves in the microwave signal line. As a next step, it would be interesting to fabricate SAW structures with two Bragg-mirrors and a single-electrode transducer in between [22], utilizing the CoFe on silicon material system.

In conclusion, the results presented in this thesis advance the understanding of magnetoelastic coupling in bulk acoustic wave resonator heterostructures, but also raise many new questions for future research projects.



## References

- [1] A. EINSTEIN. *Über einen die Erzeugung und Verwandlung des Lichtes betreffenden heuristischen Gesichtspunkt*. *Annalen der Physik* **322**, 132–148 (1905), [URL](#).
- [2] I. NEWTON. *Philosophiæ naturalis principia mathematica*. Early English books online (Jussu Societas Regiæ ac typis Josephi Streater, prostant venales apud Sam. Smith, 1687), [URL](#).
- [3] A. EINSTEIN. *The Foundation of the General Theory of Relativity* (1916), [URL](#).
- [4] A. EINSTEIN. *Die Plancksche Theorie der Strahlung und die Theorie der spezifischen Wärme [AdP 22, 180 (1907)]*. *Annalen der Physik* **517**, 280–291 (2005), [URL](#).
- [5] R. GROSS AND A. MARX. *Festkörperphysik* (Oldenbourg Wissenschaftsverlag, München, 2012), [URL](#).
- [6] J. BARDEEN AND D. PINES. *Electron-Phonon Interaction in Metals*. *Physical Review* **99**, 1140–1150 (1955), [URL](#).
- [7] J. BARDEEN, L. N. COOPER AND J. R. SCHRIEFFER. *Theory of Superconductivity*. *Physical Review* **108**, 1175–1204 (1957), [URL](#).
- [8] H. FRÖHLICH. *Electrons in lattice fields*. *Advances in Physics* **3**, 325–361 (1954), [URL](#).
- [9] B. N. BROCKHOUSE. *Scattering of Neutrons by Spin Waves in Magnetite*. *Physical Review* **106**, 859–864 (1957), [URL](#).
- [10] Y. LIU, Y. CAI, Y. ZHANG, A. TOVSTOPYAT, S. LIU AND C. SUN. *Materials, Design, and Characteristics of Bulk Acoustic Wave Resonator: A Review*. *Micromachines* **11** (2020), [URL](#).
- [11] S. KRISHNASWAMY, J. ROSENBAUM, S. HORWITZ, C. VALE AND R. MOORE. *Film bulk acoustic wave resonator technology* **1**, 529–536 (1990), [URL](#).
- [12] B. SCHRINSKI, Y. YANG, U. VON LÜPKE, M. BILD, Y. CHU, K. HORNBERGER, S. NIMMRICHTER AND M. FADEL. *Macroscopic Quantum Test with Bulk Acoustic Wave Resonators*. *Physical Review Letters* **130**, 133604 (2023), [URL](#).
- [13] V. J. GOKHALE, B. P. DOWNEY, D. S. KATZER, N. NEPAL, A. C. LANG, R. M. STROUD AND D. J. MEYER. *Epitaxial bulk acoustic wave resonators as highly coherent multi-phonon sources for quantum acoustodynamics*. *Nature Communications* **11**, 2314 (2020), [URL](#).
- [14] W. CRUMP, A. VÄLIMAA AND M. A. SILLANPÄÄ. *Coupling high-overtone bulk acoustic wave resonators via superconducting qubits*. *Applied Physics Letters* **123**, 134004 (2023), [URL](#).
- [15] M. KERVINEN, I. RISSANEN AND M. SILLANPÄÄ. *Interfacing planar superconducting qubits with high overtone bulk acoustic phonons*. *Physical Review B* **97**, 205443 (2018), [URL](#).

- [16] M. KERVINEN, A. VÄLIMAA, J. E. RAMÍREZ-MUÑOZ AND M. A. SILLANPÄÄ. *Sideband Control of a Multimode Quantum Bulk Acoustic System*. *Physical Review Applied* **14**, 054023 (2020), [URL](#).
- [17] E. G. SPENCER, R. C. LECRAW AND A. M. CLOGSTON. *Low-Temperature Line-Width Maximum in Yttrium Iron Garnet*. *Physical Review Letters* **3**, 32–33 (1959), [URL](#).
- [18] M. MÜLLER. *Coupling phenomena in magnonic hybrid heterostructures* (PhD Thesis, Technische Universität München, 2023), [URL](#).
- [19] M. MÜLLER, J. WEBER, F. ENGELHARDT, V. A. S. V. BITTENCOURT, T. LUSCHMANN, M. CHERKASSKII, S. T. B. GOENNENWEIN, S. V. KUSMINSKIY, S. GEPRÄGS, R. GROSS, M. ALTHAMMER AND H. HUEBL. *Chiral phonons and phononic birefringence in ferromagnetic metal - bulk acoustic resonator hybrids*. [arXiv:2303.08429](#) (2023).
- [20] M. MÜLLER, J. WEBER, F. ENGELHARDT, M. CHERKASSKII, S. GOENNENWEIN, S. VIOLA KUSMINSKIY, R. GROSS, M. ALTHAMMER AND H. HUEBL. *Temperature-dependence of magnon-phonon-polarons in a ferromagnetic metal with low Gilbert damping* (2023).
- [21] K. TAKAHASHI. *Magnon-phonon coupling in symmetric magneto-metallic thin film/bulk acoustic wave resonator heterostructures* (Bachelor's Thesis, Technische Universität München, 2023), [URL](#).
- [22] A. JUNG. *Development of Surface Acoustic Wave Resonators Based on Thin-Film Lithium Niobate for Circuit Quantum Acoustics Platforms* (Master's Thesis, Technische Universität München, 2022).
- [23] T. LUSCHMANN, A. JUNG, S. GEPRÄGS, F. X. HASLBECK, A. MARX, S. FILIPP, S. GRÖBLACHER, R. GROSS AND H. HUEBL. *Surface acoustic wave resonators on thin film piezoelectric substrates in the quantum regime*. *Materials for Quantum Technology* **3**, 021001 (2023), [URL](#).
- [24] C. KITTEL. *On the Theory of Ferromagnetic Resonance Absorption*. *Physical Review* **73**, 155–161 (1948), [URL](#).
- [25] N. BOHR. *Studier over metallernes elektrontheori* (Thaning et Appel in Kommission, 1911), [URL](#).
- [26] H. J. V. LEEUWEN. *Problèmes de la théorie électronique du magnétisme*. *Journal De Physique Et Le Radium* **2**, 361–377 (1921), [URL](#).
- [27] W. HEISENBERG. *Mehrkörperproblem und Resonanz in der Quantenmechanik* **38**, 411–426 (1926), [URL](#).
- [28] R. O'HANDLEY. *Modern Magnetic Materials: Principles and Applications* (Wiley, 1999), [URL](#).

- [29] A. LANDÉ. *Über den anomalen Zeemaneffekt* (Springer Netherlands, Dordrecht, 1988), [URL](#).
- [30] R. SHANKAR. *Principles of Quantum Mechanics* (Springer New York, NY, 1994), [URL](#).
- [31] M. PLANCK. *Ueber das Gesetz der Energieverteilung im Normalspectrum* **309**, 553–563 (1901), [URL](#).
- [32] L. LANDAU AND E. LIFSHITZ. *On the theory of the dispersion of magnetic permeability in ferromagnetic bodies* (Pergamon, Amsterdam, 1992), [URL](#).
- [33] T. GILBERT. *A phenomenological theory of damping in ferromagnetic materials*. IEEE Transactions on Magnetics **40**, 3443–3449 (2004), [URL](#).
- [34] L. LIENSBERGER. *Magnon Hybrid Dynamics* (PhD Thesis, Technische Universität München, 2021), [URL](#).
- [35] M. MÜLLER. *Superconductor/Ferromagnet Heterostructures for Superconducting Spintronics* (Master’s Thesis, Technische Universität München, 2019), [URL](#).
- [36] D. POLDER. *On the theory of ferromagnetic resonance*. Physica **15**, 253–255 (1949), [URL](#).
- [37] A. GUREVICH AND G. MELKOV. *Magnetization Oscillations and Waves* (CRC Press, 2020), [URL](#).
- [38] S. CHIKAZUMI. *Physics of Magnetism*. Wiley Series on the Science and Technology of Materials (Wiley, 1964), [URL](#).
- [39] S. STREIB, H. KESHTGAR AND G. E. W. BAUER. *Damping of Magnetization Dynamics by Phonon Pumping*. Physical Review Letters **121**, 027202 (2018), [URL](#).
- [40] T. SATO, W. YU, S. STREIB AND G. E. W. BAUER. *Dynamic magnetoelastic boundary conditions and the pumping of phonons*. Physical Review B **104**, 014403 (2021), [URL](#).
- [41] K. AN, A. N. LITVINENKO, R. KOHNO, A. A. FUAD, V. V. NALETOV, L. VILA, U. EBELS, G. DE LOUBENS, H. HURDEQUINT, N. BEAULIEU, J. BEN YOUSSEF, N. VUKADINOVIC, G. E. W. BAUER, A. N. SLAVIN, V. S. TIBERKEVICH AND O. KLEIN. *Coherent long-range transfer of angular momentum between magnon Kittel modes by phonons*. Physical Review B **101**, 060407 (2020), [URL](#).
- [42] K. AN, R. KOHNO, A. N. LITVINENKO, R. L. SEEGER, V. V. NALETOV, L. VILA, G. DE LOUBENS, J. BEN YOUSSEF, N. VUKADINOVIC, G. E. W. BAUER, A. N. SLAVIN, V. S. TIBERKEVICH AND O. KLEIN. *Bright and Dark States of Two Distant Macrospins Strongly Coupled by Phonons*. Physical Review X **12**, 011060 (2022), [URL](#).
- [43] L. LIENSBERGER. *Spin-Orbit Torques and Magnetization Dynamics in Non-collinear Magnets* (Master’s Thesis, Technische Universität München, 2017), [URL](#).
- [44] V. HAUEISE. *Superconducting spintronics with magnetic insulators* (Bachelor’s Thesis, Technische Universität München, 2021), [URL](#).

- [45] O. KARLQVIST. *Calculation of the Magnetic Field in the Ferromagnetic Layer of a Magnetic Drum*. Acta polytechnica (Elanders boktr.; [H. Lindståhls bokhandel i distribution, 1954), [URL](#).
- [46] A. J. BERGER, E. R. J. EDWARDS, H. T. NEMBACH, A. D. KARENOWSKA, M. WEILER AND T. J. SILVA. *Inductive detection of fieldlike and dampinglike ac inverse spin-orbit torques in ferromagnet/normal-metal bilayers*. Physical Review B **97**, 094407 (2018), [URL](#).
- [47] H. T. NEMBACH, T. J. SILVA, J. M. SHAW, M. L. SCHNEIDER, M. J. CAREY, S. MAAT AND J. R. CHILDRESS. *Perpendicular ferromagnetic resonance measurements of damping and Landé  $g$ -factor in sputtered  $(\text{Co}_2\text{Mn})_{1-x}\text{Ge}_x$  thin films*. Physical Review B **84**, 054424 (2011), [URL](#).
- [48] X. ZHANG, C.-L. ZOU, L. JIANG AND H. X. TANG. *Strongly Coupled Magnons and Cavity Microwave Photons*. Physical Review Letters **113**, 156401 (2014), [URL](#).
- [49] L. BAI, M. HARDER, Y. P. CHEN, X. FAN, J. Q. XIAO AND C.-M. HU. *Spin Pumping in Electrostatically Coupled Magnon-Photon Systems*. Physical Review Letters **114**, 227201 (2015), [URL](#).
- [50] B. A. MOORES, L. R. SLETTEN, J. J. VIENNOT AND K. W. LEHNERT. *Cavity Quantum Acoustic Device in the Multimode Strong Coupling Regime*. Physical Review Letters **120**, 227701 (2018), [URL](#).
- [51] Y. CHU, P. KHAREL, W. H. RENNINGER, L. D. BURKHART, L. FRUNZIO, P. T. RAKICH AND R. J. SCHOELKOPF. *Quantum acoustics with superconducting qubits*. Science **358**, 199–202 (2017), [URL](#).
- [52] C. T. HANN, C.-L. ZOU, Y. ZHANG, Y. CHU, R. J. SCHOELKOPF, S. M. GIRVIN AND L. JIANG. *Hardware-Efficient Quantum Random Access Memory with Hybrid Quantum Acoustic Systems*. Physical Review Letters **123**, 250501 (2019), [URL](#).
- [53] R. SCHLITZ, L. SIEGL, T. SATO, W. YU, G. E. W. BAUER, H. HUEBL AND S. T. B. GOENNENWEIN. *Magnetization dynamics affected by phonon pumping*. Physical Review B **106**, 014407 (2022), [URL](#).
- [54] H. MAIER-FLAIG, S. KLINGLER, C. DUBS, O. SURZHENKO, R. GROSS, M. WEILER, H. HUEBL AND S. T. B. GOENNENWEIN. *Temperature-dependent magnetic damping of yttrium iron garnet spheres*. Physical Review B **95**, 214423 (2017), [URL](#).
- [55] X. ZHANG, C.-L. ZOU, L. JIANG AND H. X. TANG. *Strongly Coupled Magnons and Cavity Microwave Photons*. Physical Review Letters **113**, 156401 (2014), [URL](#).
- [56] M. MARYŠKO. *Influence of GGG substrate on FMR and magnetostatic wave propagation*. Journal of Magnetism and Magnetic Materials **101**, 159–161 (1991), [URL](#).
- [57] J. BARAK, M. X. HUANG AND S. M. BHAGAT. *Electron paramagnetic resonance study of gadolinium–gallium–garnet*. Journal of Applied Physics **71**, 849–853 (1992), [URL](#).

- [58] J. P. WOLFE. *Imaging Phonons: Acoustic Wave Propagation in Solids* (Cambridge University Press, 1998), [URL](#).
- [59] 28 - On the absorption of sound in solids. In *Collected Papers of L.D. Landau* (ed. D. ter Haar) 187–192 (Pergamon, 1965). [URL](#).
- [60] H. MEYER AND A. B. HARRIS. *Specific Heat of Some Rare Earth Iron Garnets and YIG at Low Temperatures*. *Journal of Applied Physics* **31**, S49–S50 (2009), [URL](#).
- [61] A. B. HARRIS AND H. MEYER. *Calorimetric Determination of Energy Levels in Rare-Earth and Yttrium-Iron Garnets*. *Physical Review* **127**, 101–118 (1962), [URL](#).
- [62] Y. LIU, P. ZHOU, R. BIDTHANAPALLY, J. ZHANG, W. ZHANG, M. R. PAGE, T. ZHANG AND G. SRINIVASAN. *Strain Control of Magnetic Anisotropy in Yttrium Iron Garnet Films in a Composite Structure with Yttrium Aluminum Garnet Substrate*. *Journal of Composites Science* **6** (2022), [URL](#).
- [63] R. LECRAW AND R. COMSTOCK. 4 - Magnetoelastic Interactions in Ferromagnetic Insulators. In *Lattice Dynamics Vol. 3 of Physical Acoustics* (ed. W. P. MASON) 127–199 (Academic Press, 1965). [URL](#).
- [64] R. L. COMSTOCK AND W. G. NILSEN. *Parallel Pumping of Magnetoelastic Waves in Lithium Ferrite*. *Physical Review* **136**, A442–A445 (1964), [URL](#).
- [65] D. FRITSCH AND C. EDERER. *First-principles calculation of magnetoelastic coefficients and magnetostriction in the spinel ferrites  $\text{CoFe}_2\text{O}_4$  and  $\text{NiFe}_2\text{O}_4$* . *Physical Review B* **86**, 014406 (2012), [URL](#).
- [66] P. HANSEN, K. ENKE, E. K.-H. WINKLER, G." AND A. M. HELLWEGE. *A Rare-earth garnets of composition  $\text{Y}_{3-x}\text{R}_x\text{Fe}_5\text{O}_{12}$ : Datasheet from Landolt-Börnstein - Group III Condensed Matter · Volume 12A: "Part A: Garnets and Perovskites" in SpringerMaterials* [URL](#). Copyright 1978 Springer-Verlag Berlin Heidelberg.
- [67] T. Y. FAN, D. J. RIPIN, R. L. AGGARWAL, J. R. OCHOA, B. CHANN, M. TILLEMANN AND J. SPITZBERG. *Cryogenic  $\text{Yb}^{3+}$ -Doped Solid-State Lasers*. *IEEE Journal of Selected Topics in Quantum Electronics* **13**, 448–459 (2007), [URL](#).
- [68] Z. KLESZCZEWSKI AND J. BODZENTA. *Phonon–Phonon Interaction in Gadolinium–Gallium Garnet Crystals*. *physica status solidi (b)* **146**, 467–474 (1988), [URL](#).
- [69] S. P. PATI. *Study on the Gilbert damping of polycrystalline YIG films with different capping layers*. *Current Applied Physics* **20**, 167–171 (2020), [URL](#).
- [70] G. SCHMIDT, C. HAUSER, P. TREMPLE, M. PALESCHKE AND E. T. PAPAIOANNOU. *Ultra Thin Films of Yttrium Iron Garnet with Very Low Damping: A Review*. *physica status solidi (b)* **257**, 1900644 (2020), [URL](#).
- [71] S. P. PATI. *Influence on the Gilbert damping of yttrium-iron-garnet films by the spin-pumping effect*. *Materials Science in Semiconductor Processing* **107**, 104821 (2020), [URL](#).

- [72] X. ZHANG, C.-L. ZOU, L. JIANG AND H. X. TANG. *Strongly Coupled Magnons and Cavity Microwave Photons*. *Physical Review Letters* **113**, 156401 (2014), [URL](#).
- [73] R. BARTHOLIN. *Experimenta Crystalli Islandici disdiacastici, quibus mira et insolita refractione detegitur* (1669), [URL](#).
- [74] A.-J. FRESNEL AND G. R. T. PUTLAND. *Extrait of a [second] memoir on double refraction* (2022), [URL](#).
- [75] F. FEDOROV. *Theory of Elastic Waves in Crystal*, 85–117 (1965). [URL](#).
- [76] J. W. JAEKEN AND S. COTTENIER. *Solving the Christoffel equation: Phase and group velocities*. *Computer Physics Communications* **207**, 445–451 (2016), [URL](#).
- [77] L. FLACKE, L. LIENSBERGER, M. ALTHAMMER, H. HUEBL, S. GEPRÄGS, K. SCHULTHEISS, A. BUZDAKOV, T. HULA, H. SCHULTHEISS, E. R. J. EDWARDS, H. T. NEMBACH, J. M. SHAW, R. GROSS AND M. WEILER. *High spin-wave propagation length consistent with low damping in a metallic ferromagnet*. *Applied Physics Letters* **115**, 122402 (2019), [URL](#).
- [78] J. DE KLERK. *Behavior of Coherent Microwave Phonons at Low Temperatures in Al<sub>2</sub>O<sub>3</sub> Using Vapor-Deposited Thin-Film Piezoelectric Transducers*. *Physical Review* **139**, A1635–A1639 (1965), [URL](#).
- [79] Appendix D - Some Useful Physical Constants for Various Crystalline Solids. In *Ultrasonic Methods in Solid State Physics* (eds. R. Truell, C. Elbaum and B. B. Chick) 369–379 (Academic Press, 1969). [URL](#).
- [80] S. ZHARKII, A. KARABUTOV, I. PELIVANOV, N. PODYMOVA AND V. TIMOSHENKO. *Laser ultrasonic study of porous silicon layers*. *Semiconductors* **37**, 468–472 (2003), [URL](#).
- [81] D. LI AND D. G. CAHILL. *Attenuation of 7 GHz surface acoustic waves on silicon*. *Physical Review B* **94**, 104306 (2016), [URL](#).
- [82] R. WEBER, D.-S. HAN, I. BOVENTER, S. JAISWAL, R. LEBRUN, G. JAKOB AND M. KLÄUI. *Gilbert damping of CoFe-alloys*. *Journal of Physics D: Applied Physics* **52**, 325001 (2019), [URL](#).
- [83] D. SCHWIENBACHER, M. PERNPEINTNER, L. LIENSBERGER, E. R. J. EDWARDS, H. T. NEMBACH, J. M. SHAW, M. WEILER, R. GROSS AND H. HUEBL. *Magnetoelasticity of Co<sub>25</sub>Fe<sub>75</sub> thin films*. *Journal of Applied Physics* **126**, 103902 (2019), [URL](#).
- [84] F. CARDARELLI. *Ferrous Metals and Their Alloys*, 59–61 (Springer London, London, 2000). [URL](#).
- [85] M. YAMAMOTO. *Young's Modulus of Elasticity and Its Change with Magnetization in Iron-Cobalt Alloys*. *Physical Review* **59**, 768–768 (1941), [URL](#).
- [86] E. KLOKHOLM AND J. ABOAF. *The saturation magnetostriction of thin polycrystalline films of iron, cobalt, and nickel*. *Journal of Applied Physics* **53**, 2661–2663 (1982), [URL](#).

- 
- [87] J. A. GOLOVCHENKO, B. M. KINCAID, R. A. LEVESQUE, A. E. MEIXNER AND D. R. KAPLAN. *Polarization Pendellösung and the Generation of Circularly Polarized X Rays with a Quarter-Wave Plate*. *Physical Review Letters* **57**, 202–205 (1986), [URL](#).
- [88] C. J. KOESTER. *Achromatic Combinations of Half-Wave Plates*. *Journal of the Optical Society of America* **49**, 405–409 (1959), [URL](#).
- [89] K. HE, J. CHENG, M. YANG, L. SUN, W. SUN, S. BEDANTA, A. AZEVEDO, B. MIAO AND H. DING. *Spin rectification effects in ferromagnetic metal microstrips induced by anisotropic magnetoresistance, planar Hall effect, and anomalous Hall effect*. *Physical Review B* **106**, 104407 (2022), [URL](#).
- [90] Y. GUI, L. BAI AND C. HU. *The physics of spin rectification and its application*. *Science China Physics, Mechanics and Astronomy* **56**, 124–141 (2013), [URL](#).
- [91] H. MAIER-FLAIG, S. T. B. GOENNENWEIN, R. OHSHIMA, M. SHIRAISHI, R. GROSS, H. HUEBL AND M. WEILER. *Note: Derivative divide, a method for the analysis of broadband ferromagnetic resonance in the frequency domain*. *Review of Scientific Instruments* **89**, 076101 (2018), [URL](#).



## 9 Acknowledgements

Während des letzten Jahres, in dem ich am Walther-Meißner-Institut (WMI) in der Magnetiker-Gruppe meine Masterarbeit schreiben durfte, konnte ich auf die Unterstützung vieler Menschen zählen, ohne die das alles nicht möglich gewesen wäre. Insbesondere möchte ich mich bedanken bei:

Prof. Dr. Rudolf Gross für das Vertrauen und die Möglichkeit, meine Masterarbeit hier am WMI schreiben zu dürfen.

Dr. Matthias Althammer für die Themenstellung und die stete Unterstützung und hilfreichen Erklärungen zu sämtlichen Fragen experimenteller und theoretischer Natur. Vielen Dank für deine Hilfe mit dem MORIA Setup, wenn es ums Einkühlen/Aufwärmen ging und dass du auch spät abends für Fragen noch erreichbar warst, wenn ich Probleme mit dem MORIA gehabt habe. Danke auch für das Angebot einer Werkstudentenstelle nach dem ersten Mastersemester, die es mir ermöglicht hat erste Einblicke ins Institut zu erhalten und viele Labore und die Mitarbeitenden kennen zu lernen, was mir den Einstieg in die Forschungsphase im dritten Semester erleichtert hat. Zuletzt möchte ich mich noch für das Korrekturlesen meiner Masterarbeit bedanken.

Dr. Hans Huebl für dein Interesse in meine Forschung, deine hilfreichen Beiträge zur Interpretation der Daten und deine Ideen für Experimente in den Montags-Meetings und nach den Seminarvorträgen. Schließlich noch vielen Dank für dein Vertrauen und dein Angebot mich in Zukunft weiter als Doktorand beschäftigen zu wollen. Ich freue mich auf unsere zukünftige Zusammenarbeit.

Dr. Stephan Geprägs und Dr. Matthias Opel für die wissenschaftlichen Diskussionen der Daten nach den Seminarvorträgen und Danke nochmal an Steve für die Hilfe beim Einkühlen des MORIA Kryostats.

(Dr.) Manuel Müller für deine kontinuierliche Unterstützung Tag und Nacht in sämtlichen Fragen oder Problemen. Du hast mir alle relevanten experimentellen Aufbauten gezeigt und erklärt und du hast mir mit der Fabrikation meiner Proben geholfen. Dein Wissen über die Setups und die Experimente hat mich sehr beeindruckt und ich weiß es sehr zu schätzen, dass du mir in der Schreibphase zeitnah Kommentare geschickt hast. Die Zusammenarbeit mit dir hat mir immer sehr gut gefallen.

Maria Sigl, Simon Gandorfer und Franz Weidenhiller für die zahlreichen Mittagessen und den ein oder anderen Nachmittagsklatsch, die eine willkommene Ablenkung während der Schreibphase waren.

Matthias Grammer für deine Hilfe mit der Nanobeam und für die enge Zusammenarbeit bei der Herstellung der Gratings.

Raphael Höpfl für die vielen Mittagessen während meiner Werkstudentenzeit und am Anfang der Masterarbeit, die eine gute Ablenkung vom Alltag waren. Danke für deine Hilfe mit der Probenherstellung im SUPERBOWL.

Julian Franz für die willkommene Ablenkung während der Schreibphase durch den ein oder anderen etwas längeren Chatverlauf und Danke an Christian Mang für die Zusammenarbeit während meiner Werkstudentenzeit.

Niklas Bruckmoser für deine Hilfe mit dem Wafer dicer oder wenn ich im Reinraum mal aufgeschmissen war und Danke an Monika Scheufele für deine Hilfe während meiner Werkstudentenzeit.

Patricia Oehrl für deine Hilfe mit dem MORIA Kryostat, der ja immer am Wochenende gefüllt werden muss und für deine Hilfe, wenn ich im Reinraum war und gerade nicht weiter wusste.

Meinen Bürokollegen, Valentin Weidemann und Lukas Vogl für die gute Arbeitsatmosphäre.

Astrid Habel für deine Hilfe mit dem Polieren von Substraten und Sebastian Kammerer für seine Sicherheitsunterweisungen.

Die Mitarbeiter in der Helium-Halle, Harald Schwaiger, Peter Binkert und Jan Naundorf für die Bereitstellung von flüssigem Helium und Stickstoff für die Experimente.

Meinen Eltern, Johanna und Peter Weber, die mich während dieses Jahres immer unterstützt haben und Interesse an meiner Forschung gezeigt haben. Vielen Dank, dass ihr immer für mich da seid.